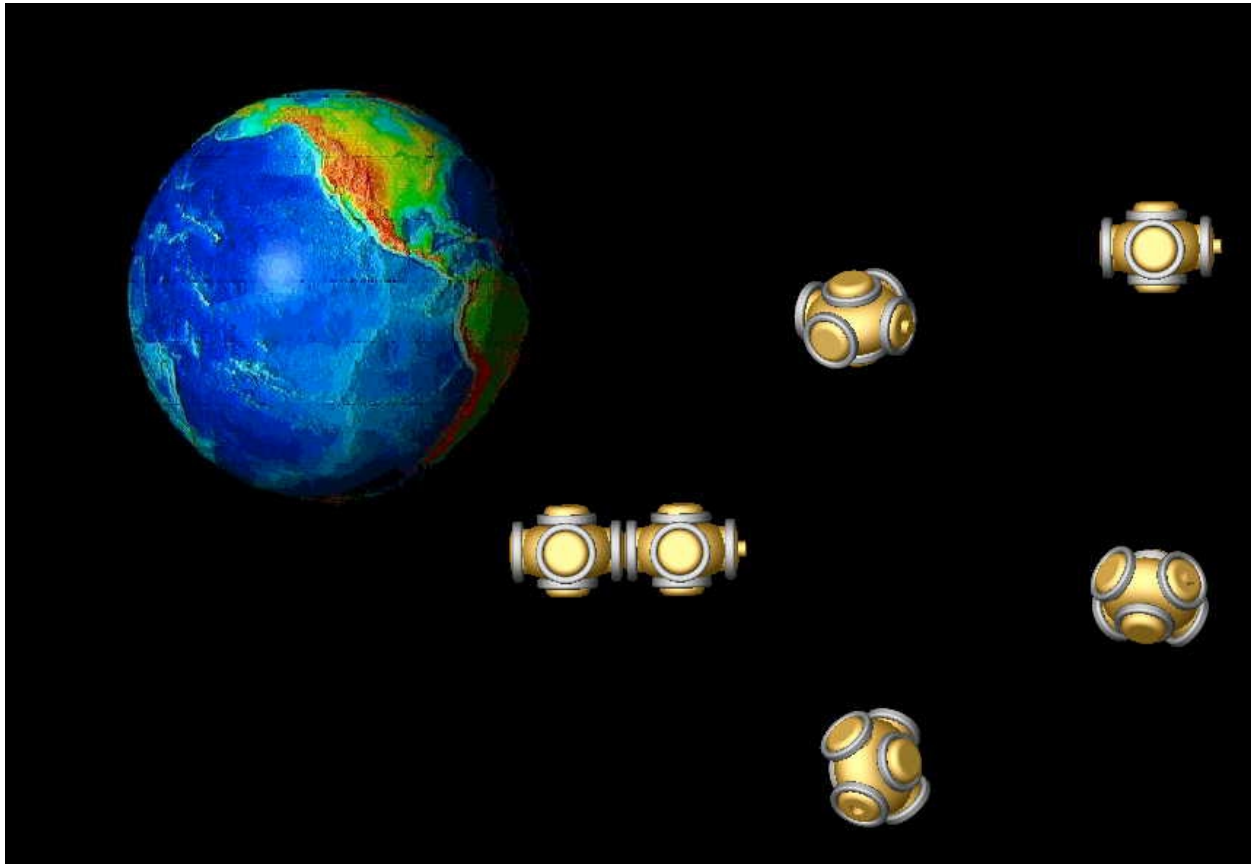


Electromagnetic Formation Flight



Final Report

Principal Investigator: Prof. David W. Miller

Co-Investigator: Dr. Raymond J. Sedwick

Contributors: Laila Elias

Samuel Schweighart

Daniel Kwon

David LoBosco

Massachusetts Institute of Technology
Department of Aeronautics and Astronautics

1. ELECTROMAGNETIC FORMATION FLIGHT OVERVIEW

1.1. Introduction

Satellite formation flight has been identified as the next revolutionary step in remote sensing technology. This allows for the synthesis of large sensor apertures without the need for prohibitively large satellites. These systems also provide mission flexibility by being able to change their geometry to reflect the current mission needs. Furthermore, satellite formations increase reliability, ease deployment, allow staged deployment, improve coverage, and potentially lower cost. By providing these benefits, distributed satellite systems will replace many of today's single, larger satellites.

However, one of the main problems identified with distributed satellite systems is the additional propellant needed to maintain these formations. Distributed satellite systems have a much higher demand on the propulsion system due to the need to keep satellites properly positioned with respect to each other. Even if the geometry of the satellite formation is to remain unchanged throughout the mission, many perturbative effects including differential drag, non-spherical geopotential (J2), and solar pressure all contribute to changes in the formation's geometry and must be counteracted. The amount of propellant that can be carried on the satellite puts an upper limit on the mission lifetime. When the satellites have exhausted the available propellant, there will be a number of perfectly good but generally useless satellites continuing in their orbits.

In response to this limitation, the MIT Space Systems Lab (SSL) has been exploring electro-magnetic formation flight (EMFF). Electromagnets will be used to provide the necessary control authority to maintain satellite formations in the presence of disturbances. Electromagnets offer the added capability to reshape the geometry of the formation while in orbit. By changing the orientation of the electromagnetic field, different forces in any direction can be produced. These forces can be used to re-size or tilt a 'free orbit ellipse' (natural closed orbital paths of satellites in a cluster) or re-shape the satellite formation into almost any geometry. Electromagnets also have the added benefit that they provide a limitless (in time) means of control. Since the power source is electrical, it is a renewable resource and does not limit mission life. Also, unlike conventional thrusters, which may leave a plume of propellant by-products around the formation that can obscure viewing or even deposit on sensitive optics, there are no contamination issues with electromagnets.

1.2. Background and Motivation

While the benefits of separated spacecraft architectures are clear, there are several drawbacks. For example, precision formation flight of the satellites in the array requires that precious propellant be expended to maintain the formation geometry. This has several implications. First, propellant is a consumable that once depleted, renders the satellite useless. Second, the impingement of a thruster plume on a neighboring spacecraft can cause a dynamic disturbance to its stability, deposit particulates on sensitive optics, induce inadvertent charging, and actually ablate material off the spacecraft thereby causing permanent damage. Third, for missions such as NASA's TPF, the propellant plume can put a thermally bright haze across the line-of-sight of the telescope. For example, micron particles at room temperature can blind TPF even if the particles are many kilometers away [Beichman, et. al. 1999].

As one explores the design of these systems in more depth, one recognizes that there is a miss-match between the geometric requirements that the formation must achieve and the way in which that geometry is controlled. Specifically, the relative separations between spacecraft, not the absolute position in space, are important. However, thrusters actuate common mode degrees-of-freedom such as movement of the center of mass. Therefore, it would be desirable if a form of formation control could be developed which does not rely on consumables and reduces the amount of contamination that is introduced by thrusters.

One way to produce this force is through the attraction or repulsion between magnetic dipoles. In a similar manner in which the Coulomb force attracts unlike charges, the opposite poles of a magnet will of course attract. Beyond this simple analogy, however, the difference in the effects quickly becomes apparent, since the variation of the attraction is different in both spatial uniformity as well as the rate at which the force weakens with distance. Whereas the attractive force between two electric charges, or monopoles, drops off as the square of the separation distance, the force between a set of dipoles (electric or magnetic) drops off as separation distance to the fourth power. Unfortunately, since there is no equivalent magnetic monopole, the dipole is the lowest order effect upon

which we may capitalize. An additional shortcoming is that electrostatic coupling is naturally a greater effect than magnetic coupling. Why then should one consider such an approach? There are in fact several advantages:

- 1) The magnetic fields may be generated by current loops rather than charge accumulation. Although it may be argued that in the case of electrostatic charging, since the overall potential of the spacecraft is being raised (or lowered) this effect will not harm the satellite, the natural irregularities of satellites will cause charge concentrations and potential differences across the satellite. At even modest potential differences, arcing across spacecraft components will most likely occur (especially in low Earth orbit operations), potentially causing damage.
- 2) The dipole interactions, in conjunction with reaction wheels can be used to produce ‘torque at a distance’, allowing not only attitude degrees of freedom to be controlled, but also providing the ability to accelerate a configuration into a spinning state without the use of propellant.
- 3) In Earth orbiting operations, the electromagnetic fields produced may be used in conjunction with the Earth’s own field to provide control of angular momentum in the reaction wheels. This is already a common practice, but with the larger field strengths considered, a great deal more authority is available.
- 4) Using current and anticipated superconducting wire technology, very large fields can be produced, with power levels set only by the internal losses in the power system itself. Proper design of the power system can render the additional power requirements negligible in comparison to power available to operate other subsystems.

1.3. Magnetic Dipole Interaction

The interaction of two magnetic dipoles is most easily discussed in the far-field approximation, where the physical size of the dipole is small compared to the separation distance. In terms of loops of wire, the magnetic dipole strength can be written as $\mu = NiA$, the product of the number of loops, the loop current and the area enclosed by the loops. If immersed in an external magnetic field (B), both a torque and a potential are generated on the dipole, and given by

$$\begin{aligned}\vec{T} &= \bar{\mu} \times \vec{B} \\ U &= -\bar{\mu} \cdot \vec{B}\end{aligned}\tag{1.3.1}$$

In addition, the magnetic induction of a dipole scales as

$$B \sim \frac{\mu_0}{2\pi} \frac{\mu}{r^3}\tag{1.3.2}$$

where μ_0 is the permeability of free space, and r is the distance from the dipole. We immediately see that the torque generated by a dipole on a second dipole scales as the reciprocal of distance cubed. Taking the gradient of the potential equation for a point along the dipole axis, and retaining only the axial part, a very specific but telling solution of the force between two opposing dipoles can be found. This is given as

$$F = -\frac{3\mu_0}{2\pi} \frac{\mu_1 \mu_2}{r^4} \cos \theta\tag{1.3.3}$$

where it is seen that the force scales as the product of the dipole moments, and inversely with the separation distance to the fourth power as stated earlier. The cosine comes from the dot product and refers to the orientation of the second dipole to the first. As expected, they attract when oriented the same way, and repel when one is inverted. The other component of force (off axis) has a sine dependence, so for angles other than 0 and 180°, there is a force (and torque from above) that pushes the dipoles off axis from one another. This has some interesting effects.

1.4. Providing Torque-at-a-Distance

Although the near field structure of magnetic and electric dipole interactions are different, in the far field (where the ‘dipole’ approximation is valid) their forms are the same. Because of this, we can use electric dipoles to provide better intuition into this effect, as shown in Figure 1.1.

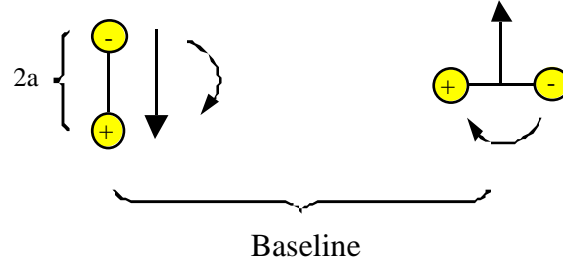


Figure 1.1: Dipole Configuration for Spin-Up

Here we see that the dipoles are placed orthogonally, corresponding to $\theta = 90^\circ$ from above. Both charges on the left dipole push ‘upward’ on the positive charge on the right dipole, and ‘downward’ on the negative charge. This provides a torque in the clockwise direction. The upward force on the positive charge is stronger, since it is closer, so that there is also a net force ‘up’. By similar arguments of the action of the dipole on the right with each charge of the dipole on the left, we see that it is pushed ‘downward’ and torqued in a clockwise manner, consistent with Newton’s third law. If in addition to the electric dipoles, each of the spacecraft is equipped with a reaction wheel, a counteracting torque can be generated to maintain (or appropriately bias) the relative orientation of the two spacecraft. The result is that the spacecraft will begin to translate (the left one down and the right one up), in a manner that will conserve the total angular momentum (spacecraft plus reaction wheels) around the center of the configuration. If an attractive radial force exists to provide centripetal acceleration, they will begin to spin around a common center.

From the previous analysis, we know that a radial force can be provided by aligning the dipoles, so allowing some amount of rotation between the spacecraft will provide the proper balance of forces to spin/de-spin the array without using any propellant at all. In fact, when the dipoles are aligned, there is only a radial force, and when they are orthogonal, there is only a tangential force, so that any ratio of the two may be achieved with the proper relative orientation. Although this demonstrates complete controllability only in 2-D (4 degrees of freedom), the same argument can be posed in 3-D (9 degrees of freedom). The reduced degrees of freedom come from a lack of controllability of the absolute position of the center of mass, which for interferometric missions is not an issue.

1.5. Mission Applicability

Electromagnetic formation flight has wide mission applicability and in the future can revolutionize three pathways.

1) Science

EMFF applied to large scale optical systems will allow man to achieve extremely high resolution telescopes and interferometers.

2) Scientific Environments

Man’s ability to conduct science will be opened to new frontiers such as artificial gravity space environments enabled by EMFF.

3) Mission Design

EMFF will change the way we think about future mission design.

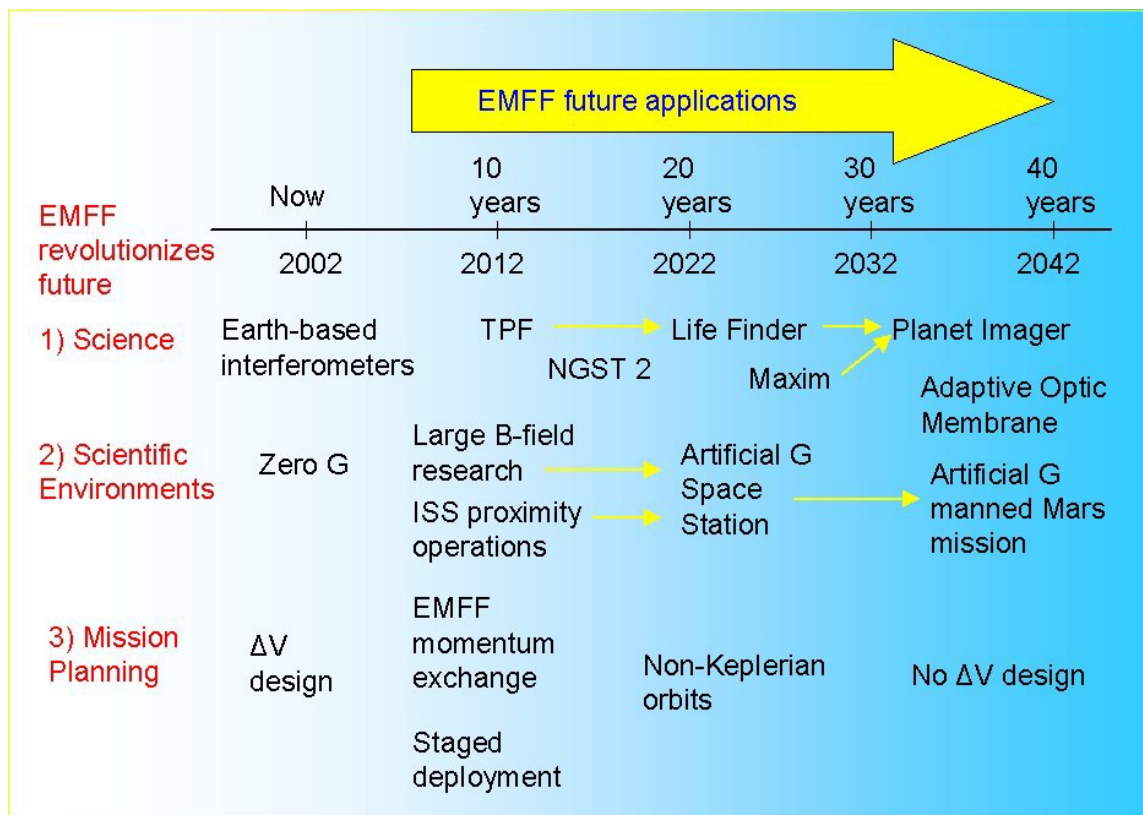


Figure 1.2: The roadmap to future EMFF applications

Science

Electromagnetic formation flight has the ability to enable large scale interferometers and create new unique optical systems that can revolutionize today's science. The first pathway in Figure 1.2 illustrates this roadmap of EMFF applications. Imaging an earth sized planet is the goal of NASA's ORIGINS program and TPF is the first of three missions that will demonstrate the necessary technology. Research at MIT has shown that TPF with an EMFF design is feasible and has the ability to outperform the current cold gas thruster TPF design. A successful demonstration of an EMFF TPF can then lead to EMFF designs for Life Finder, MAXIM, and Planet Imager. Although all the technology necessary for Planet Imager is not fully developed, EMFF allows for large systems such as this, to be built incrementally using staged deployment. The benefits of EMFF, such as lack of propellant deposition and reconfigurable arrays, will be clear on these large scale missions.

Interferometer systems are not the only scientific tools that can be transformed by EMFF. An optical system with resolving power beyond NASA's Next Generation Space Telescope (NGST) is achievable using EMFF to control the deployable secondary mirror. Figure 1.3 illustrates the transformation of NGST using EMFF. The EMFF design of the secondary mirror can eliminate the truss structure leading to a longer focal length for a flat mirror. This follow-on mission to NGST has increased versatility since the secondary can be easily upgraded by another EMFF secondary. When the time comes to upgrade, the new secondary can be flown in without the need for human interaction saving costs. Additional costs are also saved since the current truss can be eliminated leading to a significant mass savings.

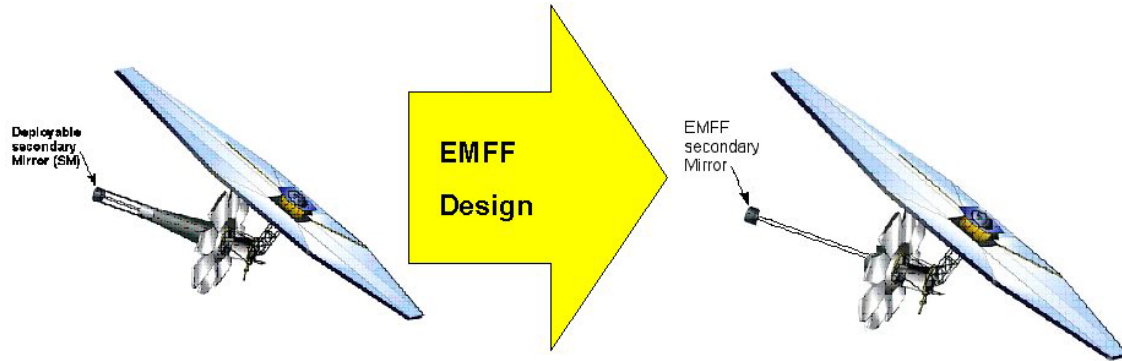


Figure 1.3. Next Generation NGST (NGST 2) using EMFF

EMFF is a key technology in the creation of an Adaptive Membrane for imaging, a system which can change the design of future telescope systems. Figure 1.4 shows a conceptual drawing of what this system may look like. A ring of EMFF spacecraft can create tension in the membrane surface and actively change the curvature for a wide range of optical resolutions. An EMFF secondary mirror or membrane can also be flown as part of the system. EMFF is a critical technology because it has the ability to uniquely change the shape, size, and tension of the membrane surface and possibly surface components using electric dipole interaction. The EMFF enabled Adaptive Membrane surface is highly conceptual, however new horizons in science can be opened if it is achieved.

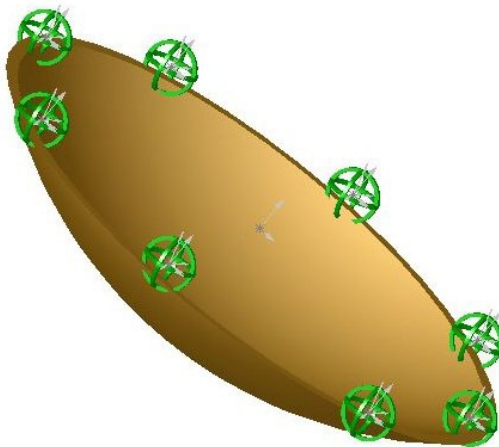


Figure 1.4. Adaptive Membrane for imaging

Scientific Environments

EMFF can transform the future space environment by the second pathway illustrated in Figure 1.2 ultimately leading to an EMFF artificial gravity space station and a possible EMFF artificial gravity Mars array. Before this can be realized there are three distinct steps for EMFF application in scientific environments.

1) Applications of large magnetic fields in zero gravity.

EMFF can create a unique scientific environment in zero gravity for determining the effects and uses of a large magnetic field. For example, EMFF can be used as a long range grappeler for sample acquisition.

2) ISS proximity operations

The International Space Station can increase its versatility using EMFF modules. Such operations include a reconfigurable station using these EMFF modules and controlled maneuvers of instruments or astronauts outside of the station.

3) Protective magnetospheres

An EMFF spacecraft can use its magnetic field to create a protective magnetosphere from cosmic radiation and solar flares as shown in Figure 1.5. Research on the effects of this protective magnetosphere must be conducted before a long term manned spacecraft mission can be designed.

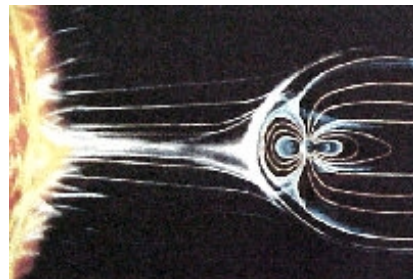


Figure 1.5: Protective magnetosphere created by an EMFF spacecraft

(Picture courtesy of schooltv.com)

Artificial gravity in space has been proposed before by either spinning a large wheel-shaped spacecraft or spinning two spacecraft attached by a tether. The idea behind each method is to produce a centripetal acceleration equal to that of the gravity field one is trying to reproduce. In these conventional systems, some sort of large structure is needed to connect the two spacecraft (or hold the wheel together), and a propulsion system is needed to start the spinning and perform corrections. Tethered systems have highly non-linear dynamics that are difficult to control. A significant amount of structural and propulsive components could be eliminated with the use of an electromagnet system. Figure 1.6 shows an artificial gravity space station design, with two spacecraft demonstrating EMFF docking and an additional spacecraft demonstrating staged deployment by entering the reconfigurable array. EMFF is used to spin the array to achieve a gravity environment within the spacecraft. Applications of artificial gravity include a manned mission to Mars, Earth orbiting space laboratories, and space tourism. A possible Mars mission could consist of a habitation spacecraft and a return vehicle spacecraft rotating around each other to simulate a Mars gravity environment.

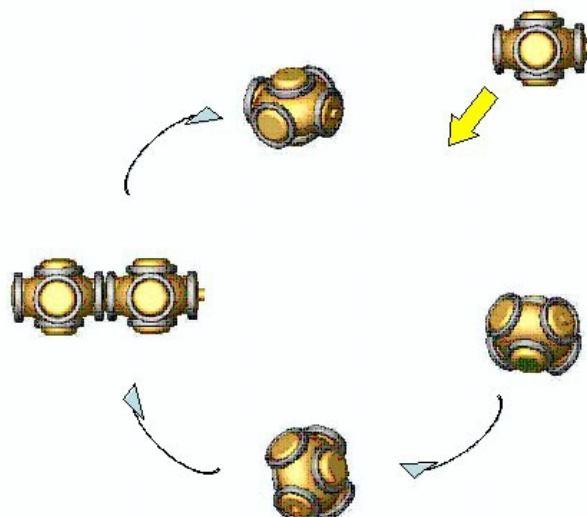


Figure 1.6: Artificial gravity space station

Mission Planning

All applications of EMFF change future mission planning paradigms since EMFF does not require a consumable for control of relative separation, relative attitude, and inertial rotation of an array. Therefore, formation flight missions are no longer based on ΔV requirements, but on their relative orientations. Without the limiting restrictions of ΔV , long term and large scale missions are enabled at a lower cost and lower launch mass. Future space missions can now plan on permanent spacecraft arrays for scientific environments and even habitation. Additionally EMFF can be applied to space maneuvers such as docking and rendezvous since they require relative control of two spacecrafts. Docking and rendezvous can benefit from EMFF since it can offer an unlimited amount of maneuvers. Mars sample acquisition is a possible application of an EMFF docking maneuver using a small EMFF sample container and larger EMFF spacecraft.

EMFF can also be used to sustain long-term non-Keplarian orbits. Since EMFF can apply continuous forces between spacecraft, orbits that cannot be obtained without sustained propellant use are now feasible. Two examples are increased formation spin rates for satellite formations and ‘stationary’ formations. In LEO, satellite formations will rotate at a rate of one revolution per orbit (~90 minutes). For satellite interferometry missions, this rotation rate may be too slow for mission applications. To have the formation spin faster than this, propellant must be continuously employed to hold the formation together. With EMFF, these orbits are within the standard uses of EMFF and require no usage of expendables.

Rotation of the formation may not be desired for some mission applications. For example a distributed telescope where the large primary lens or mirror is separated from the rest of the optics. These missions need to be held stationary in orbit. Holding one satellite fixed with respect to another satellite can be achieved with the continuous use of propellant or by the use of EMFF.

Finally, the geostationary belt is rapidly filling. Currently only satellites on the equatorial plane and at the correct altitude remain geostationary. However, if pairs of EMFF satellites were placed into a geostationary orbit, they could push against each other, placing one satellite above the equatorial plane and one satellite below. These satellites would remain geostationary, but not lie on the equatorial plane, thus increasing the capabilities of the geostationary belt. Overall, EMFF allows for a large set of orbit possibilities that are not achievable using current traditional propulsion methods.

Future system architectures

EMFF has enabled new scenarios in scientific research, scientific environments, and mission planning. However, there are some other unique applications of an EMFF system. Figure 1.7 illustrates an EMFF garbage collector system. This system consists of a ring of EMFF spacecraft that would attract any space debris, such as dead satellites, into center of the array. Once a critical amount of debris has accumulated in the center, the array can spin up the debris and perform a momentum exchange maneuver dumping the debris into the Earth’s atmosphere and changing the orbit of the garbage collector system. Such a system could sweep for garbage indefinitely since does not need to worry about running out of propellant and also become space debris.

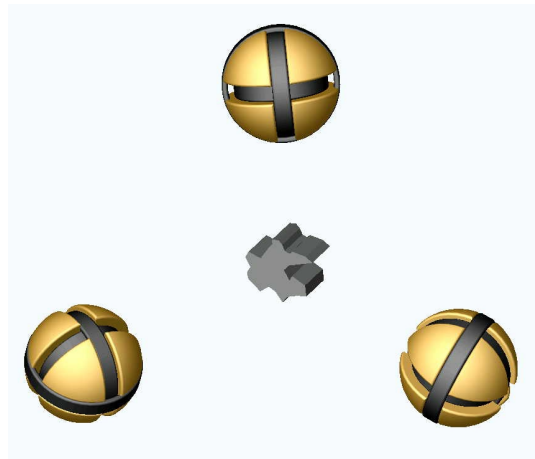


Figure 1.7: EMFF garbage collector concept

Spinning satellites and exchanging momentum using an EMFF array also has a military application. Satellites placed in the center of an EMFF system can be disabled either by de-orbiting, rapid spinning to saturate the reaction wheel, or locking its position. The final designs of these applications are still in the future, however the critical maneuvers can be enabled by EMFF.

2. ENABLING TECHNOLOGIES

The technologies that comprise EMFF are listed in Table 2.1. The first five are physical technologies where a concept has been reduced to hardware, such as high temperature superconducting wire, whereas the last three are conceptual, or mathematics based, such as the modeling of electromagnetic interactions, or non-linear dynamics. Listed alongside each technology are two NASA TRL numbers. The first represents the state of the art in its own right, whereas the second is the state of the art in the context of EMFF. For example, cryo-coolers are a commercially available product that can be purchased off the shelf, and have even been flight proven. By all rights, the technology is at TRL 9. However, the heat flow rate that is supported by these devices is much lower than is needed for EMFF, since a much larger surface is available to absorb heat. Conceptually, cryo-cooler technology can be adapted to such a need, but there has been no specific development for this purpose. Therefore the technology in relation to EMFF is only at TRL 2. This section discusses some of these critical technologies in more detail.

Table 2.1. Critical Technologies that Comprise EMFF

Critical Technology	TRL (G)	TRL (EMFF)
High temperature superconducting (HTS) wire	6	4
Cryogenic cooling and thermal control	9	2
High current, low voltage power systems	6	4
High angular momentum storage reaction wheels	6	3
Active and passive magnetic shielding	6	2
Efficient near field electromagnetic dipole interaction algorithms	2	2
Non-linear dynamics and control	6	2
Distributed control	5	2

2.1. Superconducting Coils

One of the key components of Electromagnetic Formation Flight (EMFF) is the generation of the electromagnetic fields. Relatively large magnetic dipoles are needed to generate the forces used in EMFF. In order to generate these large magnetic dipoles, large high-current electromagnetic coils with many turns must be used. Traditional copper wire electromagnets of these sizes and power levels generate significant heat and have large power requirements due to internal losses. This section looks at the current state of the art in high-current wire technology and investigates the use of high-temperature superconducting (HTS) wire for the EMFF concept.

Limitations of Conventional Wire

Currently, copper and aluminum wire are utilized for high-current applications. Aluminum is typically used when the current is transmitted over long spans such as in high-power transmission because of its strength to weight ratio. For other applications, copper is used due to its low resistively and low cost.

In most applications, wire can be assumed to have nearly zero resistance. However, when used in electromagnetics, the long length of wire makes the resistivity of the wire significant. For copper wire, the resistivity is 17 nohm m. For an EMFF electromagnet, the resulting resistance is on the order of ohms due to the long length of wire that is needed. Since EMFF systems are currently designed to use between tens and hundreds of amps, having a wire resistance on the order of ohms places a power requirement on the order of kilowatts.

This power is actually resistive losses through the wire and points to another drawback of copper wire: heat generation. The power loss due to heat is a function of the length of the wire, its resistivity and the square of the current flowing through it. This lost power is lost in the form of heat that must be radiated away, or else the wire will overheat and begin melting the insulation or wires. The allowable current that can be passed through a copper conductor of a given diameter varies depending on the application, but are typically set at between 5 and 15 Amps/mm². In the case of household wiring, the current is set by the desire to keep the voltage drop per unit length below a nominal value, and results in a current density of about 6-7 Amps/cm². For applications to EMFF, the current density is dictated by the amount of heat that can be dissipated from the wire before it begins to lose structural integrity. Consequently, as the cross section gets larger, the current density that can be supported decreases, unless changes are made to the geometry (increase surface area given the volume) or active cooling is used. Assuming a circular cross section that relies only on radiative cooling, the current density drops as 1/d (reciprocal of the wire diameter). Therefore, the allowable current increases linearly with wire diameter, not with the square of the diameter as would be expected using a constant current density.

The resistivity of the wire is a very important design parameter for EMFF. Because EMFF is a high current application, any resistance causes significant heat generation and power losses. Therefore the design should utilize wire that has the lowest resistance possible.

High Temperature Superconducting Material Overview

The solution to many of the problems encountered with conventional wire is the use of superconducting material. Superconducting material has zero resistance when cooled below a critical temperature. Since the wire has zero resistance there is no thermal heating and no power losses across the wire. Until recently, superconducting material had to be cooled down to less than 10K using liquid helium. However with the innovation of high temperature superconducting (HTS) technology, HTS wire can be manufactured that only needs to be cooled down to 110K which is much higher than the boiling point of liquid nitrogen (77K).

With HTS wire, an electromagnet could be built to any size needed. Since there is no resistance, there is no heat production and a bundle of any size can be made without fear of overheating the wire. Also, since there is zero resistance, it takes a negligible amount of power to produce a high current through the wire. Power is needed to create and change the magnetic field. The only losses are in the power subsystem itself. Therefore the only limitation on the current is the critical current density of the superconducting wire.

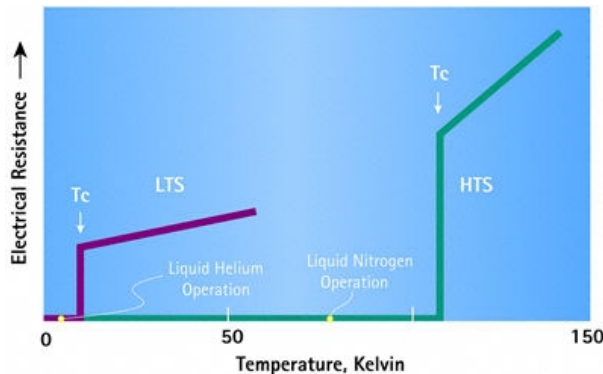


**Figure 2.1.1 Critical Temperature for HTS and LTS material
(Illustration courtesy of American Superconductor)**

First Generation Superconducting Wire Technology

HTS wire has been the focus of many papers and research groups including: the U.S. Department of Energy, the Argonne National Laboratory, the Brookhaven National Laboratory, Los Alamos National Laboratory, Oak Ridge Laboratories, the University of Wisconsin, American Superconductor, IGC-Superpower, and Innova Superconductor Technology. These companies and research labs have researched, designed and improved the making of a durable, high current, superconducting wire out of a material called Bi-2223 which stands for $\text{Bi}_2\text{Sr}_2\text{Ca}_2\text{Cu}_3\text{O}_{10}$. This wire has zero DC resistance and can carry currents 100 times that of the standard copper wire. Figure 2.1.2 shows a standard copper wire and the current HTS wire with the same current carrying capabilities.



Figure 2.1.2 Critical Temperature for HTS and LTS material
(Picture courtesy of American Superconductor)

The HTS wire is manufactured by utilizing a manufacturing technique called powder in tube (PIT) or multi-filamentary composite (MFC) method. The ceramic BI-2223 material is initially placed into long tubes or billets made out of silver. The tubes are sealed and drawn out into long filaments. Several filaments are then bundled together and placed in another tube of silver. This new bundle of wires is once again drawn out to a long length of up to a kilometer, flattened and then heat-treated to react the Bi-2223 material. The result is a thin tape that is composed of multiple superconducting filaments inside a silver matrix. Figure 2.1.3 shows a cross section of the final superconducting wire. The flattened individual filaments can be seen in the close up view of the wire.



Figure 2.1.3 Cross-section of HTS Wire
(Picture courtesy of American Superconductor)

While short segments of this wire have been manufactured with current densities exceeding $70\text{kA}/\text{cm}^2$, current manufacturing techniques allow the wire to be manufactured in long lengths of several hundreds of meters with a current density of upwards of $16\text{kA}/\text{cm}^2$.

The HTS wire is fairly brittle and does not have much intrinsic strength. The wire usually encapsulated between two thin sheets of stainless steel to give the wire strength and durability. This causes the effective current density to decrease due to the added cross-sectional area without added current carrying capabilities. Currently, wire with this added strength have current densities of approximately $11\text{kA}/\text{cm}^2$.

First Generation Superconducting Wire Availability

Currently there are only a handful of companies throughout the world that have the manufacturing capabilities to produce large volumes of superconducting wire. In the United States of America, there is only one company called American Superconductor. The company is headquartered in Westborough, Massachusetts, and they have recently completed their new HTS wire manufacturing plant in Devens, Massachusetts. Currently they are producing HTS wire at a rate of 3000km/year, and their new manufacturing plant has the capabilities of producing wire at a rate of 20,000km/year.

American Superconductor produces two types of wire: high current density superconducting wire, and high strength superconducting wire. The high current density superconducting wire is 4.1mm wide, has a thickness of 0.21 mm, and a critical current of as much as 135 Amps for 200m lengths. The high strength wire is essentially the high density superconducting wire wrapped in a stainless steel sleeve. The resulting wire is 4.1mm wide and 0.30 mm thick, and has a critical current of as much as 135 amps in lengths of over 400m. Longer lengths can be made with smaller guaranteed critical current levels. The HTS wire currently costs approximately \$20-\$25 per meter.

The MIT SSL had the opportunity to visit American Superconductor's manufacturing plant and observe their operations. Also, the MIT SSL, in conjunction with the MIT Aeronautical and Astronautical Engineering's senior design class has obtained over 500m of the HTS wire produced by American Superconductor. The wire has been insulated and made into 0.75 m diameter electromagnet coils and the specifications provided by American Superconductor have been verified.

Second Generation Superconducting Wire Technology

Research and development are continuing on what's called 'second generation' superconducting wire. This wire is constructed using a superconducting material $\text{Y}_1\text{Ba}_2\text{Cu}_3\text{O}_7$. Instead of the wire being extruded many times, the superconducting material is placed on onto a nickel metal alloy tape as a thin film. This technique is still in the development stages. Looking just at the thin film superconducting material, current densities of up to 4000 kA/cm^2 have been achieved.

Because the superconducting film is put on a metal tape of varying size, the current rating for second generation wire is usually given as a current density per cm. To date, the maximum current density has been approximately 200A/cm . This is comparable to the first generation HTS wire, and the wire does not provide for a significant DC performance increase. However, the second generation wire is projected to cost five times less to manufacture making HTS wire more accessible and cost effective. This technology is still in the research and development stage and continues to advance in performance.

Superconducting Technology and the EMFF Concept

Overall, HTS wire is an enabling technology for EMFF. Traditional copper coils are too heavy, require large amounts of active heat dissipation, and require high power to operate. Superconducting wire is 100 times lighter than copper per amperage, require no heat dissipation, and require no power to operate other than the power needed to change the magnetic fields. The drawback to EMFF is the need for a cryogenic system in space. However, similar technology has been flown in space and is covered in more detail later in the report in section 2.4.

2.2. Control Algorithms

There are several aspects that make the control of an Electromagnetic Formation Flight (EMFF) system uniquely challenging. In addition to the novel developments required in hardware technology, such as superconducting electromagnetic actuators or high-precision sensors needed to control relative distances to sub-optical wavelengths, there are certain inherent complexities associated with the control algorithms themselves. Not only must existing algorithms be better understood, but novel algorithms and control methodologies must be developed specifically for application to electromagnetic formation flight systems. These new algorithms may then be extended to find application in other fields.

Some particular challenges of electromagnetic control that must be addressed include:

- the spatial nonlinearity of such a system
- the actuation nonlinearity of such a system

First, we consider the challenge associated with **the spatial nonlinearity** of the proposed EMFF system. As described in the following section, the *forces* between electromagnets are inversely proportional to r^4 , where r is the separation distance between two electromagnets, and the *torques* are inversely proportional to r^3 . Hence EMFF control authority “falls off” rapidly with increased distance between the actuators. This aspect of EMFF control encompasses some unique challenges in the scaling of a system so that the actuators have sufficient control authority over the geometry at hand. For example, in small-scale applications, “traditional” coils (made of copper, for example) or coils with ferromagnetic cores provide sufficient authority. However, for space-scale applications, the spatial nonlinearity and “roll-off” of the actuator authority must be compensated for using novel techniques or state-of-the-art hardware, such as superconducting electromagnets, which are able to provide a much larger current for a given electromagnet-system mass.

In addition to the question of control authority, the spacial nonlinearity raises other issues. For example, to design a linear controller for such a system, the dynamics must be linearized. For such a nonlinear system, the linearized dynamics are accurate only within a very close vicinity of the nominal operating point. Operating beyond this point calls for nonlinear techniques in control design, an area that is much less developed and validated on multi-body space applications.

Second, we consider the challenge associated with **the actuation nonlinearity** of the proposed EMFF system. This nonlinearity arises because of the fact that forces and torques between the spacecraft are generated as a result of a *product* of magnetic moments of the spacecraft. In other words, one actuator has no effect without the other, and generating identical currents in the electromagnets on both spacecraft results in an actuator that varies as a *product* of currents. This poses a challenge, since new techniques must be developed to either linearize the representation of such a system, or to control such a system using novel nonlinear control techniques.

2.3. Power systems

Superconducting wire is an enabling technology of EMFF. The obvious benefit is of course the low power required to generate large magnetic fields. However the large currents that must be generated create a power system requirement that is somewhat foreign to spacecraft systems. The idealized HTS circuit consists of a relatively low voltage supply that can push a very large current through a large inductor with no internal resistance. In the limit where there is no capacitance, the governing equation for the current is

$$L \frac{di}{dt} = V - iR \quad (2.3.1)$$

where R represents the resistance over the entire system outside of the actual coil. The rate at which the current can be changed is therefore determined by the available voltage and the internal resistance. There is a roll-off of the system responsiveness at higher current levels, so that higher frequency variations in current can only be achieved at diminishing amplitudes.

The resistance also represents the only source of actual energy loss, since energy that goes into creating the magnetic field is beneficial. The challenge then is to be able to create a power system with very little internal resistance, and sufficient voltage to maintain the necessary control agility at higher current variations, as governed by the control requirements.

Since the coils must have the ability to be driven in both forward and reverse, the power system will most likely employ some form of H-Bridge. This is shown in Figure 2.3.1 below.

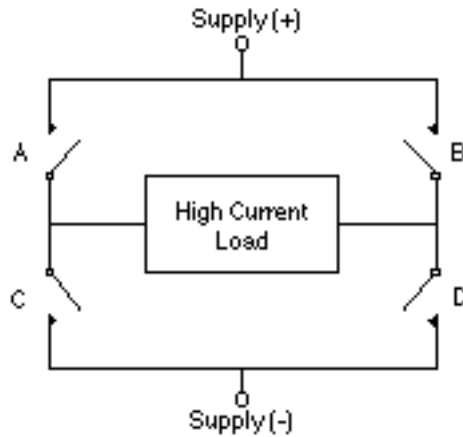


Figure 2.3.1. H-Bridge Circuit

H-Bridges are so common and useful that there are several chips that combine all the discrete components into a single package. An example of such a chip is the SN754410NE made by Texas Instruments. These chips overcome many of the difficulties in designing an H-Bridge out of discrete components such as flyback diodes, voltage drop, and thermal runaway. They also combine all of the discrete components into a single package that is often much smaller than could be accomplished otherwise.

To overcome the voltage drop problem, H-Bridges can use something called a charge pump. A charge pump uses arrays of capacitors to increase voltage in a circuit. This higher voltage can then be used to trigger the bases of the transistor arrays in an H-Bridge. In this way, the voltage of the initiating signal from the logic circuit need not be higher than that of the high-current load being driven. Often this is used in robotics to drive higher voltage loads (often 9, 12, or 24 volts) that run at high current from logic voltages that are typically 5 volts.

Since a single transistor may not provide enough current capacity in an H-Bridge design, several transistors can be used in parallel to achieve the desired voltage capacity. This can become complicated, though, as the least efficient transistor in the parallel array will heat up and in doing so, become even more inefficient. This can lead to a destructive condition called thermal run-away. This is avoided in some designs by using FET transistors that operate on voltage input and not current input.

An H-bridge implemented with transistors allows the high-current load to not only be reversed (using inverted voltage) but also allows very fast switching of the motor current. This rapid switching can be used to control the speed of the motor and is called Pulse Width Modulation or PWM.

Available Options

There are many other options for driving high-current loads from logic. Motor Controllers from the radio control industry offer one option that is designed specifically for handling large high-current loads efficiently. An example of such a device is shown in Figure 2.3.2.



Figure 2.3.2. A Radio Controlled Car Speed Control

<http://www.acroname.com/robotics/info/articles/drivers/speed_cnt.jpg>

Many Radio controlled cars, planes, boats, and even helicopters rely on motor controllers to accomplish the task of driving high-current loads. These motor controllers can handle very large currents of up to hundreds of amps. Also, since running time is important in the radio controlled hobby, these controllers have been designed to be very efficient. These controllers are typically designed around specialized power MOSFET transistors. The circuit is something like a large H-bridge that uses parallel MOSFETs to achieve high currents with high efficiency. Some controllers allow the load to be driven in reverse (voltages are inverted at the outputs). Even others allow breaking of motors by driving both the outputs at the same voltage to "lock up" the motor.

Future Innovations

Since the resistance in the power system typically comes from the source, an anticipated innovation to the high current driving system needed for EMFF is to allow a complete bypass of source during operation. High energy density capacitors are becoming available that are competitive with batteries, but do not suffer the same internal resistance problems. A separate charging circuit can be used to charge these capacitors at a lower current, reducing the power losses in the system. Then during operation, energy is simply exchanged between the electric field of the capacitors and the magnetic field of the coils. Designing the circuit to recover the energy in the fields, rather than dissipate it, will greatly reduce the required power levels to drive the coils for EMFF, making them virtually negligible compared to other systems.

2.4. Thermal

Another system that is necessary for EMFF is the cryo-cooling. An example of a cryo-cooler is shown below in Figure 2.4.1.

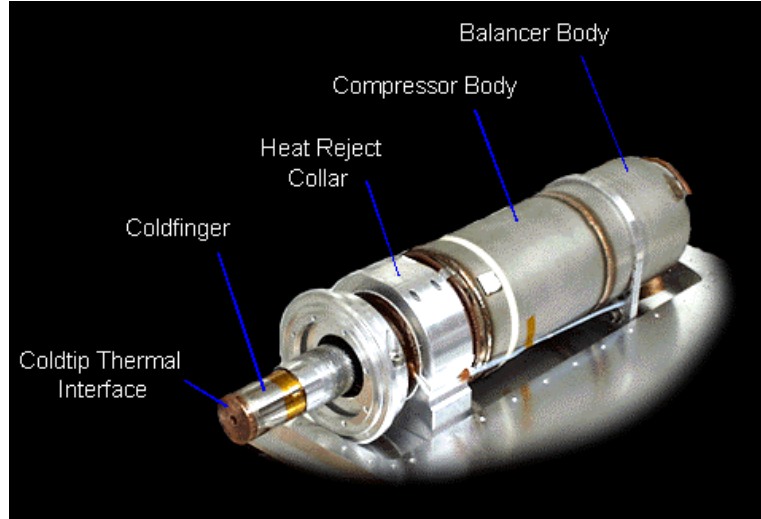


Figure 2.4.1. Cryo-cooler Designed to Maintain 77 K

<Courtesy <http://hessi.ssl.berkeley.edu/instrument/cryocooler.html>>

Recently, under contract to NASA/GSFC, Sunpower Inc. has developed an inexpensive single stage, integral (counterbalanced) Stirling cycle cooler that can provide up to 4W of cooling at 77 K, with an input of 100W. This M77 cryocooler has been designed for operational lifetimes greater than 50,000 hours, using a gas bearing/flexure system to prevent contact of moving parts. In extensive studies over the past two years at GSFC, M77 coolers have been vibrated to the GEVS mandated 14.1 Grams, run under thermal vacuum conditions from -25C to +30C, and life-tested already (continuing) for \sim 10,000 hrs. Monitoring during these tests showed no internal contamination of the working gas. Units already tested at GSFC are fully qualified for flight, and will be used for HESSI.

Although the technology itself is at TRL 9, the application to EMFF will still require significant advancement. For one, the heat transfer rate from an extended HTS wire coil will most likely be higher than the 4 W level that the system shown can provide, given that the entire coil containers may be exposed to the sun in some applications. Also, due to the extent of the coil, a circulating fluid may be necessary to keep the entire coil at the low temperatures.

The paradigm for instrument cooling has typically been to focus the cooling on specific instruments, such as discussed above. However, with future missions that could use EMFF as a technology, 90% of the spacecraft must actually be kept at temperatures that are sufficient to operate HTS wire. These are missions where the apertures themselves must be kept cool to limit the amount of thermal noise that is introduced into the optical path. For these missions, the introduction of EMFF can be done at nearly no cost, other than the necessary support structure. If eventual use of EMFF in more generic applications is the goal, then a more self-contained method of keeping the coils cool is necessary.

2.5. Shielding

Although very intense magnetic fields may not be needed, fields that are significantly higher than the Earth's can certainly be expected within the volume enclosed by the coils in an EMFF enabled spacecraft. During the phase I research, NASA and industry reports were reviewed in an attempt to find specifications of maximum field intensity for standard equipment. Sources commonly cited as generating fields are:

- Magnetic latching relays
- Traveling wave tubes
- Tape recorders

- Coaxial switches
- Transformers
- Solenoid Valves
- Motors

However, nothing was found to cause fields over 1000 Gauss (0.1 Tesla). Equipment that is traditionally known to be susceptible to magnetic effects include:

- Magnetometers
- Photomultipliers
- Image-dissector tubes
- Magnetic Memories
- Low-energy particle detectors
- Tape Recorders

In addition, the Digicon detectors in Hubble FOS and Quartz-crystal oscillators were found to be vulnerable to magnetic effects. Other effects may come into play that are negligible at low field strengths, such as eddy currents in metal harnesses, Hall effects in conductors, and possibly effects in semiconductors. More research is necessary to find existing information on some of these systems, but ultimately tests will need to be conducted to determine susceptibility.

Passive Shielding

To protect hardware that is susceptible may require some form of passive or active magnetic shielding. Passive shielding, consisting of high permeability metals enclosing the equipment, will attenuate a DC magnetic field according to the relationship

$$A = \frac{\mu \Delta}{2 R} \quad (2.5.1)$$

where μ is the permeability of the material, Δ is the thickness, and R is the characteristic radius of enclosure. Attenuation is the multiplier that relates the field intensity outside the enclosure to that inside, so that a higher value offers better protection. Some high permeability materials are given below in table 2.5.1.

Table 2.5.1. Some High Permeability Materials and Their Properties

Material	Density (lbs/cu-in)	Permeability	Saturation (G)
Amumetal	0.316	400000	8000
Amunickel	0.294	150000	15000
ULCS	0.0283	4000	22000

As an example, reducing a 600 G (0.06 T) field to ambient (0.3 G) requires an attenuation of 2×10^3 , or a minimum D/R of 0.01. This is 0.1 mm thickness for each 10 cm or radius enclosed. In addition to the scaling relationship for shielding, there are a number of other practical considerations related to shielding.

- Geometry
 - Shielding acts to divert field lines around components
 - Gentle radii are better for re-directing field lines than sharp corners
- Size

- Smaller radii are more effective, so shielding should envelop the component to be protected as closely as possible
- Continuity
 - Separate pieces should be effectively connected either mechanically or by welding to insure low reluctance
- Closure
 - Components should be completely enclosed, even if by a rectangular box to shield all axes
- Openings
 - As a rule, fields can extend through a hole ~5x the diameter of the hole
- Nested Shields
 - In high field areas, multiple shield layers with air gaps can be used very effectively. Lower permeability, higher saturation materials should be used closer to the high field regions

Active Shielding

In addition to passive shielding, large regions of relatively uniform magnetic field strengths can be actively shielded using Helmholtz coils. This is often done in laboratory environments to eliminate the Earth's field when conducting experiments that are highly susceptible to magnetic fields. The general arrangement is shown schematically in Figure 2.5.2.

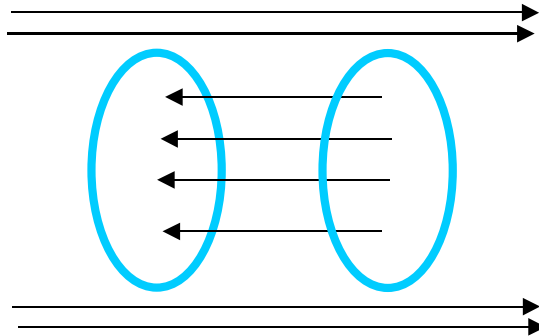


Figure 2.5.2. Helmholtz Coils Nullifying a Uniform Magnetic Field

The small coil size (relative to the main coils) requires proportionally smaller amp-turns to achieve nulling of the field. The small flux such an arrangement means that the main field will not be significantly affected by such an arrangement. A more quantitative study of the effects of both passive and active shielding on the external field is necessary.

3. FEASIBILITY STUDY SUMMARIES

In the previous section, we defined some of the most challenging aspects of the EMFF concept that must be investigated. In this section, we summarize the results of studies we have performed to investigate the feasibility of these enabling technologies. Detailed work will be referenced in appendices following the body of this report.

3.1. Magnetic Interaction

Overview

This section will describe the interaction between two electromagnets. While intuitively it may seem that magnets would only have the ability to push and pull another magnet, they are also capable of producing ‘shear’ forces. These shear forces move the satellites perpendicular to the line between the two satellites. Thus the satellites will have the ability to move relative to each other in all directions.

Along with forces, magnets also produce torques. For a system with no external torques, any rotation of the formation will cause the individual satellites to rotate in the opposite direction in order to conserve angular momentum. Reaction wheels must be used to absorb this angular momentum and control the satellites’ angular positions. The following sections will describe two different methods of modeling the forces and torques between two electromagnets.

Magnetic Forces (Near Field)

In order to calculate the forces between two satellites using EMFF, we need to step back and start with the force calculation between two current loops. Figure 3.1.1 shows two current loops of arbitrary shape and orientation. The forces between the two current loops will always be equal and opposite. Also, since there are no outside forces acting on the two current loops, their center of mass will remain unchanged.

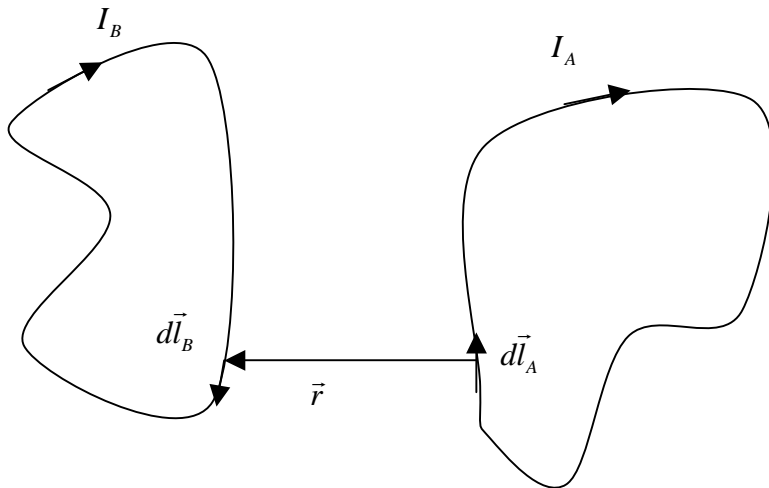


Figure 3.1.1: Two Current Loops

The force between the two current loops is given by the formula:

$$\vec{F}_{AB} = \frac{\mu_0}{4\pi} I_A I_B \iint \frac{d\vec{l}_B \times (d\vec{l}_A \times \vec{r})}{|\vec{r}|^3} \quad (3.1.1)$$

where μ_0 is a constant with a value of $4\pi \times 10^{-7}$. Because the electromagnets used in EMFF are shaped as circles, we can simplify equation (3.1.1). However, analytical expressions can still only be obtained for the special circumstance

where the two circular loops have their axis aligned. Even then, the solution is composed of elliptical integrals. For all other situations, a double numerical integration must be completed to calculate the forces between the coils. While complex and difficult to integrate, the formula exactly calculates the forces between two current loops, and serves a benchmark for other approximate methods. Because this formula works for all separation distances even in the near field, it is called herein as the Near Field Model.

Far Field Model: Magnetic Dipoles

While Equation 3.1.1 provides for an exact solution to the force between two loops of current, it does not provide for an intuitive feel of how the magnetic forces scale or change with different configurations. In order to obtain these answers, the model must be simplified.

The simplest model of a current loop is a magnetic dipole. Many magnetic devices can be approximated by a magnetic dipole including: permanent magnets, bar magnets, solenoids, and loops of current. For a loop a current, the magnetic dipole is given by the formula:

$$\vec{\mu} = N i A \hat{n} \quad (3.1.2)$$

where N is the number of turns in the coil, i is the current, A is the area enclosed by the coil loop, and \hat{n} is the unit vector pointing perpendicular to the current loop and follows the right hand rule for the current direction.

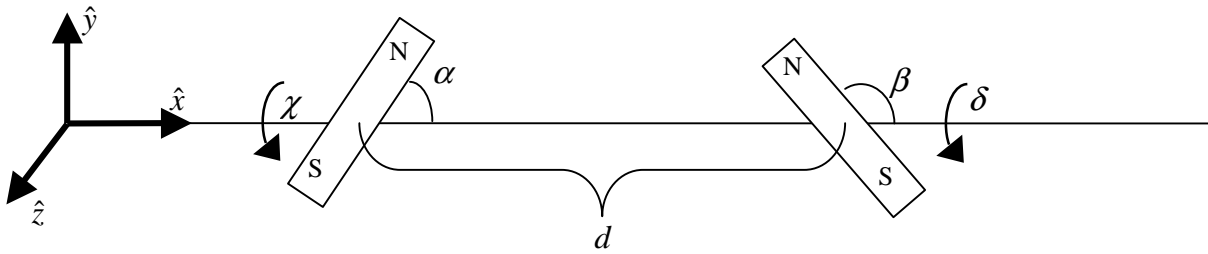


Figure 3.1.2: Schematic of Two Magnetic Dipoles

Figure 3.1.2 shows two magnetic dipoles in an arbitrary configuration (represented here as bar magnets). The two dipoles lie on the x axis. The angles α and β represent the rotation of the dipoles about the \hat{z} axis, and the angles χ and δ represent rotations about the \hat{x} axis. The order of rotation is \hat{z} axis followed by the rotation about the \hat{x} axis. Using the far field approximation, the forces and torques on the left dipole due to the right dipole will now be calculated. For a more detailed explanation see Appendix A.

The dipole angles can be thought either as bar magnets that are physically pointed, or as three orthogonal current coils that can electrically steer an effective dipole. Regardless of the way the dipole is created, the resulting equations can be used.

Using the Far Field assumption where the distance between the dipoles is great compared to the dipole length, the following approximation can be used to calculate the force and torques on the dipole A:

$$\begin{aligned} \vec{F}_A &= -\nabla U_A = \vec{\mu}_A \cdot \nabla \vec{B}_B = \frac{3\mu_0}{4\pi} \left(-\frac{\vec{\mu}_A \cdot \vec{\mu}_B}{r^5} \vec{r} - \frac{\vec{\mu}_A \cdot \vec{r}}{r^5} \vec{\mu}_B - \frac{\vec{\mu}_B \cdot \vec{r}}{r^5} \vec{\mu}_A + 5 \frac{(\vec{\mu}_A \cdot \vec{r})(\vec{\mu}_B \cdot \vec{r})}{r^7} \vec{r} \right) \\ \vec{T}_A &= \vec{\mu}_A \times \vec{B}_B = \vec{\mu}_A \times \frac{\mu_0}{4\pi} \left(\frac{\vec{\mu}_B}{r^3} + 3 \frac{(\vec{\mu}_B \cdot \vec{r})}{r^5} \vec{r} \right) \end{aligned} \quad (3.1.3)$$

Substituting in the vectors of the magnetic dipoles as described by Figure 3.1.2, the forces and torques can be re-written as:

$$\begin{aligned}
F_x &= \frac{3}{4\pi} \frac{\mu_0 \mu_A \mu_B}{d^4} (2 \cos \alpha \cos \beta - \cos(\delta - \chi) \sin \alpha \sin \beta) \\
F_y &= -\frac{3}{4\pi} \frac{\mu_0 \mu_A \mu_B}{d^4} (\cos \alpha \sin \beta \cos \delta + \sin \alpha \cos \beta \cos \chi) \\
F_z &= -\frac{3}{4\pi} \frac{\mu_0 \mu_A \mu_B}{d^4} (\cos \alpha \sin \beta \sin \delta + \sin \alpha \cos \beta \sin \chi) \\
T_x &= -\frac{1}{4\pi} \frac{\mu_0 \mu_A \mu_B}{d^3} (\sin \alpha \sin \beta \sin(\delta - \chi)) \\
T_y &= \frac{1}{4\pi} \frac{\mu_0 \mu_A \mu_B}{d^3} (\cos \alpha \sin \beta \sin \delta + 2 \sin \alpha \cos \beta \sin \chi) \\
T_z &= -\frac{1}{4\pi} \frac{\mu_0 \mu_A \mu_B}{d^3} (\cos \alpha \sin \beta \cos \delta + 2 \sin \alpha \cos \beta \cos \chi)
\end{aligned} \tag{3.1.4}$$

With this new simplification, the forces and torques can be easily calculated for any dipole configuration. This is much simpler than the double integral equation, but these equations are only valid in the far field. See Appendix A for a comparison between the near field model, and the far field model.

An Intuitive Look

Using Equation 3.1.4, it's useful to gain an intuitive feel of how magnetic dipoles react around each other. The magnetic dipole is dual to an electrostatic dipole, and can be thought of as a North Pole and a South Pole. Using this analogy, one is reminded of the saying "Like repels, opposite attracts". The left side of Figure 3.1.3 shows two dipoles (represented schematically as bar magnets) with their axes aligned. Substituting in values of $\alpha = \beta = \chi = \delta = 0^\circ$ into equation (3.1.4), the force between these two magnets is given by the equation:

$$F_{axis} = \frac{3\mu_0}{2\pi} \frac{\mu_A \mu_B}{d^4} \tag{3.1.5}$$

From this equation we see that the attractive (or repelling) force between the two magnets is a function of the product of the two dipole strengths and inversely proportional to the distance between the dipoles to the fourth power. The presence of the product of the magnetic dipoles demonstrates the coupled nature of EMFF. No satellite can move on its own. Every satellite must work in tandem with every other satellite in the formation to perform a maneuver. For formations with many satellites, this coupled nature adds to the complexity of the control problem.

The inverse scaling with the distance to the fourth power is a drawback to magnetic dipoles. This rapid fall of the magnet strength causes the magnets to be large for large satellite separation. However, the fast fall off does help simplify the control problem as satellites that are farther away will have a negligible effect on a satellite compared to a satellite nearby. Therefore, for large satellite formations a control algorithm may only need to worry about the magnetic field produced by its closest neighbors and not the magnetic field of every satellite in the fleet.

The right side of Figure 3.1.3 shows two dipoles with one dipole oriented perpendicular to the other. The resulting forces and torques are shown. The shear forces are created because the S on magnet B repels the S on top of magnet A and attracts the N on the bottom of magnet A causing an upward force on magnet A and a downward force on Magnet B. The N on magnet B acts in an opposite, causing a downward force on magnet A and an upward force on magnet B. However since the N is farther away than the S from dipole A, the resulting net force pushes magnet A upwards and magnet B downwards. The forces on these magnets are equal and opposite, perpendicular to the line connecting the two magnets and are exactly half the axial force given in Equation 3.1.5:

$$F_{shear} = \frac{3\mu_0}{4\pi} \frac{\mu_A \mu_B}{d^4} \tag{3.1.6}$$

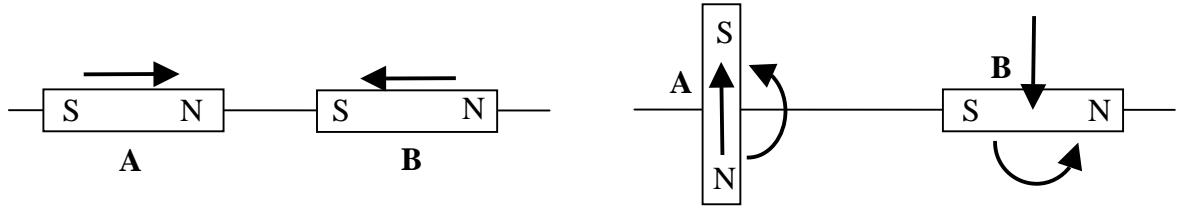


Figure 3.1.3: Resultant dipole forces of two dipoles with their axis aligned (left) and perpendicular (right)

With the ability to produce shear forces as well as attractive forces, electromagnetic dipoles are able to achieve all relative translational degrees of freedom. A spectacular example of this is described later in Section 3.3 where systems of 5 satellites are spun up from rest.

With the ability to produce shear forces comes the side-effect of producing a torque on the individual dipoles. This side effect is due to the conservation of angular momentum. As the two dipole move perpendicular to the line connecting them due to the shear forces, they actually begin rotating around the system center of mass. Since there are no outside forces, the angular momentum must be conserved, and it is conserved by the change in angular momentum of the individual dipoles due to the torques applied. This torque is not the same for both dipoles; in the configuration on the right side of Figure 3.1.3, the torque on dipole B is exactly half of that on dipole A.

The torque on each satellite is given as:

$$\begin{aligned}\tau_A &= \frac{3\mu_0}{6\pi} \frac{\mu_A \mu_B}{d^3} \\ \tau_B &= \frac{3\mu_0}{12\pi} \frac{\mu_A \mu_B}{d^3}\end{aligned}\quad (3.1.7)$$

The dipoles can be arranged in more than just the perpendicular configuration on the right side of Figure 3.1.3 and still produce pure shear. Looking at equation (3.1.4), the axial forces can be set to zero, and the resulting angles can be solved for:

$$\begin{aligned}F_x &= 0 \\ \therefore \alpha &= \pm \cos^{-1} \left(\pm \frac{\sqrt{2} \sin \beta}{\sqrt{5 + 3 \cos(2\beta)}} \right)\end{aligned}\quad (3.1.8)$$

We can now plot the angle α , and the torque distribution as a function of the angle β , as shown in Figure 3.1.4. As we vary the angles of the dipoles, the torque distribution between the two satellites changes. This extra degree of freedom allows for the ability to selectively choose the distribution of the angular momentum gain between the two satellites. There is only a slight performance decrease in the shear forces for the non-perpendicular case.

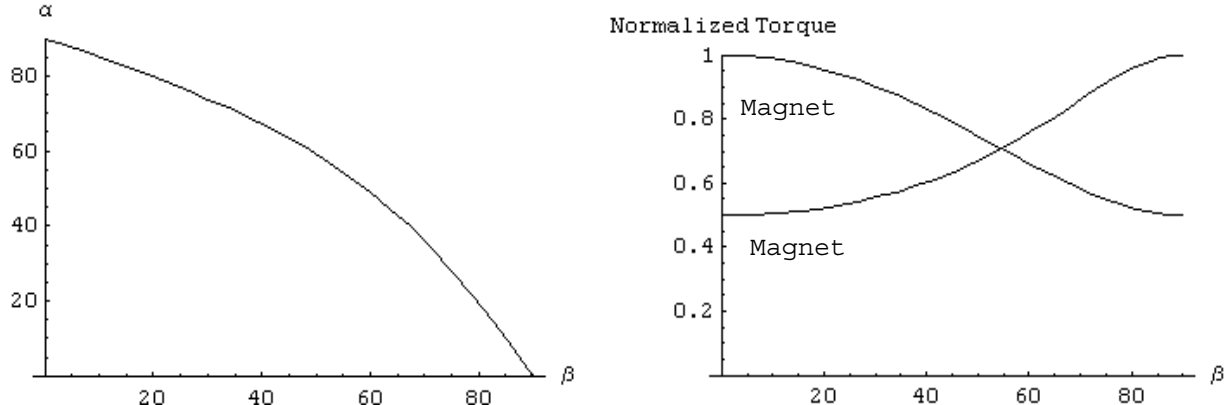


Figure 3.1.4: Plots of α and the torque distribution for varying β

Overall, in conjunction with reaction wheels, electromagnets provide the ability to move a satellite relative to another satellite.

3.2. System Trades

To determine the feasibility of retrofitting current NASA missions with EMFF, an analysis to determine the optimal system sizes for a three spacecraft TPF mission at a 25 m baseline was conducted. Room temperature copper coils were used along with a spacecraft dry mass of 600 kg and spacecraft size of 2 m. The coils are assumed to wrap around the outside of the spacecraft and have similar radius to the current spacecraft radius. The current mass of the TPF propulsion system, 400 kg, was replaced by an electromagnet system of same mass. Figure 3.2 shows the array rotation rate versus the total array mass distribution for varying electromagnet system masses. For an electromagnet system of 400 kg, the mass of the center spacecraft should be approximately half the total system mass. The two dotted lines indicate rotation rates of 1 revolution every 2 hours, the goal of TPF, and 1 revolution every 8 hours, the current state of TPF. Clearly retrofitting TPF with an EMFF system has the ability to achieve the goal rotation rate, but also reduce the propulsion system mass by approximately 150 kg. By rotating at a higher rate and reducing system mass, an EMFF design can enable TPF and future space interferometers to increase science productivity and cut costs.

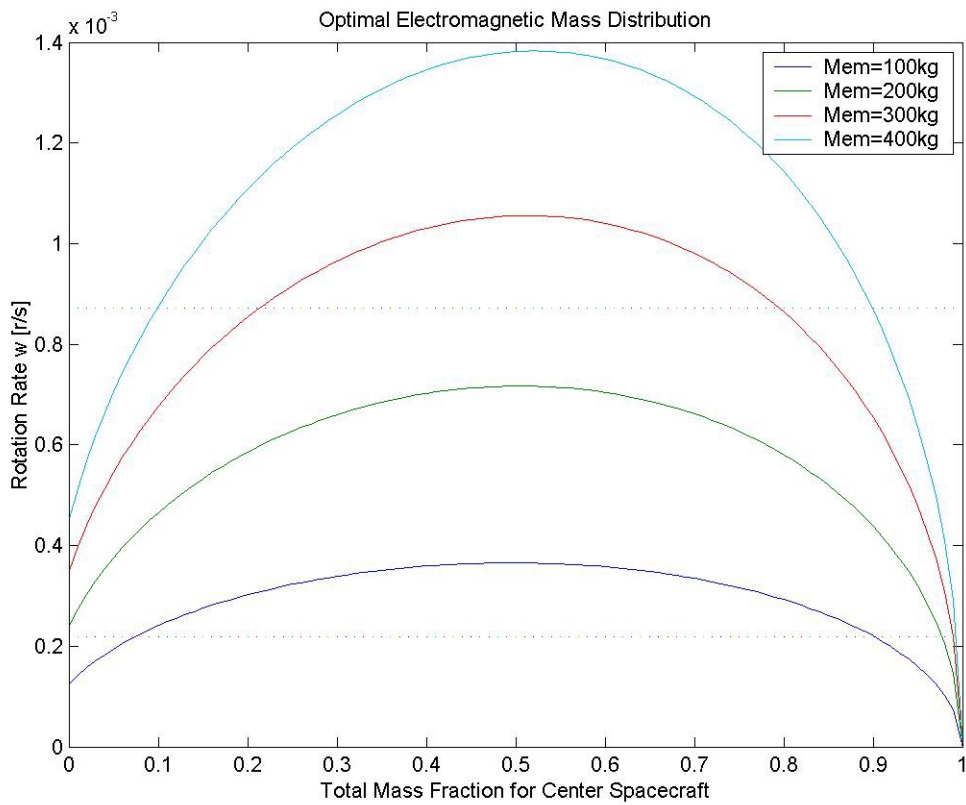


Figure 3.2: Mass Distribution of a Three Spacecraft Array

3.3 Control analysis

This Electromagnetic Formation Flight (EMFF) study seeks to develop multiple satellite formation control strategies that exploit electromagnetic forces between spacecraft to control formation geometry. EMFF, in concert with reaction wheels, will control relative positions and orientations between spacecraft through the use of a renewable energy source: electrical power. Various electromagnet geometries, such as dipole or “quadrupole” topologies, allow an increasing variety of relative degrees-of-freedom between spacecraft to be controlled without the expenditure of propellant. This section investigates the use of multiple electromagnetic dipoles and reaction wheels for relative position and orientation maintenance and array spin-up, as needed for future space-based interferometers.

Control analysis and design for EMFF applications is an extremely challenging aspect of this study. In fact, the viability of EMFF depends largely upon the ability to successfully control such a system with nonlinear and unstable dynamics. Hence a large effort has been put toward studying the feasibility of control in several proposed configurations. Figure 3.3.1 shows a list of the configurations that have been considered during Phase I of this study. Control

	2-D	3-D
Dynamics Analysis		
Spin-Up Control		
Steady-State Spin Control		

Figure 3.3.1 EMFF Geometries and Operational Modes Considered in this Study

design and analysis progress naturally from simpler, less complicated geometries to more complex ones; we have attempted to investigate the feasibility of the EMFF control concept each step along the way.

Figure 3.3.3 shows a schematic of a planar (two-dimensional), two-spacecraft array. The yellow arrows in the diagram represent forces and torques on each spacecraft due to the interaction with the other spacecraft’s electromagnet. The blue arrows represent torques imparted on each body due to a spinning reaction wheel. In the following section, we study the feasibility of control using various combinations of these actuators by checking for the “controllability” of systems with various geometries.

Small Perturbation Control Theory

The future Terrestrial Planet Finder (TPF) interferometer is an infrared detection system. To adequately detect a planet, the optical system of the interferometer must be controlled to at least an order of magnitude less than the observation wavelength (μm). This precision control will be achieved through the use of a multi-stage control system: coarse-level control that ranges from meter to centimeter levels of authority, medium-level control (optical delay

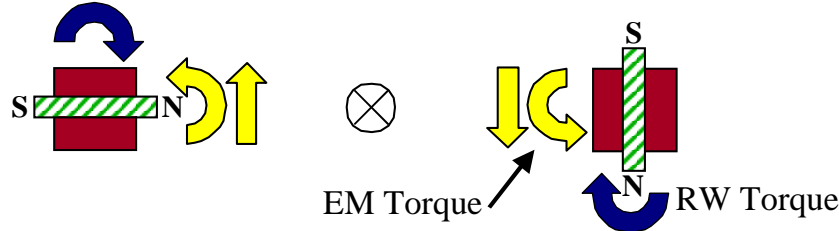


Figure 3.3.2 Schematic of Planar, Two-Spacecraft EMFF Array with Electromagnets and Reaction Wheels as Actuators

lines) that ranges from centimeter to micrometer levels, and fine-level control (fast steering mirrors) that ranges from micrometer to nanometer levels. This work proposes using EMFF in place of traditional thrusters to provide the course-level disturbance rejection capability in such systems.

In Appendix C, the requirements to reject small perturbations using only the proposed EMFF concept are determined in detail. The main steps involved are:

1. A general kinematic formulation for a multi-spacecraft multipole system is developed, based on an electrostatic analogy.
2. From these kinematic relationships, a state-space representation of the system is determined, specifically the dynamic (**A**) and control (**B**) matrices.
3. Using these matrices, the controllability of the system is determined to ensure that the given actuators (electromagnets and reaction wheels) can adequately reject disturbances in all the required degrees of freedom.

The general multi-spacecraft multipole system is shown in Figure 3.3.3. In this formulation, a system of M spacecraft, each with N magnetic poles, is considered. The results of this study are summarized here.

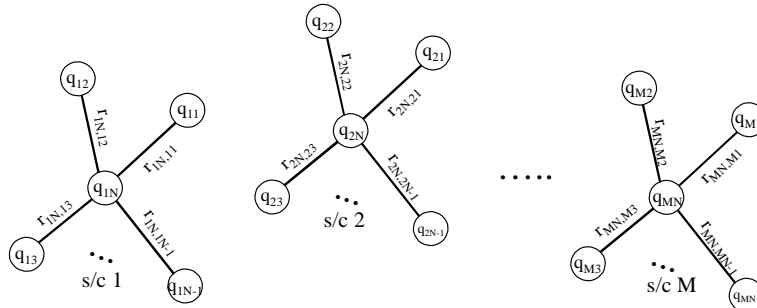


Figure 3.3.3 Multi-spacecraft multipole electromagnets.

Dipole

For a two-spacecraft array with the dipole axes aligned with each other in a two-dimensional plane, as shown in Figure 3.3.17, there should be eight state variables characterizing the system: two for the relative x and y positions within the plane of the array, two for the corresponding velocities, one each for the rotation of each spacecraft about the z axis perpendicular to the plane, and one each for the corresponding rotation rates.

The **A** and **B** matrices for this two-spacecraft dipole example, derived Appendix C, are tested for controllability and show that the given actuators are not sufficient to make this system controllable. With the axes of the dipoles aligned, one can intuitively understand this, since only the position and velocity along the line connecting the spacecraft can be controlled by varying the currents in the electromagnets. This confirms that it is not possible to control eight states with only two control variables.

Y-pole

Instead of dipoles, now consider a two-spacecraft system with *three* poles each. The poles are arranged so that they are evenly distributed at 120° apart, and this configuration is referred to as a Y-pole. In this case, the system is found to be controllable. Compared to the dipole case, two more control variables have been added, while the number of state variables remains the same. Hence this actuation scheme is adequate to control the two-spacecraft Y-pole system.

Case Study: NASA's Future Terrestrial Planet Finder Mission

Extending the analysis to NASA's future five-spacecraft TPF interferometer, full controllability of the interferometer in two-dimensional space is only achieved in the case when all the spacecraft have Y-poles.

Further extending the analysis to TPF interferometer in three-dimensional space indicates that a four-pole configuration must be implemented before full controllability of the interferometer can be achieved. Note that the four poles must be arranged such that they are not contained in the same plane. A possible configuration is to place the nodes on the vertices of a triangular-based pyramid.

Dynamics and Control Theory

A candidate operations mode for an interferometric TPF architecture is to place four collector and one combiner spacecraft along a single baseline vector (array maintenance mode). This one-dimensional array is then angularly accelerated about the line-of-sight to the parent star (spin-up mode). Once the array is rotating at the appropriate angular velocity, the requisite centripetal force must be provided to maintain that steady-state spin rate (steady state mode).

One-Dimensional Steady-State Spin Dynamics and Control

A steady-state spin maneuver (Figure 3.3.4) requires a careful force balance in which the electromagnetic force between the spacecraft must provide the centripetal load required to maintain the spacecraft in a steady spin motion. If this balance is perturbed, the system will respond with a certain dynamic behavior that will need to be controlled. For example, if the spacecraft move apart, the electromagnetic force will drop faster than the centripetal load, causing the spacecraft to continue to separate. This corresponds to an unstable or divergent mode. Modeling these dynamics allows us to derive the needed control.

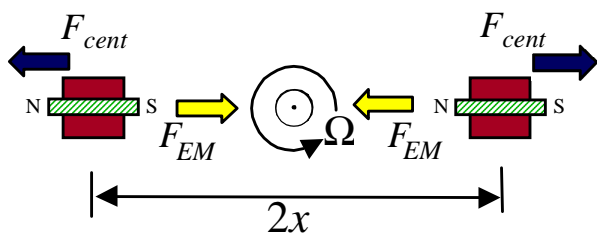


Figure 3.3.4 Two spacecraft with electromagnets undergoing steady-state spin about the system center of mass.

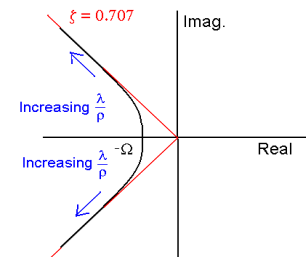


Figure 3.3.5 Closed-loop pole trajectories for increasing gain.

The admits of such a system are modeled in detail in Appendix D and are indeed found to be both nonlinear and unstable, with poles at $\pm\Omega$, where Ω is the spin-rate of the array. The nonlinear dynamic equations are then linearized assuming a nominal spacecraft separation distance and spin rate, and an optimal controller is designed.

To develop this controller, a cost function is created to weigh the importance of different parameters, then minimized to solve for the optimal control. Within this cost function, a weight λ is placed on the relative distance, and a weight p is placed on the amount of control used. (Because the controller commands current to be supplied to the actuators, and the optimal control method used is a quadratic cost minimization, the actuator *power* is penalized by the weight p .)

The detailed derivation and resulting optimal control gains are shown in Appendix D. An interesting result of this study, however, is shown in Figure 3.3.5. We find that if the ratio λ/ρ is evaluated from 0 to ∞ , a graph of the closed-loop poles for the most efficient controller can be created. When the ratio is zero, use of control is infinitely expensive, yet control effort must be expended to stabilize the unstable pole. Therefore, both poles are both located at $-\Omega$. When the ratio tends toward infinity, use of control becomes cheap, and the closed loop poles move out to infinity along 45° asymptotes, where the damping ratio is 0.707. The stabilization of these unstable open-loop dynamics is one of the challenges in electromagnetic formation flight.

Control Experiments

The control analysis in the previous section demonstrates some interesting characteristics of a rotating formation flight cluster. Of particular interest is the fact that a two-satellite cluster has open-loop poles that are real and equal to the positive and negative values of the spin rate, $+\Omega$ and $-\Omega$, respectively. Hence the rotating system is unstable, with one pole lying in the right-half complex plane.

Without a multi-body testbed on which to perform experiments, it is difficult to demonstrate closed-loop, stable control of an inherently unstable spinning cluster. However, if we can demonstrate control of an unstable system *with similar dynamics to the rotating cluster*, we will gain confidence in our ability to use electromagnetic control for disturbance rejection in rotating clusters. We now consider such a system: a linear airtrack that can be configured in either a *stable* or *unstable* geometry.

Airtrack Description

The airtrack, shown in Figure 3.3.6, is a one-dimensional platform on which bodies are allowed to translate, while constrained to linear motion. The bodies are levitated by compressed air flowing through small holes in the track surface, and thus “float” on the nearly frictionless surface.

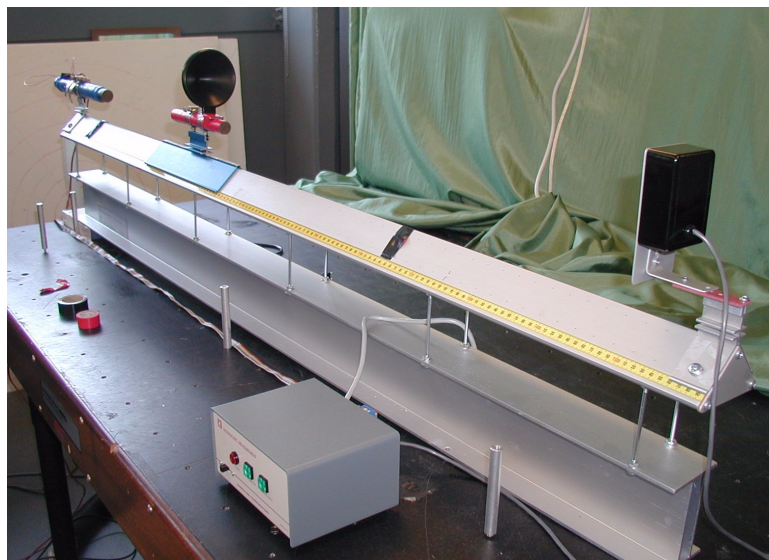


Figure 3.3.6 Airtrack used to demonstrate electromagnetic control of stable and unstable systems.

If electromagnets are placed on the airtrack, they can be used to create forces to attract or repel one other, thus controlling their relative distance. If, instead, an electromagnet is fixed to one end of the track and a permanent magnet is allowed to translate along the track, the fixed electromagnet can be used to control the separation distance of the free permanent magnet, while eliminating any wires that would be connected to the free magnet, and thus avoiding corruption of its nearly frictionless dynamics. Figure 3.3.6 shows an electromagnet fixed to the far end of the track and a permanent magnet on a “slider,” free to translate along the track. The fixed electromagnet is composed of cop-

per wires wound several times around an iron core. Control is thus modulated by running current through the wire, and the direction and magnitude of the current determine the direction and magnitude of the force between the two magnets.

Since the goal is to implement feedback control, a sensory measurement of the distance between the two magnets is required. This is provided by an ultrasonic displacement sensor, shown fixed to the near end of the track in Figure 3.3.6. The transceiver emits an ultrasonic signal, which reflects off the cone attached to the free magnet. The transceiver receives the reflected signal and calculates the distance at a 30 Hz update rate, based on the speed of sound and the time of flight. The separation distance between the two magnets is then computed by subtracting the measured distance from the length of the airtrack.

Finally, to implement feedback control, a real-time computer is used to process the sensor data, compute the required control, and output the control signal through an amplifier to the electromagnet. dSPACE hardware and software were used with a desktop computer for both data acquisition and real-time control. Figure 3.3.7 shows a virtual control panel designed for this system. It allows the user to monitor variables such as the measured distance, the separation distance between the magnets, and both the raw and amplified control signal. It also allows one to tune the various control gains using virtual knobs or numeric inputs.

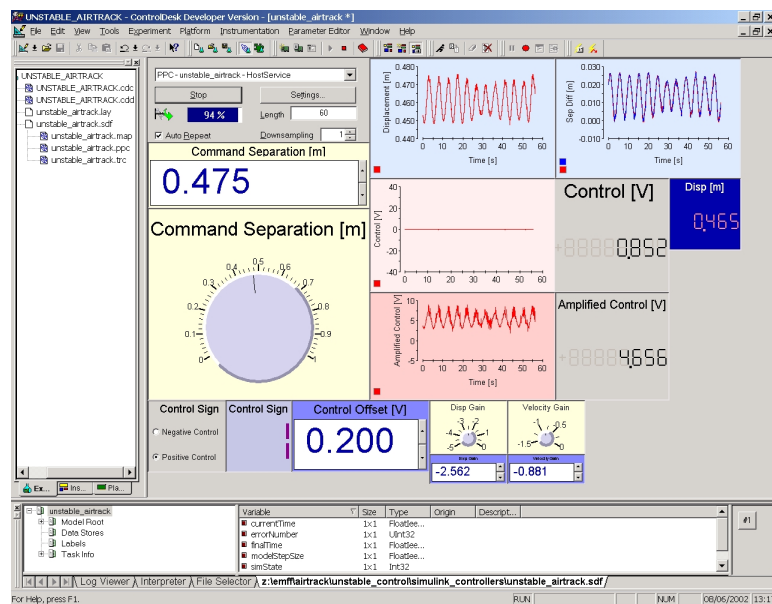


Figure 3.3.7 Sample virtual control panel used with airtrack system.

Stable Airtrack

A schematic of the stable airtrack configuration is shown in Figure 3.3.8. One electromagnet is fixed to the end of the track, another electromagnet is free to float along the length of the track, and the track is inclined so that the free magnet lies above the fixed magnet. (Figure 3.3.8 is exaggerated; the actual inclination used in these experiments is roughly two degrees.) The free magnet tends to fall toward the fixed magnet because of the gravitational force acting on it. The magnets must then repel each other in order to maintain a fixed separation distance while counteracting the gravitational force and other disturbances. The goal for this configuration is to control the separation distance between the two magnets as precisely as possible, while rejecting disturbances to the system.

A detailed derivation of the dynamic equations of motion is provided in Appendix E, along with a control design similar to the design for the steady-state spin system. Figure 3.3.9 shows the poles of the stable airtrack system, as measured from the impulse response. Very light damping due to slight friction from the airtrack surface was neglected, so that the system poles lie approximately on the imaginary axis, at $\pm 1.82j$. Substituting these measured values in place

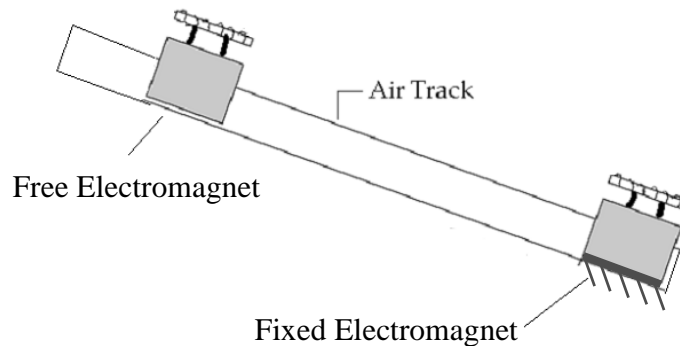


Figure 3.3.8 Schematic of the stable airtrack configuration.

of the analytical poles above, and specifying a control penalty four times that of the displacement penalty ($\lambda/\rho = 1/4$), yields the optimal displacement and velocity gains for the stable airtrack configuration.

This analysis was adapted to the configuration where the free body is a permanent magnet. The resulting open- and closed-loop step responses are shown in Figure 3.3.10, where the separation distance between the fixed and free magnets is plotted as a function of time. As expected, the open-loop response is very lightly damped, making the system slightly stable, instead of neutrally stable. The closed-loop response shows an improvement on the open-loop behavior: the overshoot is reduced and the damping is greater, yielding a much smaller settling time than the open loop response. There is room for improvement, however, since the “steady-state” behavior is still quite noisy, with a ~5 cm (or ~10%) oscillation about the steady value. This has been attributed to a noisy displacement sensor and model error; work is in progress to improve the sensor signal and the control implementation.

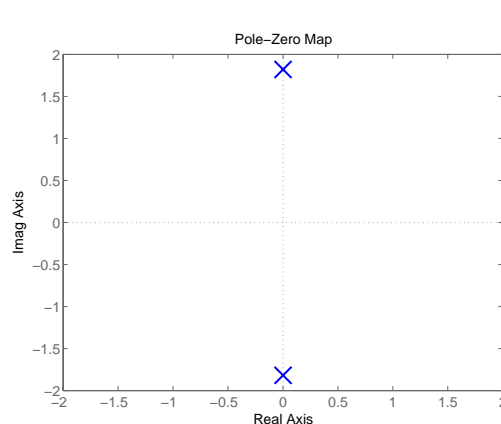


Figure 3.3.9 Stable pole locations in the complex plane.

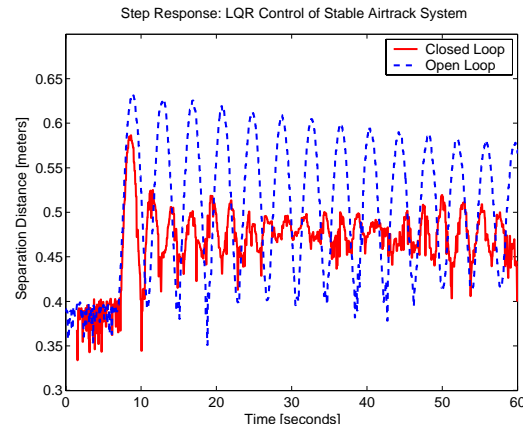


Figure 3.3.10 Open- and closed-loop step responses of stable airtrack.

Unstable Airtrack

A schematic of the unstable airtrack configuration is shown in Figure 3.3.11. In this case, the track is tilted in the opposite manner from the stable configuration; the fixed magnet now lies above the free magnet, so that the free magnet tends to fall *away* from the fixed magnet because of the gravitational force acting on it. The magnets must then

attract each other in order to maintain a fixed separation distance while counteracting the gravitational force and other disturbances.

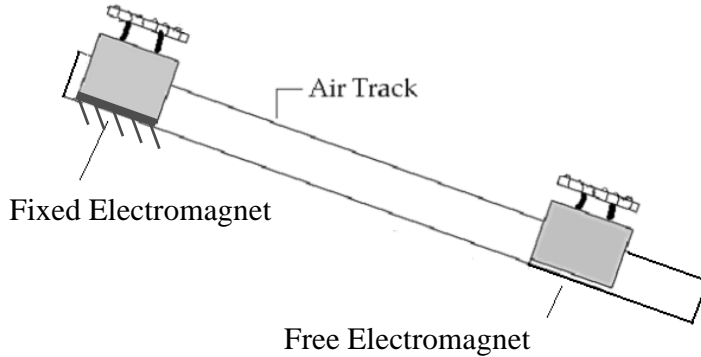


Figure 3.3.11 Schematic of the unstable airtrack configuration.

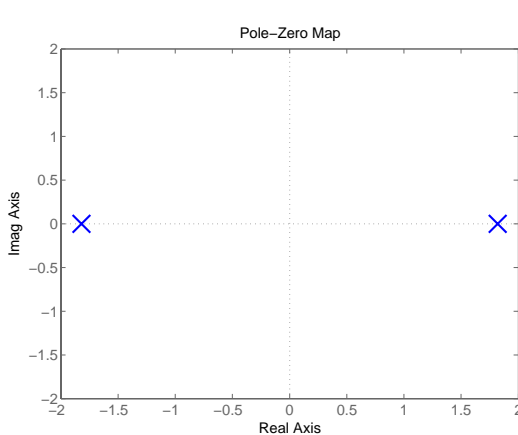


Figure 3.3.12 Unstable pole locations in the complex plane.

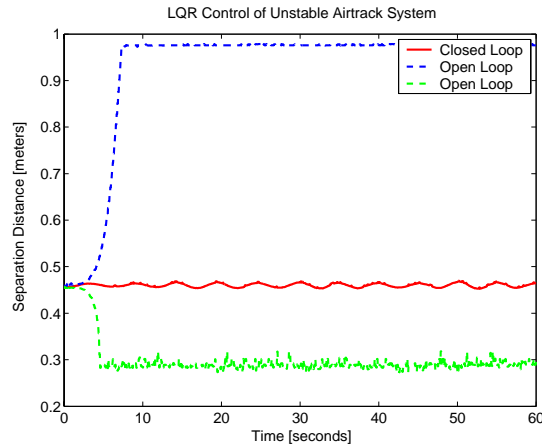


Figure 3.3.13 Open- and closed-loop responses of unstable airtrack.

As for the stable configuration, the dynamic equations of motion and control design for this unstable airtrack configuration are provided in Appendix E, and the results are summarized here.

This unstable system's poles have the same magnitude as the stable airtrack's poles, but the two poles now lie on the *real* axis, instead of the *imaginary* axis. More importantly, we see that **this system's dynamics are nearly identical to those of the satellite cluster spinning at a constant rate**, with poles at $\pm\Omega$, as derived earlier in this section. Since both systems have two real poles, one positive and one negative, mirroring each other in the complex plane, the only difference is the magnitude of the poles. **Thus implementing closed-loop control of this unstable airtrack system should demonstrate the feasibility of controlling a system with similar dynamics, such as a rotating formation flight cluster.**

Again, these results were adapted to the configuration where the free body is a permanent magnet. The resulting open- and closed-loop responses are shown in Figure 3.3.13, where the separation distance between the fixed and free magnets is plotted as a function of time. Recall in the stable airtrack configuration that *step responses* were used to

gauge the control performance; however, in the unstable configuration, the open-loop response is divergent, so rather than considering a step response, we consider the controllers' abilities to *reject disturbances and maintain a constant separation distance*. The closed-loop response performs fairly well; in addition to stabilizing the inherently unstable system, the controller contains the oscillation to within ~2 cm of the steady-state displacement value, yielding even better performance than in the stable configuration. Also shown are two open-loop responses. In one case, the response diverges because the two magnets fall apart; in the other case, the two magnets come together. In both of these cases, the divergent magnet is stopped by barriers placed at the ends of the airtrack (visible in Figure 3.3.6); hence the response becomes constant once the free magnet reaches the barrier.

These unstable airtrack experiments have demonstrated the feasibility of applying similar control for disturbance rejection in an EMFF system undergoing steady-state spin. The experimental results show that unstable dynamics can be successfully stabilized using modern control techniques.

One-Dimensional Spin-Up Dynamics: Phase-Plane Analysis

We now consider a two-spacecraft, two-dimensional array beginning at rest and undergoing a “spin-up” maneuver to reach a steady-state spin rate, as shown in Figure 3.3.14. Initially the two vehicles are positioned at an appropriate separation distance with their magnetic fields perpendicular to each other. The yellow arrows represent electromagnetic forces and torques, while the blue arrows represent reaction wheel torques. If the reaction wheel torques counteract the electromagnetic torques, the forces will cause the spacecraft to shear apart, thereby rotating the array. To design a controller, the system must first be analyzed.

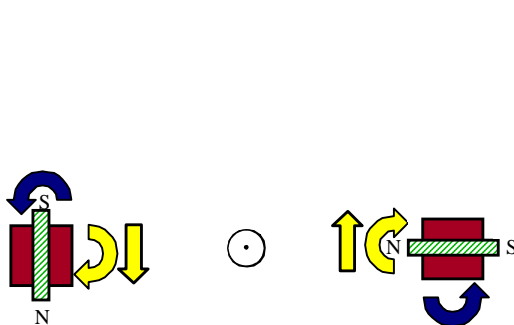


Figure 3.3.14 Two spacecraft with electromagnets undergoing initial spin-up about the system center of mass.

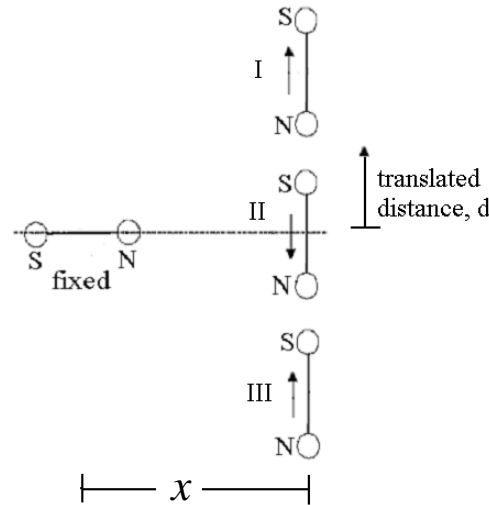


Figure 3.3.15 Translation-dependent shear force on two spacecraft with perpendicular magnetic fields.

When spinning up, the vehicles will experience disturbances. Any number of disturbances can cause one or more vehicles to translate. Therefore it is important to take into account the shear forces between two electromagnets with perpendicular magnetic fields. As shown in Figure 3.3.15, assume that the right-hand magnet is translated in the vertical (shear) direction. This magnet's motion is governed by a shear force that depends on the translated distance. This translation can be broken into three regimes. If the vertical magnet is well above the centerline of the horizontal magnet, it will be repelled. If it is well below, it will be attracted. If it is on the centerline, it will be repelled downward. Notice that these shear forces (indicated by arrows) flip direction twice, indicating the existence of two equilibrium positions. The equilibrium position that lies above the centerline is unstable, while the one below is stable. The triangle formed by the two equilibrium positions and the center of the horizontal magnet is isosceles, so that the equilibrium positions lie ± 45 degrees about the horizontal magnet's centerline. During the spin-up maneuver, the horizontal magnet must be pointed such that its centerline passes through the other magnet. The required pointing

accuracy is a fraction of the angle between equilibrium positions. One tenth of this range should be sufficient, yielding a pointing accuracy of ± 4.5 degrees.

A phase-plane analysis of these equilibria leads to Figure 3.3.16. Translation in the shear direction is plotted versus velocity. The two equilibria are shown on the horizontal axis. The location of the shearing magnet during spin-up corresponds to the origin. Notice that if the horizontal magnet remains fixed in angle, and is not allowed to rotate to track the shearing magnet, the shearing magnet will accumulate sufficient velocity to pass through the stable equilibrium and not return. This further illustrates the complexity of the electromagnetic formation flight control problem.

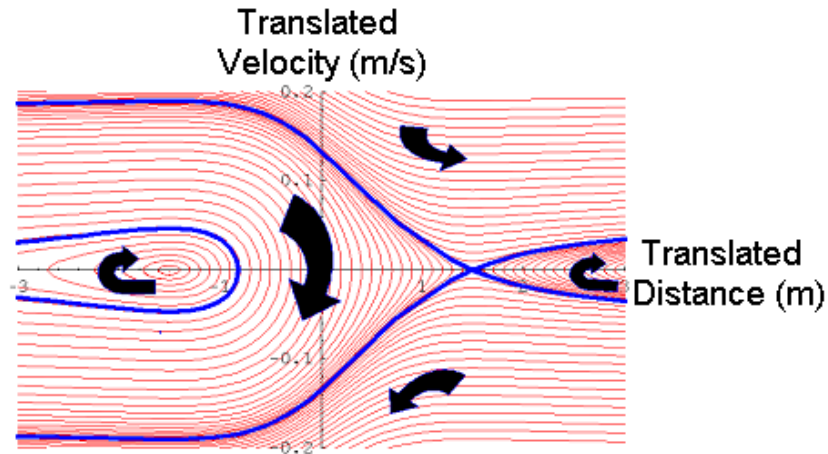


Figure 3.3.16 Phase-plane of the perpendicular magnet geometry.

Three-Dimensional Steady-State Spin Dynamics

The goal of the work summarized in this section is to define the nonlinear equations of motion for a two-spacecraft formation flying array undergoing a steady-state spin maneuver *in three dimensions*. While these equations will capture the nonlinear dynamics of the system being considered, they will be linearized for purposes of control design and stability analysis. Once a controller has been designed for this system using the linearized *design model* of the dynamics, the following nonlinear equations may serve as an *evaluation model* for simulating the closed-loop behavior of the nonlinear system. Note that these equations now include gyrostiffening effects on the spacecraft, caused by the reaction wheels' spinning about axes perpendicular to the array's spin-plane.

System Description

The two-spacecraft array being considered is depicted in Figure 3.3.17. The X, Y, Z coordinate frame represents a global, non-rotating frame whose origin lies at the center of mass of the two-spacecraft array. The first spacecraft, denoted as "spacecraft A," lies at coordinates r, ϕ, ψ . Since the global frame's origin coincides with the array's center of mass, and we are considering the two spacecraft to be identical in mass and geometry, the second spacecraft, denoted as "spacecraft B," lies at coordinates $r, \phi + \pi, -\psi$ (or equivalently $r, \phi, \psi + \pi$).

While the X, Y, Z and r, ϕ, ψ frames represent global frames, the $\hat{e}_r, \hat{e}_\phi, \hat{e}_\psi$ frame represents a local frame whose origin lies at the center of mass of spacecraft A. The $\hat{e}_r, \hat{e}_\phi, \hat{e}_\psi$ frame is not fixed to the body in that it does not rotate or "tilt" with the spacecraft. Notice the \hat{e}_r vector always aligns with the position vector, \hat{r} , of spacecraft A relative to the origin of the global frame. The x, y, z frame, in contrast, rotates with the body relative to the $\hat{e}_r, \hat{e}_\phi, \hat{e}_\psi$ frame; it is also fixed to the center of mass of spacecraft A.

The relative orientations of the two spacecraft are defined using an Euler angle representation. The Euler angles of spacecraft A are α_1, α_2 , and α_3 , which represent sequential rotations about the body-fixed z, y , and x axes, respectively. Similarly, the orientation of spacecraft B is defined by the Euler angles β_1, β_2 , and β_3 , which represent three sequential rotations about a body-fixed frame on B that is nominally aligned with the r, ϕ, ψ frame on spacecraft A.

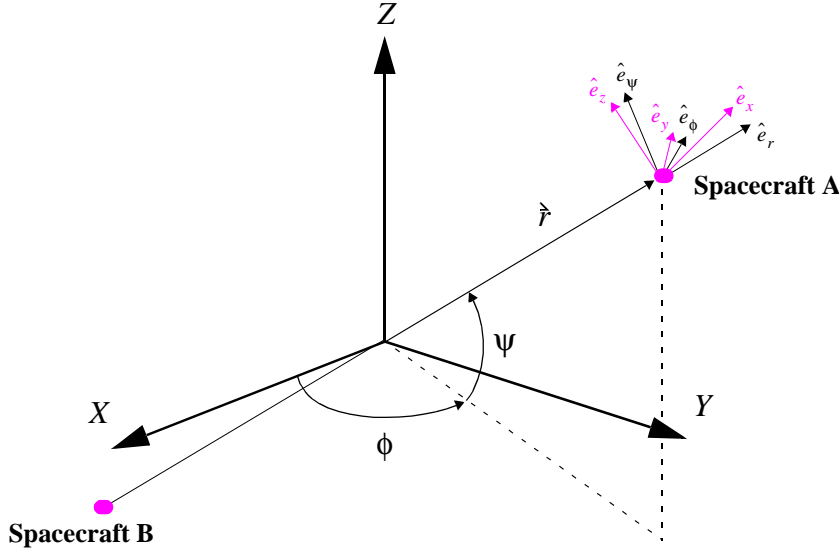


Figure 3.3.17 Geometry of Two-Spacecraft Array

The nominal orientation of each spacecraft is such that the x, y, z frame aligns with the r, ϕ, ψ frame. This work considers perturbations from this nominal orientation; in other words, it considers the dynamics of the x, y, z frame rotating relative to the r, ϕ, ψ frame.

In this analysis, we consider that spacecraft A and B each contain a single electromagnetic dipole oriented along the body-fixed x -axis (and thus aligned with \hat{e}_r when the spacecraft is in its nominal orientation). Finally, we assume that each spacecraft contains a reaction wheel (RW) whose spin axis is aligned with the body-fixed z -axis, and thus is nominally perpendicular to the array's spin-plane. Each RW is spinning at a constant rate, $\Omega_{z,w}$, necessary to conserve the angular momentum of the spinning array. In other words, the sum of the angular momentum stored in the two RWs is equal and opposite to the angular momentum of the two-spacecraft array as it rotates about its own center of mass. Nominally the two spacecraft would assume a circular trajectory in the global X, Y plane ($\psi=0$) with a constant angular velocity, $\dot{\phi} = \dot{\phi}_0$.

Now that this sample configuration has been defined, the dynamic equations of motion are derived and linearized. This derivation, and the resulting complicated set of equations, are presented in Appendix F. We have learned from this derivation the following:

- The resulting system has 18 poles, corresponding to the 18 states of the system.
- Three poles lie on the positive real axis (like the unstable pole of the unstable airtrack configuration, shown in Figure 3.3.12), and three poles mirror these poles on the negative real axis (like the *stable* pole in the unstable airtrack configuration, shown in Figure 3.3.12).
- Six poles lie at the corresponding locations on the positive and negative imaginary axes, respectively. These poles correspond to the poles of the stable airtrack configuration, shown in Figure 3.3.9.
- Six poles lie at the origin, corresponding to six rigid-body modes of the system.

Proposed future steps to extend this work include:

- assessing the controllability this system.
- deriving the corresponding equations of motion for a system with *three orthogonal electromagnets* (EM) and *three orthogonal reaction wheels* (RW) on each spacecraft, and linearizing these equations.
- assessing the controllability of this three-EM, three-RW system.
- designing an optimal controller using the linearized equations for either of these systems determined to be controllable.
- **performing a dynamic time-simulation** using the original nonlinear equations to demonstrate the control of such a complex system.

Satellite Spin Up

As discussed in Section 3.1 satellites using EMFF have the ability to move relative to each other in anyway desired. An interesting maneuver that captures this effect and demonstrates some interesting properties of EMFF is a spin-up maneuver. A spin-up maneuver initially starts with any number of satellites in an arbitrary configuration that is inertially fixed. The cluster, due to the EMFF forces, begins to rotate at a pre-determined rate. Once at the desired rotation rate, the EMFF system provides the correct centripetal forces to hold the formation together.

Two Satellite Spin-Up Dynamics (Analytical Solution)

Initially, a simulation with two spacecraft in a plane is presented. From Equation 3.1.4, the equations for the force and torque are given as

$$\begin{aligned} F_x &= \frac{3}{4\pi} \frac{\mu_0 \mu_A \mu_B}{d^4} (2 \cos \alpha \cos \beta - \sin \alpha \sin \beta) \\ F_y &= -\frac{3}{4\pi} \frac{\mu_0 \mu_A \mu_B}{d^4} (\cos \alpha \sin \beta + \sin \alpha \cos \beta) \\ T_z &= -\frac{1}{4\pi} \frac{\mu_0 \mu_A \mu_B}{d^3} (\cos \alpha \sin \beta + 2 \sin \alpha \cos \beta) \end{aligned} \quad (3.3.1)$$

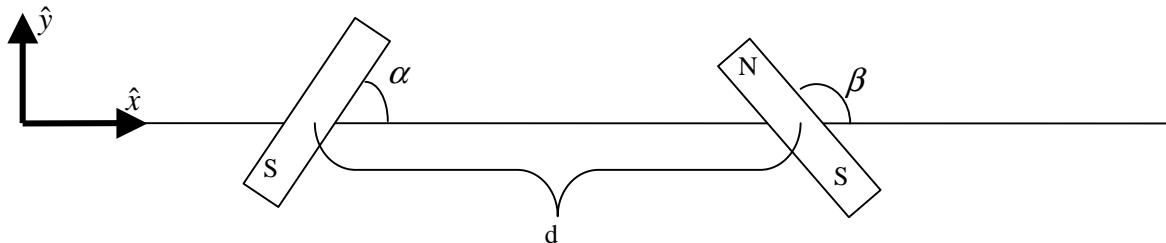


Figure 3.3.18: Schematic of Two Magnetic Dipoles

If we restrict the motion to be planar, there are six degrees of freedom: two translational and one rotational for each satellite. Because the system only has internal forces, the center of mass of the system is fixed. This reduces the translational degrees of freedom from four to two. Each satellite has three control options: magnet strength μ , dipole angle α , and the reaction wheel torque.

The reaction wheel directly controls the rotational position of the spacecraft and counteracts any torques produced by the electromagnetics. It can be assumed that the reaction wheels will always apply the correct amount of torque needed to counteract the torque produced by the electromagnets. For the two satellite case, the magnetic dipole strengths always appear as a multiplicative pair $\mu_A \mu_B$, so there are really three control choices $(\mu_A \mu_B, \alpha, \beta)$.

Because the satellites are to remain a fixed distance from each other, there cannot be any acceleration in the \hat{x} direction. The attraction force between the magnets must always counteract the centripetal acceleration of the satellite.

$$F_x = m a_{centripetal} = m \omega^2 r \quad (3.3.2)$$

The shear force must provide the correct angular acceleration

$$F_y = m \dot{\omega} r \quad F_y = m \dot{\omega} r \quad (3.3.3)$$

For simplicity we can choose one of the variables $\beta = 0$. Solving for α and $\mu_A \mu_B$ results in the following solutions:

$$\mu_A \mu_B = \frac{32\pi m r^5}{3} \frac{\sqrt{4\dot{\omega}^2 + \omega^4}}{\mu_0}$$

$$\alpha = -\cos^{-1}\left(\frac{\omega^2}{\sqrt{4\dot{\omega}^2 + \omega^4}}\right) \quad (3.3.4)$$

From Equation 3.3.4, it can be seen that the magnetic dipole strengths and angle can be calculated for any formation spin rate ω and acceleration $\dot{\omega}$.

An example spin up profile is defined as

$$\dot{\omega}_{Desired} = \begin{cases} 1 - 0.5t & t \leq 2 \\ 0 & t > 2 \end{cases} \quad (3.3.5)$$

Solving for ω as a function of time and substituting the results into Equation 3.1.4, the following spin-up profile was created. The arrows point in the direction of the magnetic dipole (N), and the formation initially starts from rest on the x-axis. The simulation was created by using a numerical integrator to verify the spin-up solution was correct.

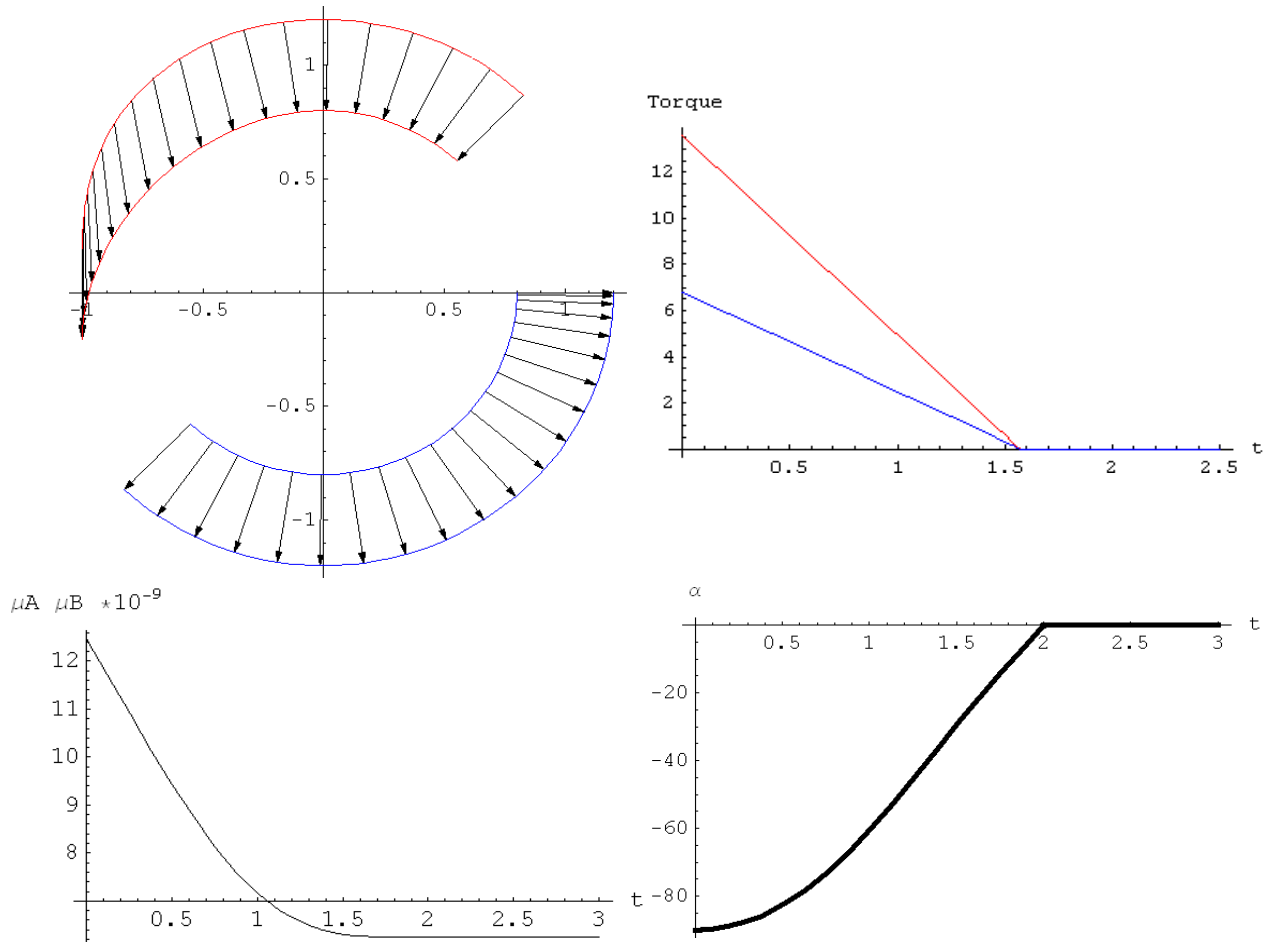


Figure 3.3.19: Results from a Two Satellite Spin-Up Simulation

The bottom left plot of Figure 3.3.19 shows the magnetic dipole strength over time. Notice the non-zero value of the magnetic dipoles. This force is the centripetal force needed to counteract the centrifugal acceleration. The bottom right plot shows the angle of the left dipole. As the centripetal acceleration increases due to the increased spinning of the cluster, the magnet turns more towards the other dipole so that the radial forces increase.

Three Spacecraft Spin-up

Spin-up is not restricted to two spacecraft. This maneuver can be accomplished with any number and orientation of satellites, but before jumping to significantly more complex satellite formations, a formation of three co-linear satellites will first be evaluated. Instead of two equations of motion and three variables, with three satellites we must now solve four non-linear simultaneous equations of motion with six variables. These extra variables allow for an increase in the flexibility of the system as it allows the user to balance magnet dipole strength throughout the maneuver, or change the torque distribution. However, with a system of four non-linear EOM, it becomes increasingly difficult to find analytical solutions except for very specific cases. The EOMs are thus solved numerically at each time step.

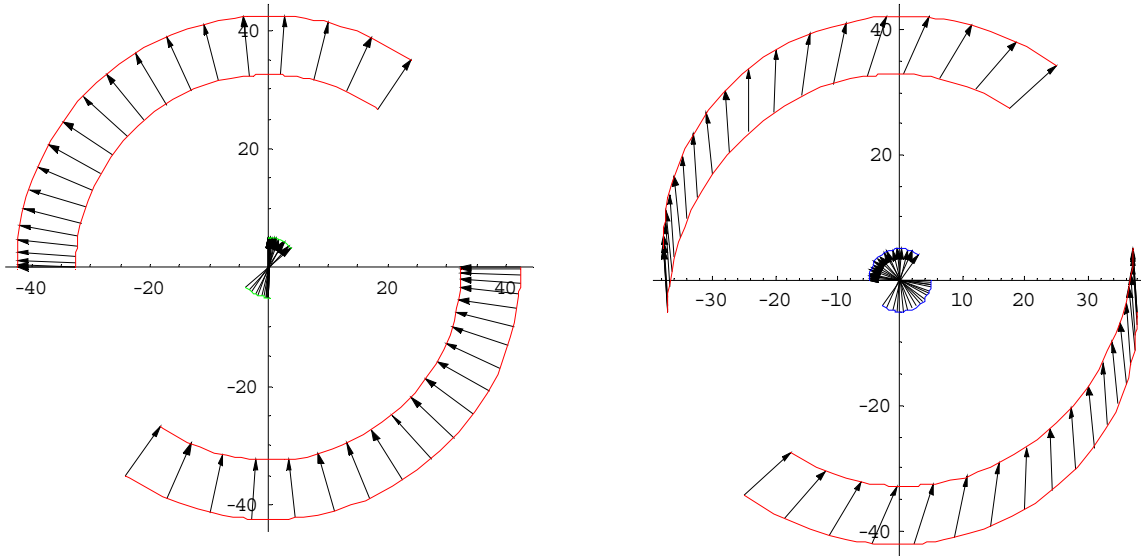


Figure 3.3.20: Results from a Three Satellite Spin-Up Simulation

Figure 3.3.20 shows three satellites initially at rest on the x-axis. The left simulation shows the three dipoles initially in a “— | —” configuration, while the simulation on the right shows the dipoles initially in a “| —” configuration. The two different configurations do not differ in the total system angular momentum (because they have the same angular velocity profile), but they do differ greatly in how the angular momentum is distributed among the satellites. It was shown in section 3.1 that the torque applied to the dipole that is perpendicular to the line between the two satellites has twice the torque applied to it than the other satellite. In the left configuration, the center satellite has twice the torque applied to it from the left satellite than the left satellite receives. It also has twice the torque applied on it from the right satellite than the right satellite receives. The ratio of applied torque is 1:4:1. The outer satellites’ reaction wheels must absorb approximately 16% of the total angular momentum each, while the center satellite must absorb over 68% of the total angular momentum. In the right configuration, the outer satellites each receive twice as much torque as they apply to the center satellite. The ratio of applied torque is now 1:1:1, and each satellite’s reaction wheel absorbs the same amount of angular momentum.

If the satellite formation is made up of identical satellites, the right configuration would be preferable because each satellite would have the same reaction wheel system and all satellites would absorb the same amount of angular momentum. However, if the center satellite was a large combiner spacecraft with a large reaction wheel, and the outer satellites were light-weight collectors, the left configuration would be ideal because most of the angular momentum could be stored in a large reaction wheel on the center satellite (much like the hub and spoke configuration for tethered systems). This would allow the outer spacecraft to have smaller reaction wheels. By

transferring most of the reaction wheel weight into the center of the cluster, the system moment of inertia is reduced, and less magnetic force is needed to spin up the formation.

Five Spacecraft Spin-Up and Other Complex Formations

While the spin-up of two and three satellite formations is fairly straight forward, more complex formations can also be controlled. The Terrestrial Planed Finder (TPF) mission utilizes five co-linear spacecraft. Figure 3.3.21 shows five satellites initially at rest on the x-axis. The dipoles are aligned in a “| - | - |” fashion with each dipole nearly perpendicular to each other. The grey lines do not indicate a physical connection, but an imaginary axis between the satellites at different times during the simulation. While the outer (A) and inner (B) satellites have perpendicular dipoles, the center (C) satellite's dipole is initially offset. The reason for this initial offset is to counteract the attraction force between the two inner satellites which have their axes aligned. With multiple satellite formations, the control becomes more complex because each satellite's magnetic dipole affects every other satellite in the formation to a varying degree. With these complex systems, the increase in the number of non-linear EOMs requires that the solutions be found numerically.

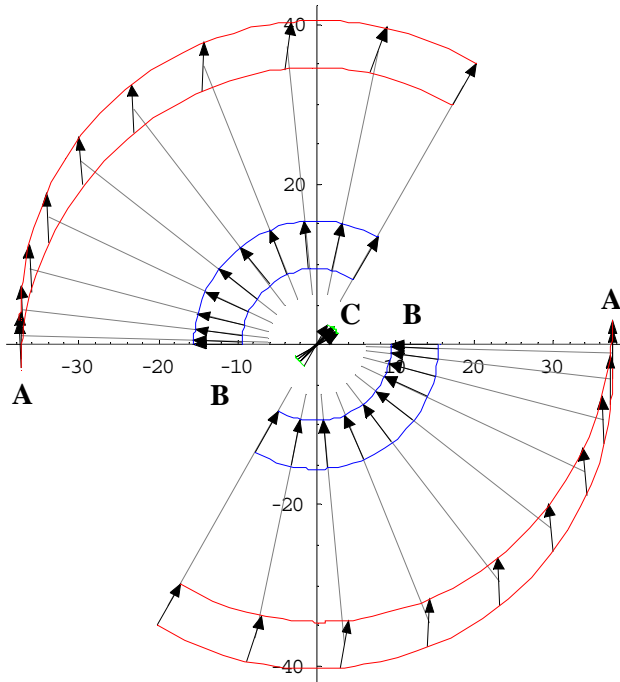


Figure 3.3.21: Five Satellite Spin-Up Maneuver

Just as with the three satellite spin-up problem, there are also multiple solutions to the five satellite spin-up problem. One could easily imagine a dipole order in a “- | - | -“ configuration, and such solutions have been found. Also, solutions where the center or inner satellites produce an outward radial force have been found. In these configurations the outer satellites must counteract this force in addition to the centrifugal acceleration. These solutions, while not optimal in terms of magnet sizing, do allow for different angular momentum distribution and demonstrate the increasing complexity of solutions for multiple satellite systems.

While all of the previous configurations have been exclusively linear systems, this is not a requirement of electromagnetic systems. An equilateral triangle configuration can also be spun-up from rest. See Figure 3.3.22. As the formation spins up, the dipoles once again change their orientation in order to counteract the increasing centrifugal acceleration. In the linear formations, the dipoles always align themselves with the radial vector in the steady state. In the equilateral triangle configuration they end up perpendicular to the radial vector. The final steady state configuration is shown with grey radial lines.

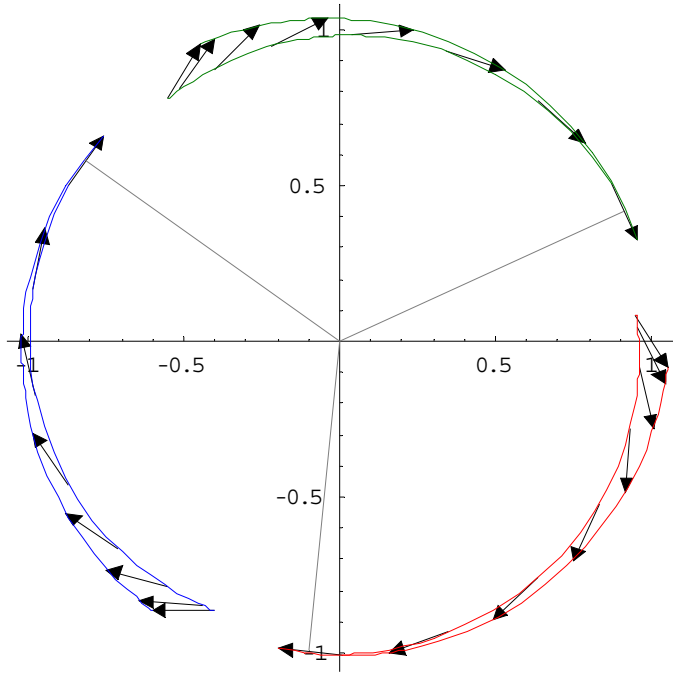


Figure 3.3.22: Equilateral Triangle Configuration

Overall any formation of satellites may be spun-up or down. The ability is not restricted to linear formations of satellites. Also, more complex motions can also be completed. The only difficulty lies in solving the simultaneous non-linear equations.

Angular Momentum Management

Overview

Once again, EMFF has the property that all the forces generated by the electromagnets are internal to the system. Excluding any disturbance interactions with the earth's magnetic field, EMFF cannot apply any external forces to the formation. This prevents EMFF from having the ability to change the inertial position of a formation. It also prevents changes in the total system angular momentum. While reaction wheels are used to temporarily store the angular momentum changes of the formation, they are not able to change the total system angular momentum.

In an ideal situation, this would not be an issue as the angular momentum of the system would remain constant. However, disturbance forces cause unwanted torques on the satellite formation and cause a net gain in the system angular momentum. If left unchecked, the reaction wheels will eventually saturate and become useless. These disturbance torques must be accounted for, and methods for removing this unwanted angular momentum are presented in this section.

Earth's Magnetic Field

One disturbance source that is immediately apparent is the Earth's magnetic field. Whenever any of the EMFF electromagnets are energized, they are affected by the Earth's magnetic field. This disturbance will manifest itself as disturbance forces and torques on the satellite formation. These disturbance forces and torques cause a net gain in the angular momentum of the satellite formation.

In order to characterize this effect, the Earth can be thought of as one large electromagnetic dipole. This is the same simplification technique used in Section 3.1. Equation 3.1.4 shows the forces and torques are all functions of the product of the magnetic dipole strengths. One novel way of canceling the disturbance torques and forces due to the

Earth's magnetic field is to reverse the polarity of every spacecraft dipole at the same time [Hashimoto et al. 2002]. Since the electromagnetic forces are functions of the product of the dipoles, the inter-spacecraft forces are unchanged. However the disturbance forces and torques due to the Earth's dipole have switched sign, thus canceling out the disturbance forces. This polarity switching could be done at a low frequency; the dipoles would switch only when the accumulated angular momentum becomes large, or the switching could also be done at a relatively high frequency, essentially preventing any angular momentum build-up.

Since we have the ability to apply a net torque to the satellite formation in one direction or the other, the Earth's magnetic field could be utilized to remove the overall net angular momentum of the system. If the system were gaining angular momentum due to some other disturbance torque, the Earth's magnetic field could be used to reduce the system angular momentum. Also, since the inter-spacecraft forces are once again products of the magnetic dipole strengths, we can selectively turn up one satellite's dipole strength and reduce the other spacecraft's dipole strength. The inter-satellite forces and torques would remain unchanged, but the magnetic disturbance force would be focused on one specific satellite. Thus individual satellites could be targeted for momentum exchange.

LEO and the J₂ Disturbance

Satellite formations that are in low Earth orbit (LEO) are subject to variations in the Earth's gravitational potential. The largest variation is known as the J₂ gravitational potential constant. The J₂ term refers to the fact that the earth is not round, but has a mass bulge around the equator. This mass bulge has three main effects on the satellite formation: it changes the orbital period of the satellite, it causes the formation to separate in the cross-track direction, and it causes the formation as a whole to rotate about its own angular momentum vector [Schweighart, Sedwick 2002].

One effect of the J₂ geopotential is that it causes a satellite's orbital angular momentum vector to precess about the vector coincident with the North Pole. The rate of this precession is dependent primarily on the satellite inclination and altitude. Except for a couple of specific geometry formations, satellite formations usually have satellites with slightly different inclinations and altitudes and thus different rates of precession of the orbital angular momentum vector. The different rates of precession cause the formation to drift apart, since their orbital planes are not aligned anymore. Internal forces can be used to counteract these differential J₂ forces.

In order to counteract these disturbance forces, shear forces must be used and there is a net gain or loss in the formation angular momentum. The loss or gain of the angular momentum is dependent, not on the direction of the EMFF dipole as with the Earth's magnetic field, but on the geometry of the formation. Certain satellite formation shapes and phasings produce a net gain in the formation angular momentum and other formations produce a net loss. Once again, if this angular momentum gain or loss is left unchecked, the reaction wheels will become saturated as they absorb more and more of the angular momentum.

Because of the ability to select the net gain or loss of the angular momentum vector by simply re-phasing the formation, angular momentum change due to the J₂ disturbances does not prevent EMFF from being a viable option for satellites within LEO. *In fact, the J₂ disturbance, much like the Earth's magnetic field, can be used to add or lose angular momentum from the system that is gained from other sources.* Overall, torque management is key to the success of EMFF. Luckily there are ways to change the system angular moment buildup without the use of thrusters.

4. FUTURE WORK

4.1. Magnetic Interaction

Far field interaction is a good approximation for satellites separated at a significant distance, but it is still an approximation and for satellites that are relatively close together, the far field approximation may not be as accurate as needed. The near field model, while accurate, is too cumbersome to calculate quickly. A model that is easy to calculate, but more accurate than the current near field model needs to be designed.

4.2. System Trades

Optimal EMFF system sizes have been determined for relatively small arrays. The next steps are to determine optimal configurations of larger arrays and design electromagnet systems with superconductors. Optimal mass distributions for larger arrays can be simplified by adding additional layers of spacecraft for a collinear array. Incorporating superconducting coils will change the total spacecraft composition because the solar array mass will not be driven by the resistivity of the coil. Superconducting coils will lead to greater mission efficiencies due to higher currents and lower solar array masses. Additionally, it is possible to design an array where only the large center spacecraft is superconducting and the smaller outer spacecrafts use regular copper electromagnet systems.

4.3. Control Analysis

Dynamics and Control Theory

Preliminary dynamic analyses and *linear* control designs have been implemented for theoretical EMFF systems, and a linear controller was successfully implemented on simplified hardware (a one-dimensional airtrack). Hence we have made significant progress in demonstrating the feasibility of the EMFF concept on *simplified systems*.

We would like to further develop this work by performing the following steps in the future:

- develop dynamic analyses and linear control designs for *more complicated EMFF systems*, including multiple-spacecraft arrays in three dimensions, and geometries on the scale of future space-based missions that could benefit from EMFF technology.
- assess the inherent *controllability* of such systems.
- determine the *optimal electromagnetic actuator configurations* for such systems.
- investigate the possibility of applying *nonlinear and/or distributed control methodologies* to the EMFF concept, and develop novel techniques suitable to an EMFF array.
- validate the *EMFF concept on more representative hardware*, such as a two- or multi-dimensional testbed, thus increasing the current TRL of many of the associated technologies.
- compare several control algorithms on this new hardware in order to assess the type of control necessary and the level of success of the various control algorithms and methodologies.

Torque Management

We have identified that angular momentum management is an important issue for EMFF. The earth's magnetic field, and countering the Earth's J_2 geopotential are both sources of system angular momentum change. It was shown that through some simple maneuvers, the Earth's magnetic field and the J_2 geopotential can actually be exploited to change the system angular momentum. While it was shown that the exploitations of these disturbances are possible, exact maneuvers have not been developed and are a source of future research.

4.4. Critical Technology Development

A significant amount of future experimental research will be conducted in conjunction with a testbed being developed by the PI as a part of a senior design project in the Department of Aeronautics and Astronautics. While this testbed was not a part of the Phase I funding, the final products delivered by the course will be used for

development of the critical EMFF technologies. The course is three semesters, and involves the design and construction of a complex aerospace system, integrated from subsystems and operated in ‘the field’. Past operations have involved formation flying of small ‘spacecraft’ on the KC-135 (SPHERES) and operation of an imaging interferometer at the Haystack Observatory (ARGOS). The SPHERES experiment (using cold gas thrusters) has been developed into a NASA flight program, which will be launched to ISS in the summer of 2003.

The current class project is to construct an EMFF testbed (complete with HTS electromagnets) to evaluate the general feasibility of such a system, as well as to verify near field interaction models and test control algorithms that will be developed. The goal of the class is to build three testbed spacecraft to demonstrate formation flight capabilities such as vehicle slewing, disturbance rejection, steady state spin, and spin-up of a three spacecraft array. Figure 4.4 shows a preliminary CAD model design of the EMFF testbed spacecraft. Two orthogonal coils containing superconducting coils along with a reaction wheel in the center of the coils provide the necessary actuation for the spacecraft. The spacecraft is supported on a frictionless air carriage, as a way of simulating the relevant dynamics in two dimensions. A carriage system of this type has been developed in the lab for earlier experiments. The top of the spacecraft contains the avionics and metrology systems while the power systems are located below the reaction wheel. The in field operations will occur on a large flat floor facility.

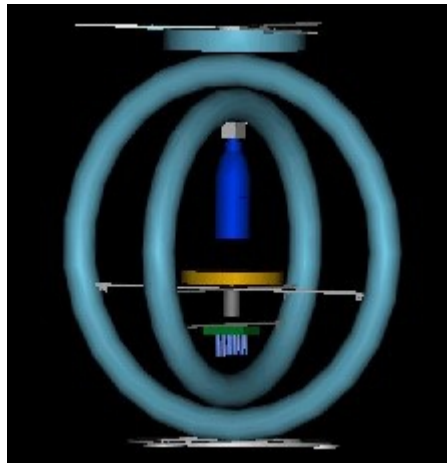


Figure 4.4 CAD model of the EMFF testbed spacecraft

The class began in the spring of 2002, and will have a fully functioning testbed by the end of May 2003. The focus of the class is on the development of the hardware rather than control algorithm development, which will occur at the graduate level. Future work will include development of control algorithms to evaluate the precision with which the system can perform maneuvers and validate the near field models of the dipole-dipole interaction. Successful operation of this testbed to validate these theories in the future will effectively advance major components of this technology to TRL 3-4.

5. REFERENCES

- Beichman, C.A., Woolf, N. J., and Lindensmith, C. A., ed., *The Terrestrial Planet Finder (TPF): A NASA Origins Program to Search for Habitable Planets*, JPL Publication 99-003, 1999.
- Belanger, P.R., *Control Engineering: A Modern Approach*, Saunders College Publishing, 1995.
- Elias, L.M., Kong, E.M., and Miller, D.W., "An Investigation of Electromagnetic Control for Formation Flight Applications," *Proceedings of the SPIE Astronomical Telescopes and Instrumentation Conference*, Waikoloa, HI, August 22-28, 2002.
- Hashimoto, T, Sakai, S, Ninomiya, K, Maeda, K, and Saitoh, T. "Formation Flight Control Using Super-Conducting Magnets," International Symposium on Formation Flying Missions and Technologies, Centre National d'Etudes Spatiales, Toulouse Space Center, France, Oct 29-31, 2002.
- Hughes, P.C., *Spacecraft Attitude Dynamics*, John Wiley and Sons, 1986.
- Kong, E.M.C., *Spacecraft Formation Flight Exploiting Potential Fields*, Ph.D. thesis, Massachusetts Institute of Technology, February 2002.
- Miller, D.W., Sedwick, R.J., Kong, E.M., and Schweighart, S., "Electromagnetic Formation Flight for Sparse Aperture Telescopes," *Proceedings of the 2002 IEEE Aerospace Conference*, Big Sky, MT, March 9-16, 2002, IEEEAC Paper #418.
- Schweighart, S.A. and R.J. Sedwick, "Development and Analysis of a High Fidelity Linearized J2 Model for Satellite Formation Flying", *Journal of Guid. Control and Dynamics*, Vol 25 No. 5, Sept-Oct, 2002.

APPENDIX A. MAGNETIC DIPOLE INTERACTION MODELS (MODEL COMPARISON)

This appendix will derive the near and far field dipole interaction models in detail. The far field model will be compared to the near field model to check its accuracy in both the far and near fields.

A.1 Near Field Model

The near field models for two coils can be created using the following formula:

$$\vec{F}_{AB} = \frac{\mu_0}{4\pi} I_A I_B \iint \frac{d\vec{l}_B \times (d\vec{l}_A \times \vec{r})}{|\vec{r}|^3} \quad (\text{A.1})$$

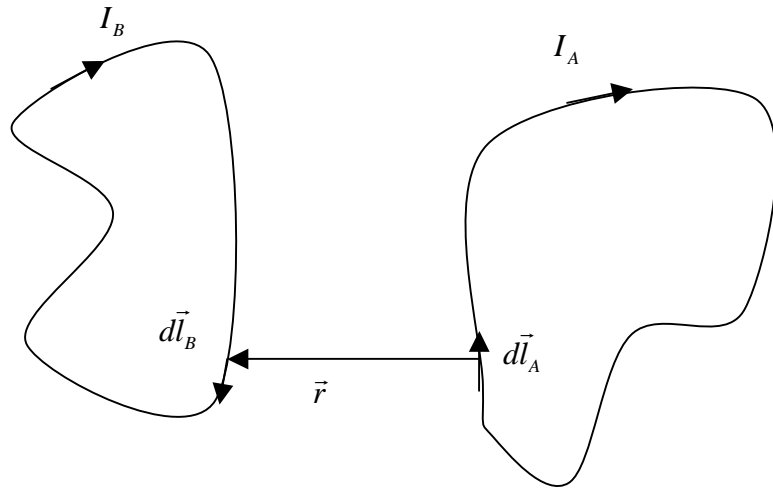


Figure A.1.1: Two Current Loops

The formula can be simplified using circles for the coil loops. However, analytical expressions can only be obtained for special circumstances. Once such circumstance is two circular loops with their axis aligned. The force between these two such loops is:

$$F = \frac{\mu_0 \mu^2}{2\pi r^2} \frac{(\gamma - 2)E(\gamma) - 2(\gamma - 1)K(\gamma)}{(\gamma - 1)} \quad (\text{A.2})$$

$$\gamma = -4 \frac{r^2}{d^2}$$

where K is the elliptical integral of the first kind and E is the complete elliptical integral.

A.2 Far Field Approximation

As stated earlier in Section 3.1, a far field approximation can be made assuming that each electromagnet can be approximated as an electromagnetic dipole. For a current loop the dipole is given as:

$$\bar{\mu} = N i A \hat{n} \quad (\text{A.3})$$

where N is the number of turns, i is the current, and A is the area of the loop, and \hat{n} is the axis of rotation of the loop. The vector expressions for force and torque between two magnetic dipoles will be expressed in a coordinate system and using the parameters defined in Figure A.2.

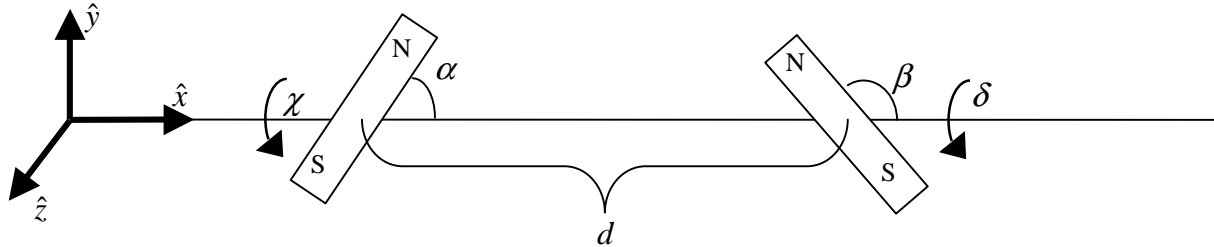


Figure A.2.1: Schematic of Two Magnetic Dipoles

The vector expressions for force and torque on dipole A (left) as a result of the field produced by dipole B (right) are given by:

$$\begin{aligned} \vec{F}_A &= -\nabla U_A = \bar{\mu}_A \cdot \nabla \bar{B}_B = \frac{3\mu_0}{4\pi} \left\{ -\frac{(\bar{\mu}_A \cdot \bar{\mu}_B)}{r^5} \vec{r} - \frac{(\bar{\mu}_A \cdot \vec{r})}{r^5} \bar{\mu}_B - \frac{(\bar{\mu}_B \cdot \vec{r})}{r^5} \bar{\mu}_A + 5 \frac{(\bar{\mu}_A \cdot \vec{r})(\bar{\mu}_B \cdot \vec{r})}{r^7} \vec{r} \right\} \\ \vec{T}_A &= \bar{\mu}_A \times \frac{\mu_0}{4\pi} \left[-\frac{\bar{\mu}_B}{r^3} - 3 \frac{(\bar{\mu}_B \cdot \vec{r})}{r^5} \vec{r} \right] \end{aligned} \quad (\text{A.4})$$

The magnetic dipole moments can be expressed in terms of the parameters defined in figure A.1, and are given as a product of amplitude and direction vector as:

$$\begin{aligned} \bar{\mu}_A &= \mu_A [\cos \alpha \hat{x} + \sin \alpha \cos \chi \hat{y} + \sin \alpha \sin \chi \hat{z}] \\ \bar{\mu}_B &= \mu_B [\cos \beta \hat{x} + \sin \beta \cos \delta \hat{y} + \sin \beta \sin \delta \hat{z}] \end{aligned} \quad (\text{A.5})$$

The position vector \vec{r} was defined from dipole A to dipole B, and in this coordinate system is simply $d \hat{x}$. Making this substitution, as well as the definitions of the magnetic moments into the force equation, and carrying out the dot products results in:

$$\vec{F}_A = -\frac{3\mu_0 \bar{\mu}_A \bar{\mu}_B}{4\pi d^4} \left\{ c\beta \begin{bmatrix} c\alpha \\ s\alpha c\chi \\ s\alpha s\chi \end{bmatrix} + c\alpha \begin{bmatrix} c\beta \\ s\beta c\delta \\ s\beta s\delta \end{bmatrix} + \begin{bmatrix} c\alpha c\beta + s\alpha s\beta c\chi c\delta + s\alpha s\beta s\chi s\delta \\ 0 \\ 0 \end{bmatrix} - 5 \begin{bmatrix} c\alpha c\beta \\ 0 \\ 0 \end{bmatrix} \right\} \quad (\text{A.6})$$

which can be simplified and reduced using trigonometric identities to produce:

$$\vec{F}_A = -\frac{3\mu_0\vec{\mu}_A\vec{\mu}_B}{4\pi d^4} \begin{bmatrix} \sin \alpha \sin \beta \cos(\delta - \chi) - 2 \cos \alpha \cos \beta \\ \cos \alpha \sin \beta \cos \delta + \sin \alpha \cos \beta \cos \chi \\ \cos \alpha \sin \beta \sin \delta + \sin \alpha \cos \beta \sin \chi \end{bmatrix} \quad (\text{A.7})$$

Likewise, the torque can be written as:

$$\vec{T}_A = \frac{\mu_0}{4\pi d^3} [-\vec{\mu}_A \times \vec{\mu}_B + 3(\vec{\mu}_B \cdot \vec{r})(\vec{\mu}_A \times \vec{r})] \quad (\text{A.8})$$

with the cross products given as:

$$\vec{\mu}_A \times \vec{\mu}_B = \mu_A \mu_B \begin{bmatrix} \hat{i} & \hat{j} & \hat{k} \\ c\alpha & s\alpha c\chi & s\alpha s\chi \\ c\beta & s\beta c\delta & s\beta s\delta \end{bmatrix} = \mu_A \mu_B \begin{bmatrix} s\alpha s\beta c\chi s\delta - s\alpha s\beta s\chi c\delta \\ s\alpha c\beta s\chi - c\alpha s\beta s\delta \\ c\alpha s\beta c\delta - s\alpha c\beta c\chi \end{bmatrix} \quad (\text{A.9})$$

and:

$$\vec{\mu}_A \times \hat{x} = \mu_A \begin{bmatrix} \hat{i} & \hat{j} & \hat{k} \\ c\alpha & s\alpha c\chi & s\alpha s\chi \\ 1 & 0 & 0 \end{bmatrix} = \mu_A \begin{bmatrix} 0 \\ s\alpha s\chi \\ -s\alpha c\chi \end{bmatrix} \quad (\text{A.10})$$

Substituting into the equation for torque, and again using trigonometric substitution, the final expression is:

$$\vec{T}_A = \frac{\mu_0 \mu_A \mu_B}{4\pi d^3} \begin{bmatrix} \sin \alpha \sin \beta \sin(\chi - \delta) \\ \cos \alpha \sin \beta \sin \delta + 2 \sin \alpha \cos \beta \sin \chi \\ -\cos \alpha \sin \beta \cos \delta - 2 \sin \alpha \cos \beta \cos \chi \end{bmatrix} \quad (\text{A.11})$$

The same results, not shown here, can also be obtained by using the duality principle between electrostatic dipoles and electromagnetic dipoles. After linearization, the resulting equations are exactly the same.

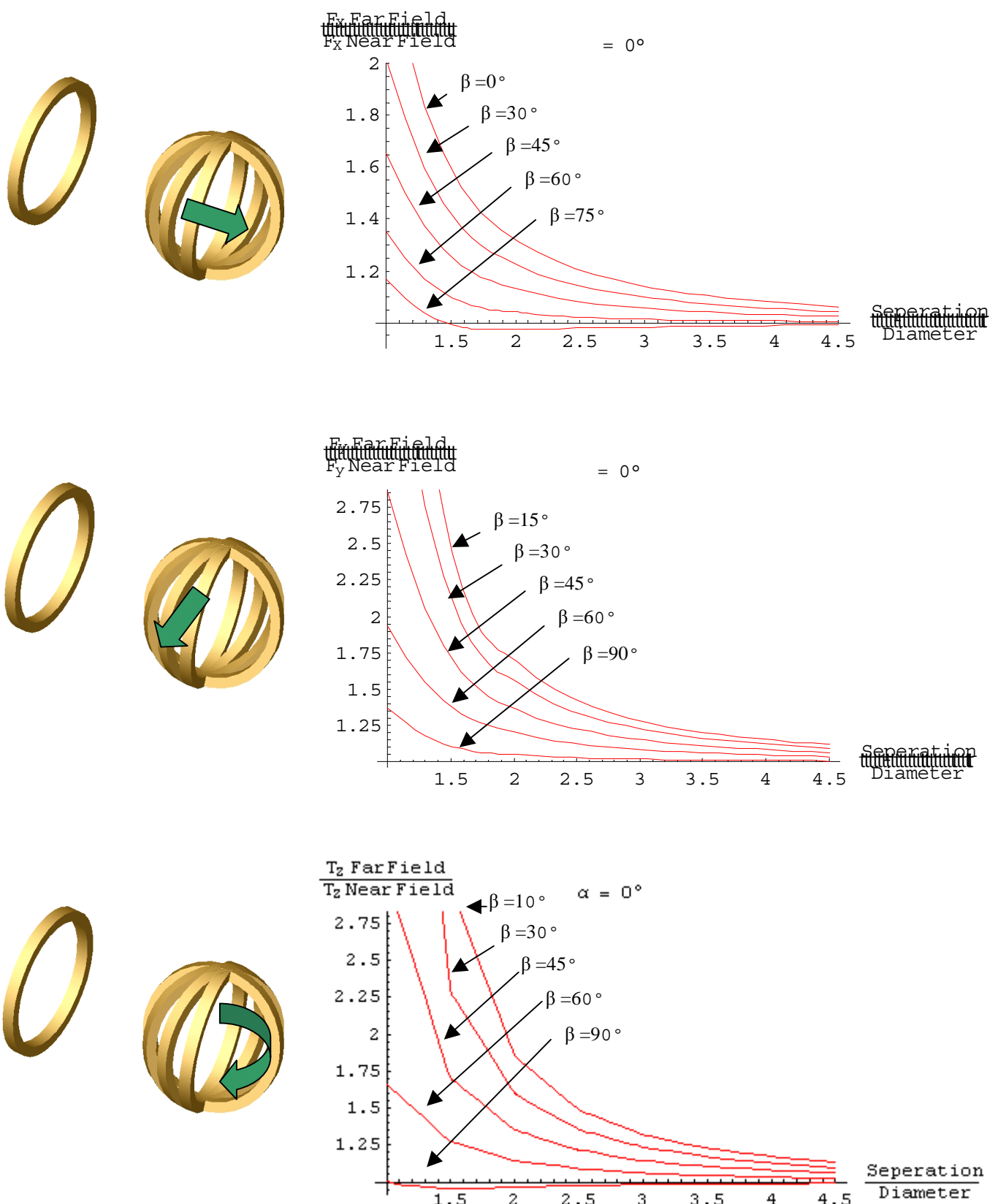
A.3 Comparison between Near Field Model and Far Field Model

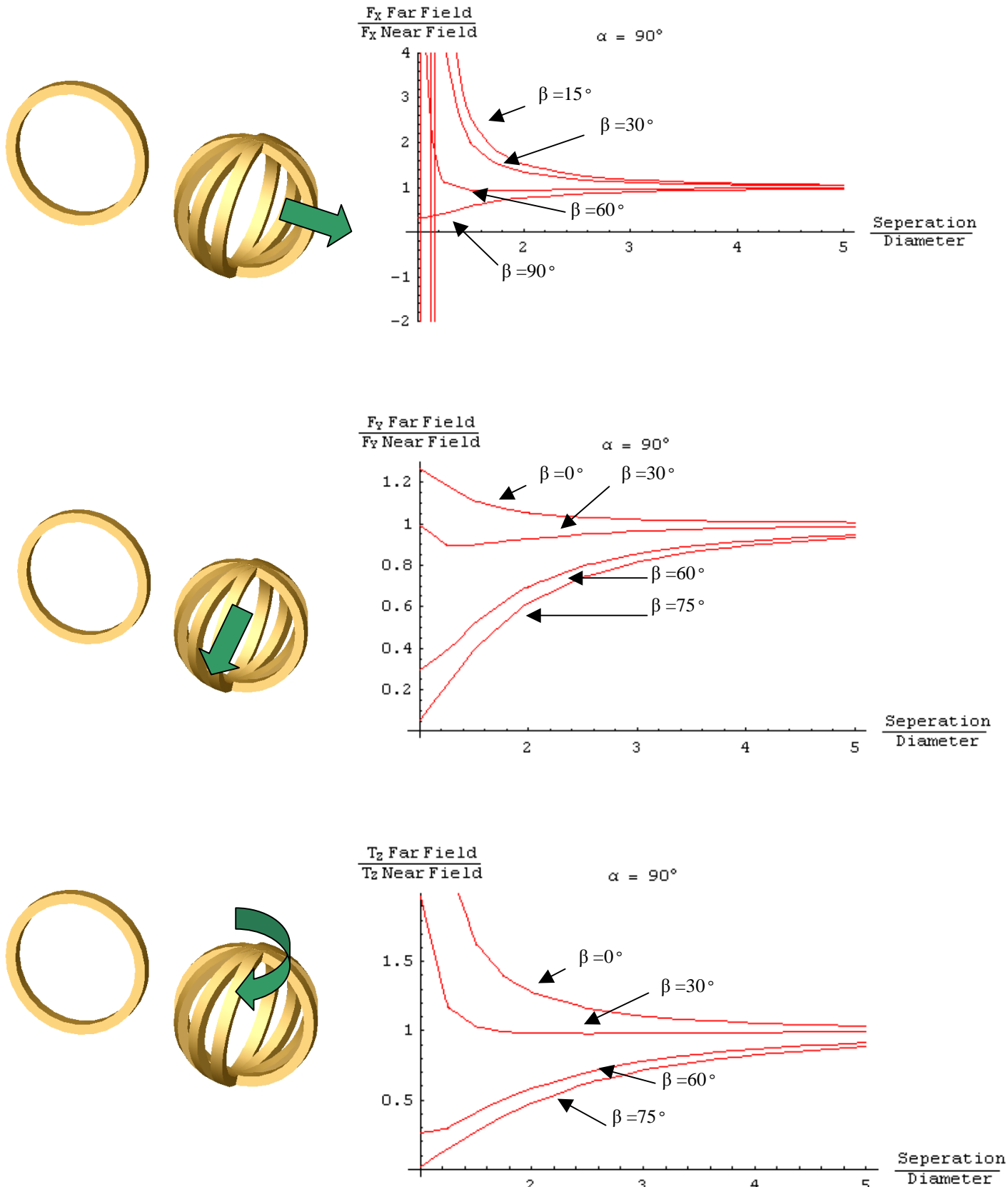
This section will compare the near field model and the far field model described above. The far field equations are much more desirable to use than the near field equation. The far field solutions are analytical expressions in terms of sines and cosines, which makes them easily and quickly solvable. The exact model requires a double numerical integration in all but a handful of specific cases and is time consuming to integrate. For real-time control loops, it would be desirable to use the far field equations for their speed of computation. Also the far field model allows for an intuitive grasp of the dipole-dipole interaction. This section will validate the far field model and show the distance at which the far field model correctly describes the dipole-dipole forces.

Figures A.3.1 and A.3.2 each contain three plots. The top plot compares the axial forces, the middle compares the shear forces, and the bottom compares the torques between the near and far field models. In each plot the distance between the two dipoles is varied and the ratio of far and near field solutions is plotted. The angle of the left dipole, α , is held constant while the angle of the second dipole, β , is varied, and plots of different angles are shown. As can be seen from the plots, the ratio of solutions from the far field and near field always goes towards unity as r is increased. This signifies that the far field solutions are valid for any dipole orientation *in the far field*. When the

satellites are close together, the far field solution diverges from the near field solution. Sometimes the far field solution predicts a higher value than the near field, and sometimes it predicts a lower value, depending on dipole orientation and radius. This prevents a simple near field approximation.

In summary, the far field approximation proves valid, as the name implies, in the far field, but quickly loses accuracy in the near field.

Figure A.3.1: Verification of Far Field Model $\alpha = 0^\circ$

Figure A.3.2: Verification of Far Field Model $\alpha = 90^\circ$

APPENDIX B. SYSTEM TRADES

B.1 Motivation

Proposed EMFF missions such as TPF and Planet Imager consist of an array of multiple spacecraft. As arrays become populated with an increased number of spacecraft and array complexity increases, there exist cost and science productivity benefits in determining an optimal distribution of satellites. The main concern for EMFF is determining the optimal distribution of the electromagnetic mass, which consists of the electromagnetic coil mass and solar array mass.

B.2 Mission Efficiency

The first concern in EMFF system sizing is to determine the benefits of increasing the number of spacecraft in an array. For EMFF missions that require array rotation to conduct scientific observations, the mission efficiency can be defined as the science productivity divided by the cost.

$$J = \frac{w}{c_o m_{array}} \quad (\text{B.2.1})$$

The science productivity is directly related to the array rotation because the faster the rotation, the more images produced in a given amount of time. This is a very general relationship since it assumes photon starvation does not occur. Additionally, the mass of the array is proportional to cost. To simplify J, a scaling term c_o is included. Therefore, increasing the mission efficiency can be accomplished by increasing the rotation rate while minimizing the system mass.

Two identical spacecraft separated by a baseline, B, is used to determine a base case for mission efficiency. Their rotation rate can be found by equating the electromagnetic force to the centripetal force and solving for ω as seen Equation B.2.2 and Equation B.2.3, where n is the number of coil turns, i is the current, and a is the coil radius.

$$\begin{aligned} F &= \frac{3}{2} \mu_o \pi \frac{n^2 i^2 a^4}{B^4} = \frac{1}{2} m_{tot} \omega^2 B \\ \omega &= \sqrt{\frac{3\mu_o \pi}{B^5}} \frac{nia^2}{\sqrt{m_{tot}}} \end{aligned} \quad (\text{B.2.2})$$

c_o is defined so that J becomes a function of the electromagnet properties. For two spacecraft, J_2 is found to be

$$\begin{aligned} m_{array} &= 2m_{tot} \\ c_o &= \sqrt{\frac{3\mu_o \pi}{B^5}} \\ J_2 &= \frac{nia^2}{2m_{tot}^{3/2}} \end{aligned} \quad (\text{B.2.3})$$

where the total array mass, m_{array} consists of two identical spacecrafts.

This same procedure can be repeated for three spacecraft, however with increased complexity. Assuming the array rotates around the center spacecraft, there are two layers of design, the inner and outer spacecraft layers designated

by subscripts. Determining how to design these layers will be discussed later, for simplicity, assume identical spacecraft masses. The force and magnetic interactions for three spacecraft can be defined as

$$F = \frac{3}{2} \mu_o \pi a^4 \left(\frac{n_i i_i n_o i_o}{\left(\frac{B}{2}\right)^4} + \frac{n_o^2 i_o^2}{B^4} \right) = \frac{1}{2} m_{tot} \omega^2 B \quad (\text{B.2.4})$$

$$m_{array} = 2m_{tot_{outer}} + m_{tot_{inner}}$$

The mission efficiency for three identical spacecraft, J_3 , is found to be

$$J_3 = \frac{\sqrt{17}}{3} \frac{n i a^2}{m_{tot}^{3/2}} \quad (\text{B.2.5})$$

The gain of adding a third spacecraft into the array can be found by taking the ratio of mission efficiencies.

$$\frac{J_3}{J_2} = 2.75 \quad (\text{B.2.6})$$

The mission efficiency almost triples by adding a third spacecraft into the array. The added center spacecraft does not need to add scientific functionality in order to increase the amount of science collected. The outer spacecraft will receive 16 times the electromagnetic force from the center spacecraft allowing the array to rotate much faster. Since the array rotates about the center spacecraft, the center vehicle does not need to translate. It can still provide the necessary magnetic forces to the outer spacecraft by steering its dipole. Since the center spacecraft does not need to translate relative to the outer spacecrafcts, there is no mass penalty on it. This leads to the next trade on mass distribution of the array.

B.3 Mass Distribution Trade

Given a restriction on the total mass of an array, either by mission costs or launch restrictions, it is possible to design for maximum mission efficiency. This trade will investigate how the electromagnetic masses for a three spacecraft array can be distributed for maximum science productivity, or rotation rate. The rotation rate for one of the outer spacecraft can be determined by solving the force equation for acceleration in Equation B.2.7.

$$a = \frac{3}{2} \mu_o \pi \frac{a^4}{m_{total} B^4} (16n_i i_i n_o i_o + n_o^2 i_o^2) \quad (\text{B.3.1})$$

A three spacecraft array rotating around the center spacecraft consists of two “layers”. The inner layer is the mass of the center spacecraft while the outer layer consists of the masses of the two outer spacecraft. The outer spacecraft are identical for array symmetry. From these two layers, a mass fraction, γ , is used to determine the distribution of the total array mass.

$$M_{inner} = \gamma M_{total_array} \quad (\text{B.3.2})$$

$$M_{outer} = \left(\frac{\gamma - 1}{2} \right) M_{total_array}$$

γ ranges from zero to one, with zero γ indicating an array with only two outer spacecraft, and γ equaling one indicating a large single spacecraft. The mass of a spacecraft is defined as follows

$$m_{total} = m_o + M_{em} = m_o + m_{sa} + m_{coil} \quad (\text{B.3.3})$$

where m_o is the dry mass of the spacecraft and M_{em} is the electromagnet system, which consists of an electromagnetic coil and solar array. The mass of the coil is defined in terms of the conductor radius, r , number of coil turns, n , coil radius, a , current density, c_o , and coil density, ρ_c .

$$m_{coil} = l_c A_c \rho_c = (2\pi a n)(\pi r^2) \rho_c = 2nia \frac{\rho_c}{c_o} \quad (\text{B.3.4})$$

The mass of the solar array is defined as

$$m_{sa} = \frac{P}{P_w} = \frac{i^2 R}{P_w} = \frac{i^2}{P_w} \frac{p_c l_c}{A_c} = \frac{i^2}{P_w} p_c \frac{2\pi a n}{\pi r^2} = 2\pi nia \frac{p_c c_o}{P_w} \quad (\text{B.3.5})$$

where p_c is the resistivity and P_w is the specific power of the solar array. The total spacecraft mass can be simplified as

$$m_{total} = m_o + 2\pi nia \beta \quad (\text{B.3.6})$$

where

$$\beta = \frac{\rho_c}{c_o} + \frac{p_c c_o}{P_w} \quad (\text{B.3.7})$$

From Equations B.3.4 and B.3.7, the number of amp-turn, ni , for the inner and outer spacecrafts can be determined as a function of γ and substituted into the acceleration for the array (B.3.1). The array rotation now becomes a function of the array mass distribution γ and an optimal γ can be determined. Recall that since the center spacecraft does not translate, the optimal should yield an array with γ greater than one third.

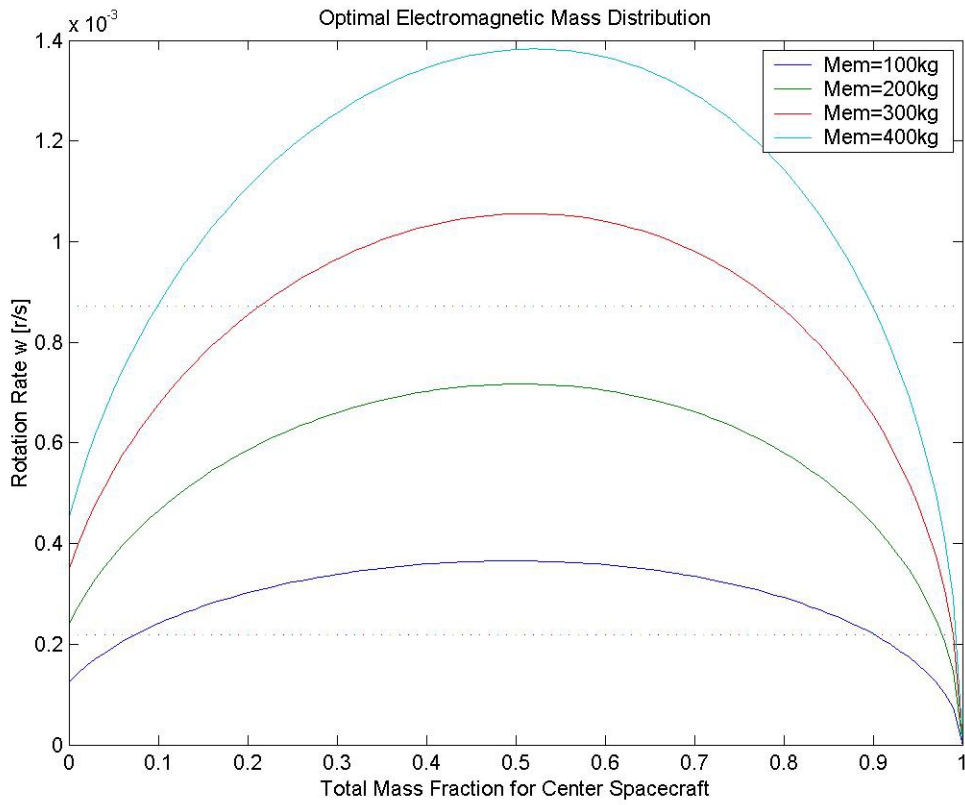


Figure B.3.1: Mass Distribution of a Three Spacecraft Array

Figure B.3.1 shows the array rotation rate as a function of γ for different electromagnetic masses. Equation B.3.9 indicates the mass distribution of the array with a 400 kg EMFF system

$$\frac{M_{inner}}{M_{total_array}} = 0.53 \quad (\text{B.3.8})$$

The center spacecraft consists of almost half the total array mass validating the earlier prediction that the center spacecraft will be larger than an outer spacecraft. Figure B.3.1 also shows the boundary conditions, two identical spacecraft ($\gamma=0$) rotating at a slow rate and a single large spacecraft ($\gamma=1$) with no array rotation. An interesting comparison can be conducted between the three identical spacecraft ($\gamma=0.33$) and three optimally distributed spacecraft. Figure B.3.2 shows the rotation rate ratio between an identical array to an optimally distributed array for varying electromagnetic masses. There is always a gain in rotation rate by designing an array with a larger center spacecraft at optimal γ and this gain increases as the total array mass increases. Therefore it becomes more important for very large arrays to be designed with an optimal distribution in mind.

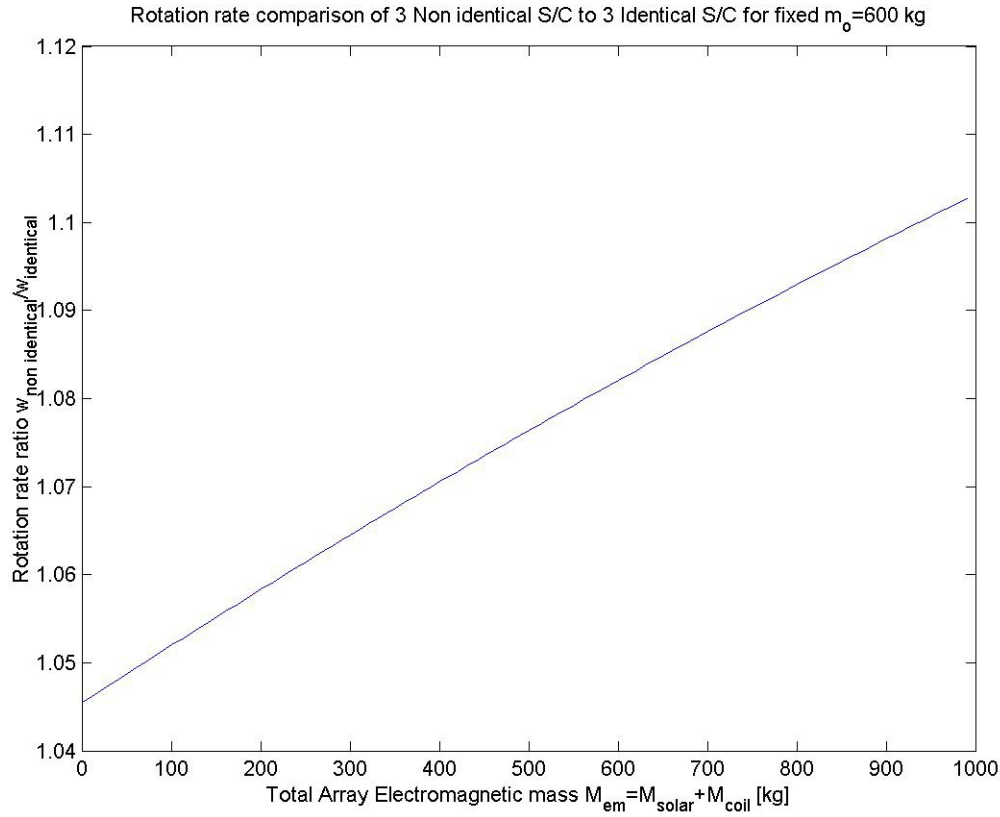


Figure B.3.2: Rotation rate comparison for an identical and optimally distributed three spacecraft array

Figure B.3.3 shows the optimal distribution, γ , as a function of electromagnetic system mass at the maximum rotation rate. The mass of the center spacecraft is approximately half the total array for small and medium sized arrays, however it increases as the array increases.

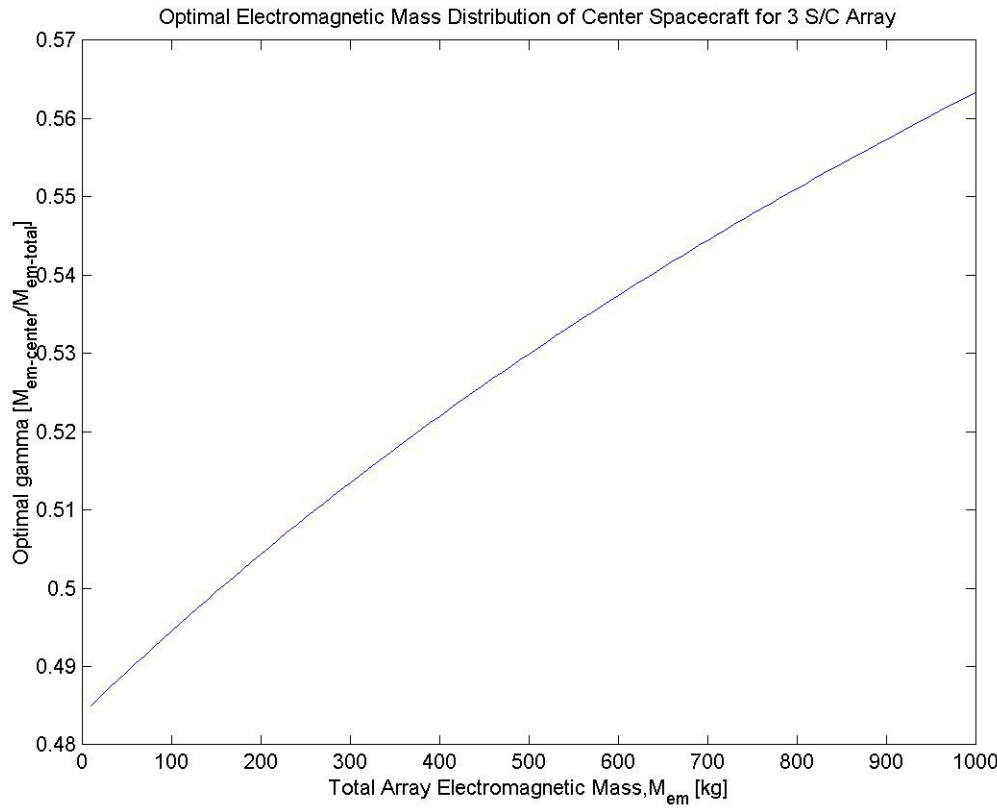


Figure B.3: Optimal mass distribution for varying electromagnetic system masses.

The following analysis was conducted using the present characteristics for a three spacecraft TPF mission at a 25m baseline. Room temperature copper coils were used along with a spacecraft dry mass of 600 kg and spacecraft size of 2 m. The coils are assumed to wrap around the outside of the spacecraft and have similar radius to the current spacecraft radius. The current mass of the TPF propulsion system, 400 kg, was replaced by an electromagnet system of same mass. The two dotted lines in Figure B.3.1 indicate rotation rates of 1 revolution every 2 hours, the goal of TPF, and 1 revolution every 8 hours, the current state of TPF. Clearly retrofitting TPF with an EMFF system has the ability to achieve the goal rotation rate, but also reduce the propulsion system mass by approximately 150 kg. Additionally, by optimally distributing the there is a rotation rate gain which can be determined from Figure 2. By rotating at a higher rate and reducing system mass, an EMFF design can enabled TPF and future space interferometers to increase science productivity and cut costs.

B.4 Generalized Mission Efficiency

Coil vs. Core

The previous section used TPF as a baseline for design optimal system sizes. In order to design a more general EMFF system, the effects of changing the various EMFF system parameters, mainly current and number of coil turns, can be determined. Before optimizing the system size for EMFF spacecraft, determining the effect of magnetizable cores is the first design step. Spacecrafts can be designed with either electromagnetic coils only, or coils wrapped around paramagnetic or ferromagnetic cores. Magnetizable cores can directly improve the electromagnetic attractive force; however, EMFF with cores must account for the additional core mass.

To conduct the following trade analysis, the system masses of a coil-only system and a coil-with-core system are constrained to be equal. The normalized force and acceleration between two axially aligned magnets are then determined. The normalized force has direct impact on a mission baseline, while the acceleration determines spacecraft agility. These aspects of EMFF spacecraft will also be explored later. To model the coil-with-core configuration, the iron core system mass increased with increasing core dimensions while the copper wire length and thickness were held constant. This is a necessary constraint since the wires in a coil have current density and temperature limitations. For the coil-only system, mass was increased with the number of wire turns. Wire length of the coil was increased to keep the system mass equal to that of the core system.

Figures B.4.1 and B.4.2 compare the coil-with-core and the coil-only systems. The trade models two axis-aligned electromagnets and calculates the normalized axial forces and accelerations as a function of core radius, and hence system mass.

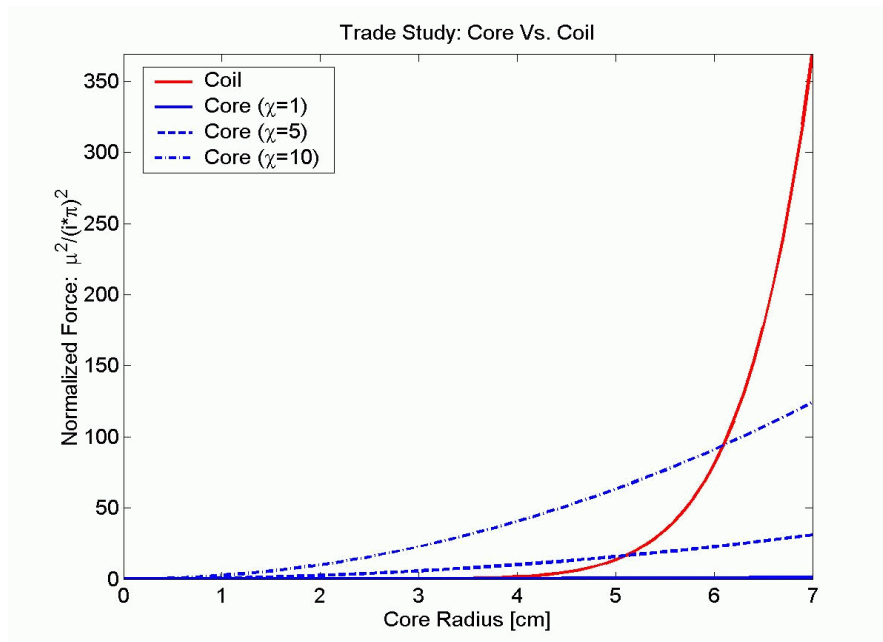


Figure B.4.1: Normalized Forces for Core and Coil Systems

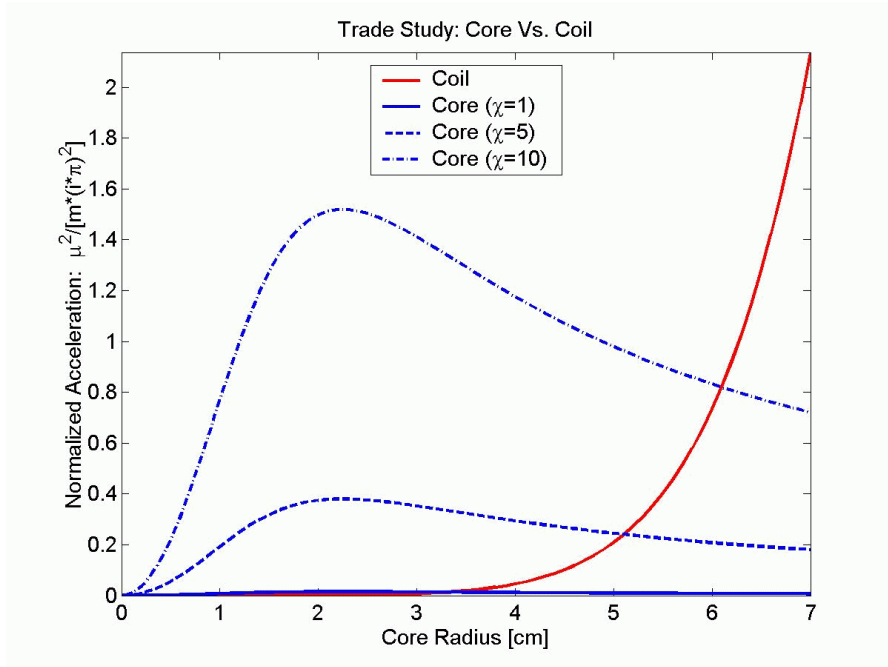


Figure B.4.1: Normalized Accelerations for Core and Coil Systems

There are two useful results from this trade study. For systems with small core or coil radius, mainly testbed-sized vehicles, a core with relatively modest magnetic amplification factor, χ , will greatly improve the system baseline and agility. However, flight-sized EMFF systems will be much larger and will require larger coil and core radii. For these systems, a coil-only configuration is more beneficial, since the normalized force and acceleration for the coil-only system increase dramatically with increasing radius.

Three-Spacecraft Sizing

Now that spacecrafsts have been selected with coils only, we can determine the optimal distribution of EMFF system sizes according to mission efficiency, J , defined in Equation B.2.1. The model considered consists of three collinear EMFF spacecraft: one center vehicle and two vehicles rotating about the center one. With three spacecraft, the constraint of identical spacecraft masses has been dropped because it will not yield the highest mission efficiency. The number of amp-turns in the inner and outer spacecrafsts can be traded to determine the mission efficiency, J . The number of amps or coil turns in the system can be set from the amp-turn product. J can be determined by solving Equation B.2.7 for non-identical spacecrafsts.

$$J = \frac{a\sqrt{16n_i i_i n_o i_o + n_o^2 i_o^2}}{(2m_o + m_i)m_o^{1/2}} \quad (\text{B.4.1})$$

The results of the trade are illustrated in Figure B.4.3. As a baseline mission efficiency, J_R , three identical spacecrafst with 2000 coil turns and 13 A was used for room temperature copper coils. The optimal mission efficiency was then determined along with the designs for the amp-turns and system masses. The gain in mission efficiency was determined as

$$\frac{J_{\max}}{J_R} = 1.24 \quad (\text{B.4.2})$$

The optimal system yields a 25% gain in mission efficiency however, it creates a very massive center spacecraft. The total electromagnetic array mass determined was 4,740 kg with $\gamma=0.68$, yielding small outer spacecraft of 761 kg and a large center spacecraft of 3218 kg. Although the large center spacecraft seems unreasonable, this EMFF system was designed using room temperature copper coils. Implementing superconducting coils will dramatically decrease the mass of the electromagnet system since a superconducting system will require significantly less coil turns and less coil mass.

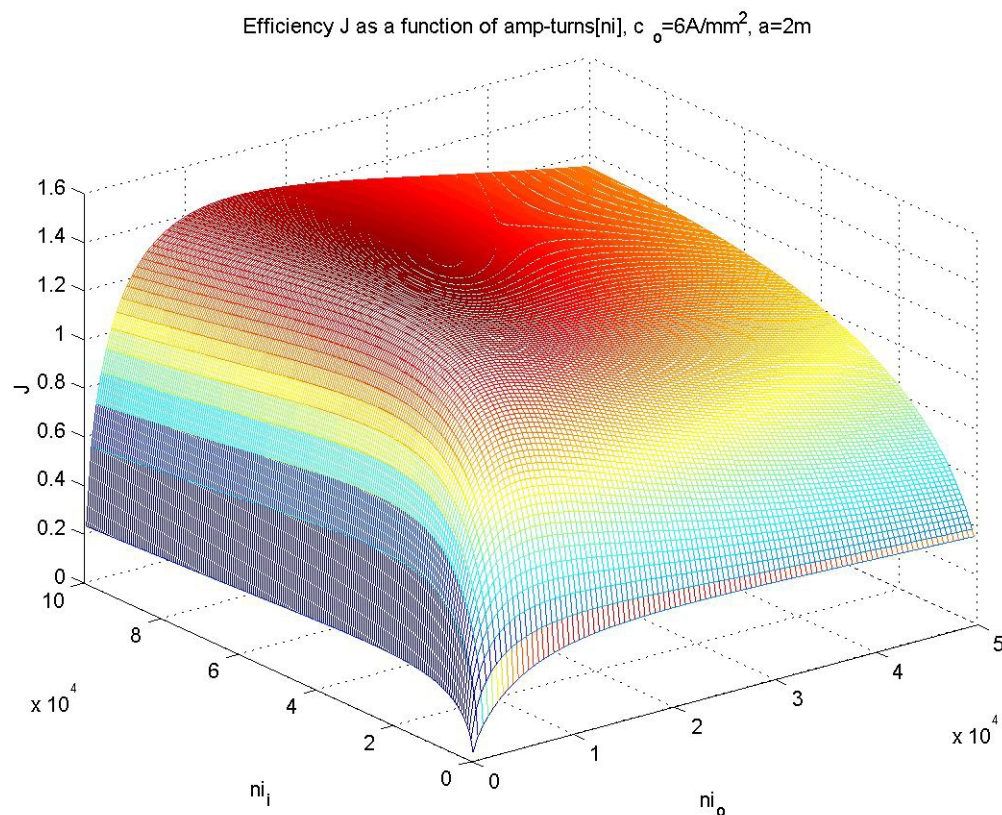


Figure B.4.3: Mission efficiency as a function of amp-turns

Future System Sizing Work

The next steps in EMFF system sizing are to determine optimal configurations of larger arrays and design electromagnet systems with superconductors. Optimal mass distributions for larger arrays can be simplified by adding additional layers of spacecraft for a collinear array. Incorporating superconducting coils will change the total spacecraft composition because the solar array mass will not be driven by the resistivity of the coil. Superconducting coils will lead to greater mission efficiencies due to higher currents and lower solar array masses. Additionally, it is possible to design an array where only the large center spacecraft is superconducting and the smaller outer spacecrafts use regular copper electromagnet systems.

APPENDIX C. SMALL PERTURBATION CONTROL THEORY

In this appendix, the requirements to reject small perturbations using only the proposed EMFF concept are determined in detail. A general kinematic formulation for a multi-spacecraft multipole system is first presented, based on an electrostatic analogy. From these kinematic relationships, a state-space representation of the system is determined, specifically the dynamic (**A**) and control (**B**) matrices. Using these matrices, the controllability of the system is determined to ensure that the system can adequately reject disturbances in all the required degrees of freedom.

C.1 Multi-spacecraft Multipole Electromagnets

The general multi-spacecraft multipole system is shown in Figure C.1.1. In this formulation, a system of M spacecraft, each with N magnetic poles, is considered. The force interaction between two poles is given by:

$$\overrightarrow{F}_{ab,mn} = \frac{kq_{mn}q_{ab}}{\left|\overrightarrow{r}_{ab,mn}\right|^3} \overrightarrow{r}_{ab,mn}, \quad (\text{C.1.1})$$

where k is a constant, $\overrightarrow{r}_{ab,mn}$ is the position vector between poles q_{mn} and q_{ab} , and the product of the two “charges” indicates whether the force between the poles is attractive or repulsive.

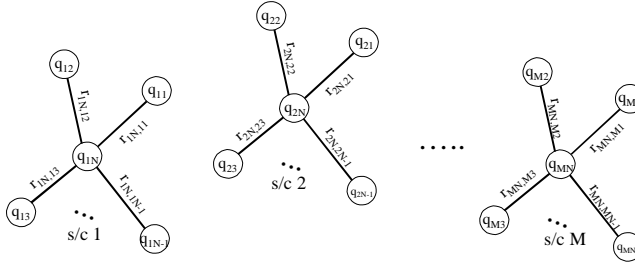


Figure C.1.1: Multi-spacecraft multipole electromagnets.

The total force acting on spacecraft m , due to all the poles on all the other spacecraft, is given by:

$$\overrightarrow{F}_m = \sum_{n=1}^{N} \sum_{a=1}^M \sum_{\substack{b=1 \\ a \neq m}}^N \overrightarrow{F}_{ab,mn}. \quad (\text{C.1.2})$$

Since these poles are generally not located at the centroid of the spacecraft, each spacecraft will inherently experience a torque. The torque acting on spacecraft m can be determined by taking the sum of the cross products between the moment arms and the forces experienced by each pole:

$$\overrightarrow{T}_m = \sum_{n=1}^{N-1} \left[\overrightarrow{r}_{mN,mn} \times \sum_{\substack{a=1 \\ a \neq m}}^M \sum_{b=1}^N \overrightarrow{F}_{ab,mn} \right], \quad (\text{C.1.3})$$

where the N -th pole of each spacecraft represents the centroid of the spacecraft and $\overrightarrow{r}_{mN,mn}$ is the position vector of the n -th pole of the m -th spacecraft relative to the center of the spacecraft, written in the inertial reference frame. This torque equation can then be substituted into the Euler equation to obtain the angular acceleration vector ($\dot{\omega}_m$) of the m -th spacecraft. The Euler equation can be written in terms of either the inertial reference frame or the respective spacecraft body coordinate system. To simplify the calculation, the latter coordinate system is chosen such that the direction of the three spacecraft angular rates coincide with the principal axes of the spacecraft. The angular acceleration of the spacecraft, written in terms of the spacecraft body coordinates, is therefore:

$$\ddot{\omega}_{m,B} = \mathbf{I}_{p,m}^{-1} \left[\sum_{n=1}^N \sum_{\substack{a=1 \\ a \neq m}}^M \sum_{b=1}^N (\vec{r}_{mn} \times \mathbf{Q}_m^T \vec{\mathbf{F}}_{ab,mn}) - \vec{\omega}_m \times \mathbf{I}_{p,m} \vec{\omega}_m \right]_B, \quad (\text{C.1.4})$$

where \mathbf{Q}_m is the rotational matrix describing the orientation of the spacecraft in the inertial reference frame, and $\mathbf{I}_{p,m}$ is the spacecraft's inertia matrix about its principal axes.

Finally, since magnetic monopoles do not exist, the sum of the charges on each spacecraft must be equal to zero:

$$\sum_{n=1}^N q_{mn} = 0. \quad (\text{C.1.5})$$

C.2 State Space Representation

In an M -spacecraft system, the total number of acceleration vectors is simply M . These acceleration vectors are defined with respect to the inertial reference frame. Of importance, however, are the *relative* displacements and velocities between the spacecraft since it is the *difference* in path lengths that light rays travel that must be controlled. The position and velocity vector for the M -1 spacecraft relative to the first spacecraft is:

$$\vec{x}_p = \begin{bmatrix} \vec{x}_{1,2} & \vec{x}_{1,3} & \dots & \vec{x}_{1,M} & \vec{\dot{x}}_{1,2} & \dots & \vec{\dot{x}}_{1,3} & \vec{\dot{x}}_{1,M} \end{bmatrix}^T, \quad (\text{C.2.1})$$

where each relative position (and corresponding relative velocity) consists of the three cartesian coordinate variables (x , y , and z), making the total number of position and velocity state variables equal to $6*(M-1)$.

The attitude control for each spacecraft is described using a quaternion representation. Although this requires four variables to characterize the attitude, instead of three as in an Euler angle representation, ambiguities that are inherent using Euler angles are completely eliminated using quaternions. The quaternion variables for each spacecraft in the system are:

$$\vec{\epsilon}_m = [\epsilon_{1,m} \ \epsilon_{2,m} \ \epsilon_{3,m} \ \epsilon_{4,m}]^T, \quad (\text{C.2.2})$$

while the angular velocities for the spacecraft are described using only three variables:

$$\vec{\omega}_{m,B} = [\omega_{1,m} \ \omega_{2,m} \ \omega_{3,m}]^T_B. \quad (\text{C.2.3})$$

Hence, for each spacecraft, seven variables are required to describe the attitude of the spacecraft, and for the entire system, $7M$ variables are required. To adequately describe the system in state space representation, the quaternion rates in terms of the quaternion and angular velocities are given by:

$$\begin{aligned} \dot{\vec{\epsilon}}_{1-3,m} &= \frac{1}{2} (\vec{\epsilon}_{1-3,m} \times + \vec{\epsilon}_{4,m} \mathbf{I}) \vec{\omega}_{m,B}, \\ \dot{\vec{\epsilon}}_{4,m} &= -\frac{1}{2} \vec{\epsilon}_{1-3,m}^T \vec{\omega}_{m,B} \end{aligned}, \quad (\text{C.2.4})$$

where the $\vec{\epsilon}_{1-3,m}$ vector represents the first three quaternion variables, $\vec{\epsilon}_{4,m}$ represents the fourth, and \mathbf{I} represents the identity matrix. The notation $(\vec{\epsilon}_{1-3,m})^\times$ represents the formation of the skew-symmetric matrix $\vec{\epsilon}_{1-3,m}^\times$ from the elements of $\vec{\epsilon}_{1-3,m}$ according to the pattern given by:

$$\vec{\epsilon}_{1-3,m}^\times \equiv \begin{bmatrix} 0 & -\epsilon_3 & \epsilon_2 \\ \epsilon_3 & 0 & -\epsilon_1 \\ -\epsilon_2 & \epsilon_1 & 0 \end{bmatrix}. \quad (\text{C.2.5})$$

To summarize, for a system with M spacecraft, the total number of variables required to adequately describe the system is $13M-6$. In this paper, these variables are arranged as follow:

$$\vec{x} = \left[\overrightarrow{\Delta x}_{1,2} \dots \overrightarrow{\Delta x}_{1,M} \varepsilon_1 \dots \varepsilon_M \overrightarrow{\dot{\Delta x}}_{1,2} \dots \overrightarrow{\dot{\Delta x}}_{1,M} \omega_{1,B} \dots \omega_{M,B} \right]^T. \quad (\text{C.2.6})$$

The control variables in this system are the strengths of the charges in the poles. Since the total charge for each N -pole spacecraft must equate to zero, as in (C.1.5), the number of control variables for each spacecraft is simply $N-1$:

$$\vec{u}_m = [q_{m,1} \ q_{m,2} \ \dots \ q_{m,N-1}]^T, \quad (\text{C.2.7})$$

and for the entire system, the total number of control variables is $M(N-1)$.

Linearization

The dynamic (**A**) and control (**B**) matrices in the control framework are obtained by linearizing the equations of motions with respect to the state and control variables. For this, both the force and torque equations must be explicitly expressed in terms of the state and control variables.

In both the force and torque equations, the EM forces are directly dependent on the position vectors between the poles of interest, as demonstrated by Equations (C.1.1)-(C.1.3). Since the N -th node of each spacecraft is defined as the centroid of the spacecraft, the position vector $\overrightarrow{r}_{ab,mn}$ can then be rewritten in terms of the state variables given by (C.2.6):

$$\overrightarrow{r}_{ab,mn} = \overrightarrow{\Delta x}_{1,m} - \overrightarrow{\Delta x}_{1,a} + \mathbf{Q}_m \overrightarrow{r}_{mn} - \mathbf{Q}_a \overrightarrow{r}_{ab}, \quad (\text{C.2.8})$$

where the first two terms form the position vector between the m -th and a -th spacecraft centroids, and \mathbf{Q}_m and \mathbf{Q}_a are the rotational matrices describing the spacecraft orientations in the inertial reference frame using the quaternion variables:

$$\mathbf{Q}_m = \begin{bmatrix} \varepsilon_1^2 - \varepsilon_2^2 - \varepsilon_3^2 + \varepsilon_4^2 & 2(\varepsilon_1\varepsilon_2 - \varepsilon_3\varepsilon_4) & 2(\varepsilon_1\varepsilon_3 + \varepsilon_2\varepsilon_4) \\ 2(\varepsilon_1\varepsilon_2 + \varepsilon_3\varepsilon_4) & -\varepsilon_1^2 + \varepsilon_2^2 - \varepsilon_3^2 + \varepsilon_4^2 & 2(\varepsilon_2\varepsilon_3 - \varepsilon_1\varepsilon_4) \\ 2(\varepsilon_1\varepsilon_3 - \varepsilon_2\varepsilon_4) & 2(\varepsilon_2\varepsilon_3 + \varepsilon_1\varepsilon_4) & -\varepsilon_1^2 - \varepsilon_2^2 + \varepsilon_3^2 + \varepsilon_4^2 \end{bmatrix}_m. \quad (\text{C.2.9})$$

The \overrightarrow{r}_{mn} and \overrightarrow{r}_{ab} vectors are the position vectors of the poles relative to the center node of the respective spacecraft, written in the spacecraft body frame. Thus, the position and rotation equations of motion can now be written entirely in terms of the state variables defined in (C.2.6).

The final step in the process is to linearize the equations of motion with respect to both the state and control variables. Expanding the two equations of motion about a nominal trajectory and ignoring second and higher order terms, the general linearization of these equations can be written as:

$$\dot{\vec{x}} = \frac{\partial}{\partial \vec{x}} f(\vec{x}, \vec{u}) \Big|_{(\vec{x}_o, \vec{u}_o)} \vec{x} + \frac{\partial}{\partial \vec{u}} f(\vec{x}, \vec{u}) \Big|_{(\vec{x}_o, \vec{u}_o)} \vec{u}, \quad (\text{C.2.10})$$

where the partial derivative with respect to $\dot{\vec{x}}$ is the **A** matrix, and that with respect to \vec{u} is the **B** matrix.

A & B Matrix Organization

The **A** and **B** matrices are now generated by taking the partial derivatives of the linear and angular acceleration equations with respect to the state and control variables. Based upon the state and control vector organizations in (C.2.6) and (C.2.7), the resultant **A** matrix is organized as follows:

$$\mathbf{A} = \begin{bmatrix} 0 & 0 & \mathbf{I} & 0 \\ 0 & \mathbf{A}_{b,b} & 0 & \mathbf{A}_{b,d} \\ \mathbf{A}_{c,a} & \mathbf{A}_{c,b} & 0 & 0 \\ \mathbf{A}_{d,a} & \mathbf{A}_{d,b} & 0 & \mathbf{A}_{d,d} \end{bmatrix} \quad \begin{array}{c} \rightarrow 1 \\ \vdots \\ \rightarrow 3M-3 \\ \rightarrow 3M-2 \\ \vdots \\ \rightarrow 7M-3 \\ \rightarrow 7M-2 \\ \vdots \\ \rightarrow 10M-6 \\ \rightarrow 10M-5 \\ \vdots \\ \rightarrow 13M-6 \end{array} \quad \begin{array}{c} \overrightarrow{\Delta x} \\ \overrightarrow{\dot{\epsilon}} \\ \overrightarrow{\ddot{x}} \\ \overrightarrow{\omega} \end{array} . \quad (C.2.11)$$

It is a $13M - 6$ square matrix with a number of distinct features. The first is an identity matrix relating the rates of the state variables on both sides of the dynamic equation. The second row is the result of using the quaternion variables to represent the orientation of each spacecraft. These two entries ($\mathbf{A}_{b,b}$ and $\mathbf{A}_{b,d}$) are block diagonal, since the orientation description of each spacecraft is independent of the other. Then there is the fully populated bottom left corner of the matrix. These entries comprise the relative linear and angular accelerations of all the spacecraft differentiated with respect to the state variables. Since the linear and the angular accelerations are affected by the orientation and the relative separations of the spacecraft, the resulting square matrix is of the size $7M - 3$. The final entry in the matrix results from the angular rates given by the Euler equation.

The corresponding \mathbf{B} matrix is given by:

$$\mathbf{B} = \begin{bmatrix} 0 & \rightarrow 1 \\ 0 & \vdots \\ 0 & \rightarrow 3M-3 \\ 0 & \rightarrow 3M-2 \\ \mathbf{B}_c & \vdots \\ \mathbf{B}_d & \rightarrow 7M-3 \\ \vdots & \rightarrow 7M-2 \\ \vdots & \rightarrow 10M-6 \\ \vdots & \rightarrow 10M-5 \\ \vdots & \rightarrow 13M-6 \end{bmatrix} \quad \begin{array}{c} \overrightarrow{\Delta x} \\ \overrightarrow{\dot{\epsilon}} \\ \overrightarrow{\ddot{x}} \\ \overrightarrow{\omega} \end{array} .$$

The first two rows are simply zero, since the control variables exist only in the force and torque equations. This $(13M - 6) \times M(N - 1)$ matrix only considers $N - 1$ control variables for each spacecraft, in compliance with the constraint in (C.1.5).

C.3 Controllability

The controllability for a separated-spacecraft interferometer using the EMFF concept is explored by first considering a two-spacecraft system. Both the dynamics (\mathbf{A}) and control (\mathbf{B}) matrices are needed to obtain the controllability matrix, C :

$$C = \left[B \ AB \ A^2B \ \dots \ A^{n-1}B \right], \quad (C.3.1)$$

where n is the size of the square \mathbf{A} matrix. In order for the system to be fully controllable, C must be of full rank, n .

Dipole

For a two-spacecraft system with the dipole axes aligned with each other in a two-dimensional space, there should only be eight state variables: two for the relative x and y position variables, two for the corresponding velocities, one each for the rotation of each spacecraft about the z axis, and one each for the corresponding rotation rates. This seems to contradict the ten state variables given by the new control matrices. The difference comes from the fact that a quaternion representation is used to describe the spacecraft rotation variables. Instead of the three variables in an Euler-angle representation, the quaternion representation requires four variables. However, the quaternion variables for each spacecraft must also satisfy the following contrarian:

$$\varepsilon_1^2 + \varepsilon_2^2 + \varepsilon_3^2 + \varepsilon_4^2 = 1. \quad (C.3.2)$$

When reducing the original control matrices, the last two of the four quaternion variables for each spacecraft must be maintained, since they are not necessarily zero. Therefore, in order to determine the controllability of this reduced system, the rank of the C matrix needs to be only eight.

The \mathbf{A} and \mathbf{B} matrices for this two-spacecraft dipole example give a controllability matrix with a rank of only two. With the axes of the dipoles aligned, one can intuitively observe that only the position and velocity along the vector connecting the spacecraft can be controlled by varying the currents in the dipoles. It also makes sense that it is not possible to control eight states with only two control variables.

Y-pole

Instead of dipoles, now consider a two-spacecraft system with *three* poles each. The poles are arranged so that they are evenly distributed at 120° apart, and this configuration is referred to as a Y-pole.

The rank of the controllability matrix using the Y-pole configuration is eight. Compared to the dipole case, two more control variables have been added, while the number of state variables to be controlled remains the same. Although the number of variables is still eight, the number of directions to be controlled is only four. Hence the four control variables are adequate to control the two-spacecraft Y-pole system.

TPF 2-D Case

Extending the analysis to the five-spacecraft TPF interferometer, full controllability of the interferometer is only achieved if a rank of 26 is achieved for the C matrix. In the case when all the spacecraft have dipoles, a rank of only eight is achieved. However, when the spacecraft have Y-poles, the rank of the system is 26. This indicates that full controllability of the TPF interferometer in two-dimensional space can only be achieved if the number of poles assigned for each spacecraft is at least three. Note that the number of control variables in this case is only ten (five spacecraft, each with two control variables) compared to the 13 independent state variables.

TPF 3-D Case

Further extending the analysis to consider the TPF interferometer in three-dimensional space indicates that a four-pole configuration must be implemented before full controllability of the interferometer can be achieved. For this three-dimensional case, the full rank of 54 is only achieved when all four poles on each spacecraft are arranged such that they are not contained in the same plane. A possible configuration is to place the nodes on the vertices of a triangular-based pyramid. Again, similar to the previous case, the number of control variables (15) required is actually less than the number of independent state variables (27).

APPENDIX D. ONE-DIMENSIONAL DYNAMICS AND CONTROL THEORY

D.1 Steady-State-Spin Dynamics and Control Derivation

Maintaining steady-state spin (Figure D.1.1) requires a careful balance between the centripetal force and the required electromagnetic force. If this balance is perturbed, the system will respond with a certain dynamic behavior that will need to be controlled. For example, if the spacecraft move apart, the electromagnetic force will drop faster than the centripetal force, causing the spacecraft to continue to separate. This corresponds to an unstable or divergent mode. Modeling these dynamics allows us to derive the needed control.

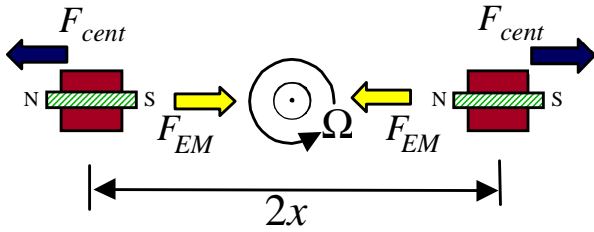


Figure D.1.1 Two spacecraft with electromagnets undergoing steady-state spin about the system center of mass.

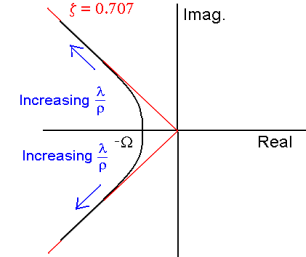


Figure D.1.2 Closed-loop pole trajectories for increasing gain.

If any perturbation to the separation between the spacecraft is caused by some internal source, we can assume that the system angular momentum is conserved under perturbed motion. Therefore, the electromagnetic and centripetal forces are given by

$$F_{EM} = \frac{c_0 \mu^2}{(2x)^4} , \quad F_{cent} = \frac{mv^2}{x} = m\Omega^2 x = \frac{mh^2}{x^3} , \quad (\text{D.1.1})$$

where

$$c_0 = \frac{3\mu_0}{2\pi} , \quad (\text{D.1.2})$$

$\mu_0 = 4\pi \cdot 10^{-7}$ T·m/A is the permeability constant, $2x$ is the spacecraft separation distance, v is the tangential velocity, and Ω is the cluster spin rate. The magnetic moment, μ , and the mass, m , are assumed to be the same for both spacecraft. The angular momentum of the system, divided by total mass, is conserved and is given by

$$h = \frac{H}{2m} = \Omega x^2 . \quad (\text{D.1.3})$$

The radial acceleration in the separation between spacecraft is determined by the imbalance between these two forces. Applying a perturbation, ∂x , about the nominal separation, x_0 ,

$$x = x_0 + \partial x , \quad (\text{D.1.4})$$

as well as a perturbation, $\partial \mu$, about the nominal control, μ_{avg} ,

$$\mu = \mu_{avg} + \partial \mu , \quad (\text{D.1.5})$$

the governing equation of motion is

$$m(\ddot{x}_0 + \partial \ddot{x}) = \frac{mh^2}{(x_0 + \partial x)^3} - \frac{c_0(\mu_{avg} + \partial \mu)^2}{16(x_0 + \partial x)^4} . \quad (\text{D.1.6})$$

Linearizing in terms of small perturbations ($\delta x/x_0$ small) and solving the steady portion of this equation ($\ddot{x} = 0$) gives the steady-state control required to provide the centripetal load when no perturbation exists:

$$\mu_{avg}^2 = \frac{16mx_0h^2}{c_0} = \frac{16m\Omega^2x_0^5}{c_0} . \quad (\text{D.1.7})$$

The perturbation equation then reduces to

$$\frac{\partial \ddot{x}}{x_0} - \Omega^2 \frac{\partial x}{x_0} = -2\Omega^2 \frac{\partial \mu}{\mu_{avg}} , \quad (\text{D.1.8})$$

which has poles at $\pm\Omega$. Hence one pole is stable, and the other is unstable and divergent, as predicted. These poles are the characteristic frequencies of the system. To stabilize the unstable pole, which increases with spin rate, requires that the inductance of the electromagnetic coil be small enough to provide a characteristic electrical frequency one to two orders of magnitude higher than the spin rate.

To derive the control for this system, the equation of motion is first placed in state-space form:

$$\begin{bmatrix} \frac{\partial \dot{x}}{x_0} \\ \frac{\partial \ddot{x}}{x_0} \end{bmatrix} = \begin{bmatrix} 0 & 1 \\ \Omega^2 & 0 \end{bmatrix} \begin{bmatrix} \frac{\partial x}{x_0} \\ \frac{\partial \dot{x}}{x_0} \end{bmatrix} + \begin{bmatrix} 0 \\ -2\Omega^2 \end{bmatrix} \frac{\partial \mu}{\mu_{avg}} \Leftrightarrow \dot{x} = Ax + Bu . \quad (\text{D.1.9})$$

Modern control techniques can now be used to determine the feedback gains and closed-loop poles for a cost-efficient controller. To develop this controller, a cost function is created to weigh the importance of different parameters. R_{xx} is defined as a two-by-two matrix that penalizes differences in radial separation or relative velocity of the vehicles. R_{uu} is a scalar that penalizes the use of control. Because the controller commands power to be supplied to the actuators, controlling the system has a cost of power. The cost function, J , weighs the importance of accuracy in positioning the satellites with the limited resource of power:

$$J = \int_0^\infty [\dot{x}^T R_{xx} \dot{x} + R_{uu} u^2] dt . \quad (\text{D.1.10})$$

The control that minimizes the cost is

$$u = -R_{uu}^{-1} B^T P \dot{x} = -K \dot{x} , \quad (\text{D.1.11})$$

where P is a symmetric, positive-semidefinite matrix found by solving the Algebraic Riccati Equation:

$$R_{xx} + PA + A^T P - PBR_{uu}^{-1}B^T P = 0 . \quad (\text{D.1.12})$$

If we penalize the mean square displacement with a weight λ , penalize the control power with a weight ρ , and enforce the symmetry of P :

$$R_{xx} = \begin{bmatrix} \lambda & 0 \\ 0 & 0 \end{bmatrix} , \quad R_{uu} = \rho , \quad P = \begin{bmatrix} P_{11} & P_{12} \\ P_{12} & P_{22} \end{bmatrix} , \quad (\text{D.1.13})$$

then the displacement and velocity gains of the most efficient controller can be calculated from (D.1.9) and (D.1.11)-(D.1.13) for any given ratio of penalties, λ and ρ :

$$K = - \begin{bmatrix} \frac{1}{2} \left(1 + \sqrt{1 + 4\frac{\lambda}{\rho}} \right) & \frac{1}{\sqrt{2}\Omega} \sqrt{1 + \sqrt{1 + 4\frac{\lambda}{\rho}}} \end{bmatrix} . \quad (\text{D.1.14})$$

If the ratio λ/ρ is evaluated from 0 to ∞ , a graph of the closed-loop poles for the most efficient controller can be created (Figure D.1.2). When the ratio is zero, use of control is infinitely expensive, yet control effort must be expended to stabilize the unstable pole. Therefore, both poles are both located at $-\Omega$. When the ratio tends toward infinity, use of control becomes cheap, and the closed loop poles move out to infinity along 45° asymptotes, where the damping ratio is 0.707. The stabilization of these unstable open-loop dynamics is one of the challenges in electromagnetic formation flight.

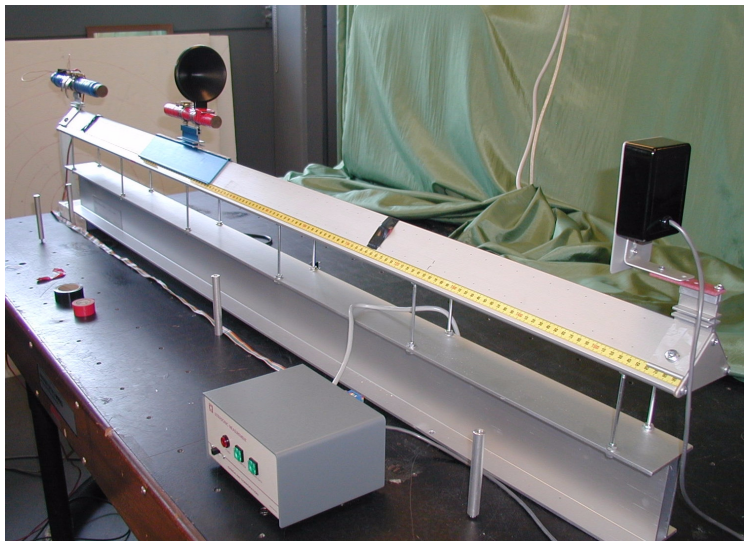


Figure D.1.3 Airtrack used to demonstrate electromagnetic control of stable and unstable systems.

D.2 Airtrack Dynamics and Control Derivation

The control analysis in the previous section demonstrates some interesting characteristics of a rotating formation flight cluster. Of particular interest is the fact that a two-satellite cluster has open-loop poles that are real and equal to the positive and negative values of the spin rate, $+\Omega$ and $-\Omega$, respectively. Hence the rotating system is unstable, with one pole lying in the right-half complex plane.

Without a multi-body testbed on which to perform experiments, it is difficult to demonstrate closed-loop, stable control of an inherently unstable spinning cluster. However, if we can demonstrate control of an unstable system *with similar dynamics to the rotating cluster*, we will gain confidence in our ability to use electromagnetic control for disturbance rejection in rotating clusters. We now consider such a system: a linear airtrack that can be configured in either a *stable* or *unstable* geometry.

Airtrack Description

The airtrack, shown in Figure D.1.3, is a one-dimensional platform on which bodies are allowed to translate, while constrained to linear motion. The bodies are levitated by compressed air flowing through small holes in the track surface, and thus “float” on the nearly frictionless surface.

If electromagnets are placed on the airtrack, they can be used to create forces to attract or repel one other, thus controlling their relative distance. If, instead, an electromagnet is fixed to one end of the track and a permanent magnet is allowed to translate along the track, the fixed electromagnet can be used to control the separation distance of the free permanent magnet, while eliminating any wires that would be connected to the free magnet, and thus avoiding corruption of its nearly frictionless dynamics. Figure D.1.3 shows an electromagnet fixed to the far end of the track and a permanent magnet on a “slider,” free to translate along the track. The fixed electromagnet is composed of copper wires wound several times around an iron core. Control is thus modulated by running current through the wire, and the direction and magnitude of the current determine the direction and magnitude of the force between the two magnets.

Since the goal is to implement feedback control, a sensory measurement of the distance between the two magnets is required. This is provided by an ultrasonic displacement sensor, shown fixed to the near end of the track in Figure D.1.3. The transceiver emits an ultrasonic signal, which reflects off the cone attached to the free magnet. The transceiver receives the reflected signal and calculates the distance at a 30 Hz update rate, based on the speed of sound and the time of flight. The separation distance between the two magnets is then computed by subtracting the measured distance from the length of the airtrack.

Finally, to implement feedback control, a real-time computer is used to process the sensor data, compute the required control, and output the control signal through an amplifier to the electromagnet. dSPACE hardware and software were used with a desktop computer for both data acquisition and real-time control. Figure D.2.1 shows a virtual control panel designed for this system. It allows the user to monitor variables such as the measured distance, the separation distance between the magnets, and both the raw and amplified control signal. It also allows one to tune the various control gains using virtual knobs or numeric inputs.

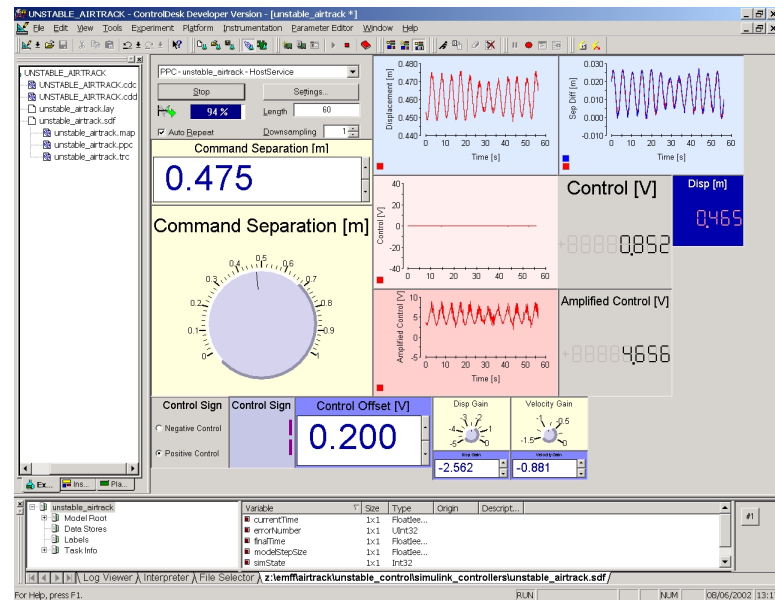


Figure D.2.1 Sample virtual control panel used with airtrack system.

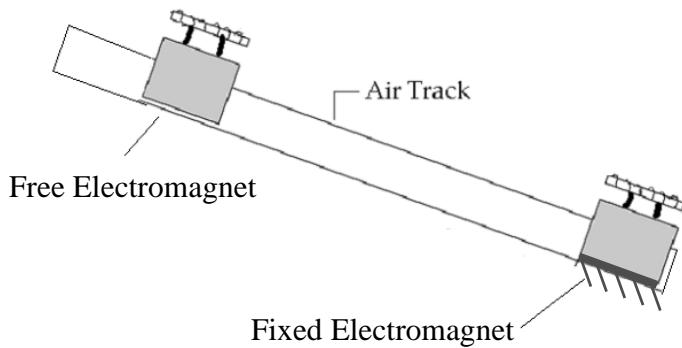


Figure D.2.2 Schematic of the stable airtrack configuration.

Stable Airtrack Configuration

A schematic of the stable airtrack configuration is shown in Figure D.2.2. One electromagnet is fixed to the end of the track, another electromagnet is free to float along the length of the track, and the track is inclined so that the free magnet lies above the fixed magnet. (Figure D.2.2 is exaggerated; the actual inclination used in these experiments is roughly two degrees.) The free magnet tends to fall toward the fixed magnet because of the gravitational force acting

on it. The magnets must then repel each other in order to maintain a fixed separation distance while counteracting the gravitational force and other disturbances. The goal for this configuration is to control the separation distance between the two magnets as precisely as possible, while rejecting disturbances to the system.

Stable Airtrack Control

As in Section D.1, we assume the two electromagnets have identical magnetic moments, μ , so that the repulsive force between the two magnets separated at a distance x is:

$$F_{EM} = \frac{c_0 \mu^2}{x^4} \quad (\text{D.2.1})$$

The gravitational force acting on the free magnet is:

$$F_g = mg \sin\theta \quad (\text{D.2.2})$$

where θ is the inclination angle of the airtrack.

Balancing the forces acting on the free magnet allows us to write the equation of motion for this system:

$$m\ddot{x} = F_{EM} - F_g = \frac{c_0 \mu^2}{x^4} - mg \sin\theta \quad (\text{D.2.3})$$

Assuming small displacements, we linearize this equation about a nominal separation distance, x_0 , and a nominal steady-state control, μ_{avg} , so that:

$$x = x_0 + \partial x, \quad \frac{\partial x}{x_0} \ll 1 \quad (\text{D.2.4})$$

$$\mu = \mu_{avg} + \partial\mu, \quad \frac{\partial\mu}{\mu_{avg}} \ll 1 \quad (\text{D.2.5})$$

and ∂x and $\partial\mu$ are small perturbations from the nominal values.

The equation of motion, (D.2.1), becomes:

$$m(\ddot{x}_0 + \ddot{\partial x}) = \frac{c_0(\mu_{avg} + \partial\mu)^2}{(x_0 + \partial x)^4} - mg \sin\theta \quad (\text{D.2.6})$$

Solving the steady portion of this equation ($\ddot{x} = 0$) gives the steady-state control required to counteract the gravitational force when no perturbation exists:

$$\mu_{avg}^2 = \frac{mg \sin\theta x_0^4}{c_0}. \quad (\text{D.2.7})$$

Neglecting higher order terms, the perturbation equation then reduces to

$$\ddot{\partial x} + \frac{4c_0\mu_{avg}^2}{mx_0^5}\partial x = \frac{2c_0\mu_{avg}\partial\mu}{mx_0^4}, \quad (\text{D.2.8})$$

which has poles at $\pm j\sqrt{4c_0\mu_{avg}^2/mx_0^5}$. Hence this “stable” system is actually neutrally stable, with two poles on the imaginary axis. The small amount of friction on the airtrack system will bring the poles slightly into the left-half complex plane.

Performing an analysis similar to the one in Section D.1, we find the optimal control gains for this stable airtrack system:

$$K = \begin{bmatrix} -2\mu_{avg} \left[1 + \sqrt{1 + \frac{\lambda}{\rho} \left(\frac{x_0}{2\mu_{avg}} \right)^2} \right] & \sqrt{\frac{-2mx_0^3}{c_0} \left(1 - \frac{x_0}{2\mu_{avg}} \sqrt{\frac{\lambda}{\rho} - \frac{mx_0^3}{c_0}} \right)} \end{bmatrix}, \quad (\text{D.2.9})$$

where λ is the penalty on the displacement, ρ is the penalty on the control, and the ratio λ/ρ is left for the user to specify.

Stable Airtrack Experimental Results

Figure D.2.3 shows the poles of the stable airtrack system, as measured from the impulse response. Very light damping due to slight friction from the airtrack surface was neglected, so that the system poles lie approximately on the imaginary axis, at $\pm 1.82j$. Substituting these measured values in place of the analytical poles above, and specifying a control penalty four times that of the displacement penalty ($\lambda/\rho = 1/4$), yields the optimal displacement and velocity gains for the stable airtrack configuration:

$$K = [11.74 \quad 4.33] . \quad (\text{D.2.10})$$

This analysis was adapted to the configuration where the free body is a permanent magnet. The resulting open- and closed-loop step responses are shown in Figure D.2.4, where the separation distance between the fixed and free magnets is plotted as a function of time. As expected, the open-loop response is very lightly damped, making the system slightly stable, instead of neutrally stable. The closed-loop response shows an improvement on the open-loop behavior: the overshoot is reduced and the damping is greater, yielding a much smaller settling time than the open loop response. There is room for improvement, however, since the “steady-state” behavior is still quite noisy, with a ~ 5 cm (or $\sim 10\%$) oscillation about the steady value. This has been attributed to a noisy displacement sensor and model error; work is in progress to improve the sensor signal and the control implementation.

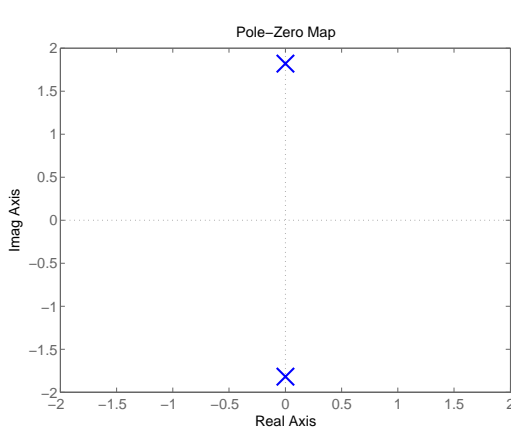


Figure D.2.3 Stable pole locations in the complex plane.

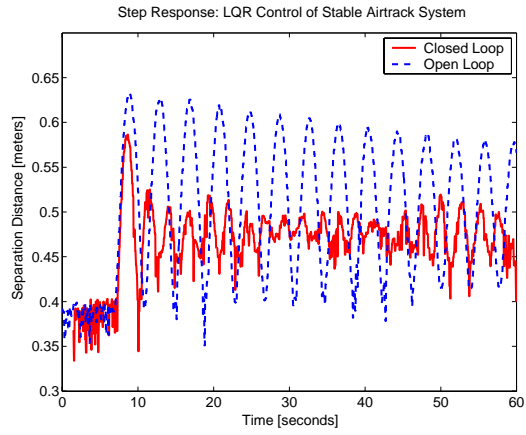


Figure D.2.4 Open- and closed-loop step responses of stable airtrack.

Unstable Airtrack Configuration

A schematic of the unstable airtrack configuration is shown in Figure D.2.5. In this case, the track is tilted in the opposite manner from the stable configuration; the fixed magnet now lies above the free magnet, so that the free magnet tends to fall *away* from the fixed magnet because of the gravitational force acting on it. The magnets must then *attract* each other in order to maintain a fixed separation distance while counteracting the gravitational force and other disturbances.

Unstable Airtrack Control

We now derive the equation of motion for the unstable airtrack configuration. The attractive electromagnetic force between the two magnets is:

$$F_{EM} = \frac{c_0 \mu^2}{x^4} , \quad (\text{D.2.11})$$

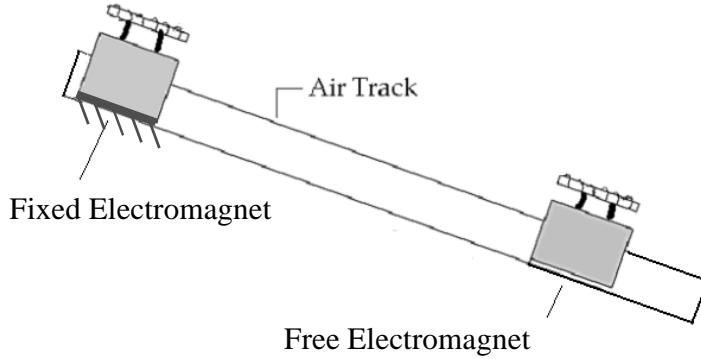


Figure D.2.5 Schematic of the unstable airtrack configuration.

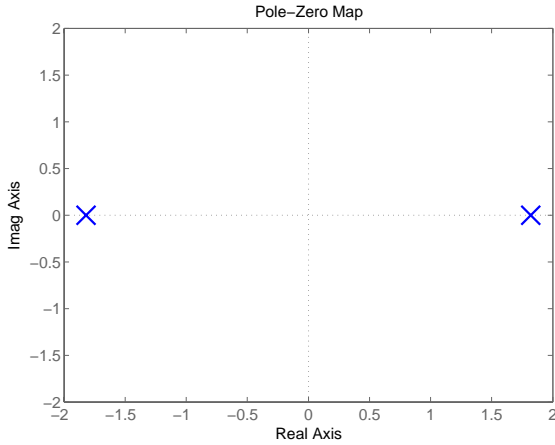


Figure D.2.6 Unstable pole locations in the complex plane.

while the gravitational force acting on the free magnet is:

$$F_g = mg \sin\theta . \quad (\text{D.2.12})$$

Balancing the forces and applying the same perturbation as in the stable airtrack analysis, we find the perturbed equation of motion for this system:

$$m(\ddot{x}_0 + \partial\ddot{x}) = mg \sin\theta - \frac{c_0(\mu_{avg} + \partial\mu)^2}{(x_0 + \partial x)^4} \quad (\text{D.2.13})$$

Solving the steady portion of this equation ($\ddot{x} = 0$) gives the steady-state control required to counteract the gravitational force when no perturbation exists:

$$\mu_{avg}^2 = \frac{mg \sin\theta x_0^4}{c_0} . \quad (\text{D.2.14})$$

Note that the steady-state magnetic moments in the stable configuration have the same magnitude as in this unstable configuration. However, in the stable configuration, the moments of the two magnets are opposite in sign so that the magnets repel one another. In this unstable case, the magnetic moments have the same sign, so that the magnets attract.

Neglecting higher order terms, the perturbation equation reduces to

$$\partial \ddot{x} - \frac{4c_0\mu_{avg}^2}{mx_0^5} \partial x = -\frac{2c_0\mu_{avg}}{mx_0^4} \partial \mu , \quad (\text{D.2.15})$$

which has poles at $\pm\sqrt{4c_0\mu_{avg}^2/mx_0^5}$.

Note that this unstable system's poles have the same magnitude as the stable airtrack's poles, but the two poles now lie on the *real* axis, instead of the imaginary axis. More importantly, we see that **this system's dynamics are nearly identical to those of the satellite cluster spinning at a constant rate**, with poles at $\pm\Omega$, as derived in Section D.1. Since both systems have two real poles, one positive and one negative, mirroring each other in the complex plane, the only difference is the magnitude of the poles. **Thus implementing closed-loop control of this unstable airtrack system would demonstrate our ability to control a system with similar dynamics, such as a rotating formation flight cluster.**

Performing an analysis similar to the one in Section D.1, we find the optimal control gains for this unstable airtrack system:

$$K = \left[\frac{-2\mu_{avg}}{x_0} \left[1 + \sqrt{1 + \frac{\lambda}{\rho} \left(\frac{x_0}{2\mu_{avg}} \right)^2} \right] \quad \sqrt{\frac{2mx_0^3}{c_0} \left(1 + \frac{x_0}{2\mu_{avg}} \sqrt{\frac{\lambda}{\rho} + \frac{mx_0^3}{c_0}} \right)} \right] , \quad (\text{D.2.16})$$

where λ is the penalty on the displacement, ρ is the penalty on the control, and the ratio λ/ρ is left for the user to specify.

Unstable Airtrack Experimental Results

Since one cannot measure the poles for the unstable airtrack configuration as easily as for the stable configuration (i.e. from the open-loop impulse response), we use the stable configuration results to predict the unstable poles. Section demonstrated that the unstable poles should be of the same magnitude as the stable poles, but at positive and negative locations on the *real*, not the imaginary axis. Hence from the stable poles at $\pm 1.82j$, we assume the unstable poles lie at ± 1.82 , as shown in Figure D.2.6. Substituting these values in place of the analytical poles, and specifying a control penalty four times that of the displacement penalty ($\lambda/\rho = 1/4$), yields the optimal displacement and velocity gains for the unstable airtrack configuration:

$$K = -[2.56 \quad 0.88] \quad (\text{D.2.17})$$

This analysis was adapted to the configuration where the free body is a permanent magnet. The resulting open- and closed-loop responses are shown in Figure D.2.7, where the separation distance between the fixed and free magnets is plotted as a function of time. Recall in the stable airtrack configuration that *step responses* were used to gauge the control performance; however, in the unstable configuration, the open-loop response is divergent, so rather than considering a step response, we consider the controllers' abilities to *reject disturbances and maintain a constant separation distance*. The closed-loop response performs fairly well; in addition to stabilizing the inherently unstable system, the controller contains the oscillation to within ~2 cm of the steady-state displacement value, yielding even better performance than in the stable configuration. Also shown are two open-loop responses. In one case, the response diverges because the two magnets fall apart; in the other case, the two magnets come together. In both of these cases, the divergent magnet is stopped by barriers placed at the ends of the airtrack (visible in Figure D.1.3); hence the response becomes constant once the free magnet reaches the barrier.

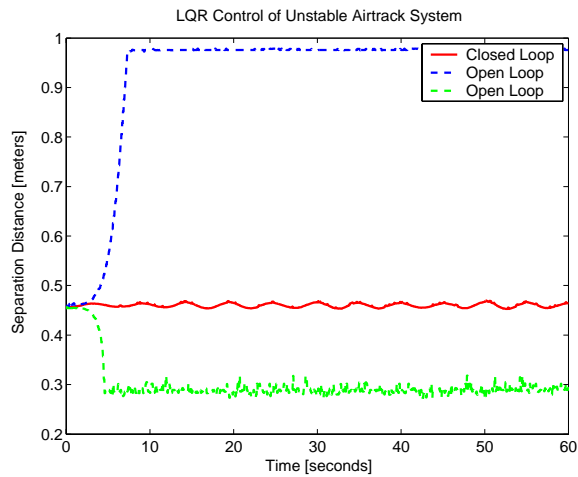


Figure D.2.7 Open- and closed-loop responses of unstable airtrack.

APPENDIX E. THREE-DIMENSIONAL DYNAMICS, INCLUDING GYROSTIFFENING

E.1 Introduction

The goal of the work presented here is to define the nonlinear equations of motion for a two-spacecraft formation flying array undergoing a steady-state spin maneuver. While these equations will capture the nonlinear dynamics of the system being considered, they will be linearized for purposes of control design and stability analysis. Once a controller has been designed using the linearized *design model* of the dynamics, the original nonlinear equations may serve as an *evaluation model* for simulating the closed-loop behavior of the nonlinear system.

In the following sections, we define the geometry of the system being considered, present the nonlinear equations of motion, and linearize the equations of motion.

E.2 System Description

The two-spacecraft array being considered is depicted in Figure E.2.1. The X, Y, Z coordinate frame represents a global, non-rotating frame whose origin lies at the center of mass of the two-spacecraft array. The first spacecraft, denoted as “spacecraft A,” lies at coordinates r, ϕ, ψ . Since the global frame’s origin coincides with the array’s center of mass, and we are considering the two spacecraft to be identical in mass and geometry, the second spacecraft, denoted as “spacecraft B,” lies at coordinates $r, \phi + \pi, -\psi$ (or equivalently $r, \phi, \psi + \pi$).

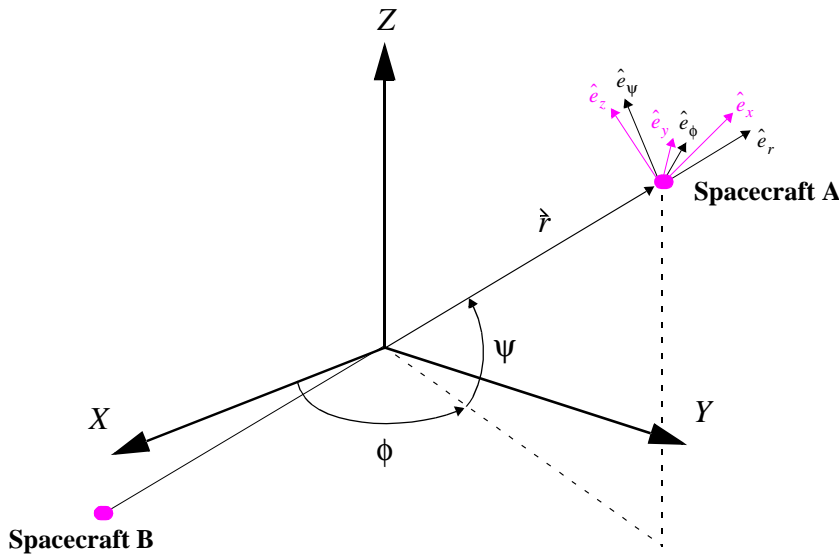


Figure E.2.1 Geometry of Two-Spacecraft Array

While the X, Y, Z and r, ϕ, ψ frames represent global frames, the $\hat{e}_r, \hat{e}_\phi, \hat{e}_\psi$ frame represents a local frame whose origin lies at the center of mass of spacecraft A. The $\hat{e}_r, \hat{e}_\phi, \hat{e}_\psi$ frame is not fixed to the body in that it does not rotate or “tilt” with the spacecraft. Notice the \hat{e}_r vector always aligns with the position vector, \hat{r} , of spacecraft A relative to the origin of the global frame. The x, y, z frame, in contrast, rotates with the body relative to the $\hat{e}_r, \hat{e}_\phi, \hat{e}_\psi$ frame; it is also fixed to the center of mass of spacecraft A.

We now define the relative orientations of the two spacecraft using Euler angles. The Euler angles of spacecraft A are α_1, α_2 , and α_3 , which represent sequential rotations about the body-fixed z, y , and x axes, respectively. Similarly, the orientation of spacecraft B is defined by the Euler angles β_1, β_2 , and β_3 , which represent three sequential rotations about a body-fixed frame on B that is nominally aligned with the r, ϕ, ψ frame on spacecraft A. The nominal orientation of each spacecraft is such that the x, y, z frame aligns with the r, ϕ, ψ frame. In the following sections, we consider perturbations from this nominal orientation; in other words, we consider the dynamics of the x, y, z frame rotating relative to the r, ϕ, ψ frame.

With the variables defined so far and the constraints on the position of spacecraft B:

$$r_B = r_A = r, \quad \phi_B = \phi_A + \pi = \phi + \pi, \quad -\psi_B = \psi_A = \Psi \quad (\text{E.2.1})$$

we have defined 18 state variables that make up the state vector, \mathbf{x} :

$$\mathbf{x} = \begin{bmatrix} r & \phi & \Psi & \alpha_1 & \alpha_2 & \alpha_3 & \beta_1 & \beta_2 & \beta_3 & \dot{r} & \dot{\phi} & \dot{\Psi} & \dot{\alpha}_1 & \dot{\alpha}_2 & \dot{\alpha}_3 & \dot{\beta}_1 & \dot{\beta}_2 & \dot{\beta}_3 \end{bmatrix}^T. \quad (\text{E.2.2})$$

In this analysis, we consider that spacecraft A and B each contain a single electromagnetic dipole oriented along the body-fixed x -axis (and thus aligned with \hat{e}_x when the spacecraft is in its nominal orientation). The magnetic moment of the electromagnet on spacecraft A is defined as:

$$\vec{\mu}_A = \mu_A \hat{e}_x = n_A i_A A_A \hat{e}_x \quad (\text{E.2.3})$$

where n_A is the number of times the conductor is wrapped around to form the electromagnetic coil, i_A is the current running through the coil, and A_A is the cross-sectional area of the coil system. The magnitude of the magnetic moment, μ_A , is assumed constant in this analysis, although its direction, \hat{e}_x , rotates with the spacecraft.

The magnetic moment of the electromagnet on spacecraft B is defined similarly and points along the local body-fixed x -axis on spacecraft B. For this analysis, we assume the same geometry for the coils on both spacecraft, so that:

$$n_B = n_A = n, \quad A_B = A_A = A \quad (\text{E.2.4})$$

However, the currents i_A and i_B are unique and depend on the dynamics and closed-loop control of the system.

Finally, we assume that each spacecraft contains a reaction wheel (RW) whose spin axis is aligned with the body-fixed z -axis. Each RW is spinning at a constant rate, $\Omega_{z,w}$, necessary to conserve the angular momentum of the spinning array. In other words, the sum of the angular momentum stored in the two RWs is equal and opposite to the angular momentum of the two-spacecraft array as it rotates about its own center of mass. Nominally the two spacecraft would assume a circular trajectory in the global X, Y plane ($\psi=0$) with a constant angular velocity, $\dot{\phi} = \phi_0$. In this case, the conservation of angular momentum is expressed as:

$$I_{zz,w} \Omega_{z,w} = m r_0^2 \dot{\phi} \quad (\text{E.2.5})$$

where $I_{zz,w}$ is the RW mass-moment of inertia about its spin axis, m is the mass of each spacecraft, and r_0 is the nominal array radius.

E.3 Nonlinear Equations of Motion

Translational Equations

The translational equations of motion for spacecraft A describe the motion of its center of mass with respect to the global coordinate frame. They may be written as:

$$\ddot{\mathbf{r}} = \begin{Bmatrix} \ddot{r} - r\dot{\psi}^2 - r\dot{\phi}^2 \cos^2 \psi \\ 2\dot{r}\dot{\phi} \cos \psi + r\ddot{\phi} \cos \psi - 2r\dot{\phi}\dot{\psi} \sin \psi \\ 2\dot{r}\dot{\psi} + r\ddot{\psi} + r\dot{\phi}^2 \sin \psi \cos \psi \end{Bmatrix} = \frac{1}{m} \begin{Bmatrix} F_r \\ F_\phi \\ F_\psi \end{Bmatrix}_A \quad (\text{E.3.1})$$

where $\begin{Bmatrix} F_r \\ F_\phi \\ F_\psi \end{Bmatrix}_A$ are the external forces acting on spacecraft A along the local axes $\{\hat{e}_r, \hat{e}_\phi, \hat{e}_\psi\}^T$. We now consider only the forces exerted on spacecraft A by the electromagnet on spacecraft B due to the relative positions and orientations of the two spacecraft. With the Euler angles of each spacecraft as defined in Section E.2, the forces exerted on spacecraft A due to the electromagnetic interaction with spacecraft B are:

$$\begin{Bmatrix} F_r \\ F_\phi \\ F_\psi \end{Bmatrix}_A = \frac{3\mu_0 \mu_A \mu_B}{64\pi r^4} \begin{Bmatrix} s\alpha_1 c\alpha_2 s\beta_1 c\beta_2 - 2c\alpha_1 c\alpha_2 c\beta_1 c\beta_2 + s\alpha_2 s\beta_2 \\ c\alpha_2 c\beta_2 (s\alpha_1 c\beta_1 + s\beta_1 c\alpha_1) \\ -c\beta_1 c\beta_2 s\alpha_2 - c\alpha_1 c\alpha_2 s\beta_2 \end{Bmatrix} \quad (\text{E.3.2})$$

where $\mu_0 = 4\pi \cdot 10^{-7} \text{ T}\cdot\text{m/A}$ is the permeability constant, “s” represents the sine function, and “c” represents the cosine function. Hence the translational equations of motion for spacecraft A are:

$$\begin{Bmatrix} \ddot{r} - r\dot{\psi}^2 - r\dot{\phi}^2 \cos^2\psi \\ 2\dot{r}\dot{\phi} \cos\psi + \ddot{r}\phi \cos\psi - 2r\dot{\phi}\dot{\psi} \sin\psi \\ 2\dot{r}\dot{\psi} + \ddot{r}\psi + r\ddot{\phi}^2 \sin\psi \cos\psi \end{Bmatrix} = \frac{3\mu_0\mu_A\mu_B}{64\pi mr^4} \begin{Bmatrix} s\alpha_1 c\alpha_2 s\beta_1 c\beta_2 - 2c\alpha_1 c\alpha_2 c\beta_1 c\beta_2 + s\alpha_2 s\beta_2 \\ c\alpha_2 c\beta_2 (s\alpha_1 c\beta_1 + s\beta_1 c\alpha_1) \\ -c\beta_1 c\beta_2 s\alpha_2 - c\alpha_1 c\alpha_2 s\beta_2 \end{Bmatrix} \quad (\text{E.3.3})$$

While similar equations of motion may be written for the motion of spacecraft B due to the forces exerted by the electromagnet on spacecraft A, these equations are not necessary for a dynamic simulation; rather, the constraints defined by Equation (E.2.1), along with a knowledge of the position of spacecraft A, are sufficient to determine the position of spacecraft B. Note also that the two spacecraft exert equal and opposite forces on one another, so that:

$$\begin{Bmatrix} F_r \\ F_\phi \\ F_\psi \end{Bmatrix}_A = - \begin{Bmatrix} F_r \\ F_\phi \\ F_\psi \end{Bmatrix}_B \quad (\text{E.3.4})$$

Rotational Equations

We now consider the rotational (“rocking”) equations of motion of spacecraft A. They may be written as:

$$\begin{Bmatrix} I_{rr,s} + I_{rr,w} & 0 & 0 \\ 0 & I_{rr,s} + I_{rr,w} & 0 \\ 0 & 0 & I_{zz,s} \end{Bmatrix}_A \begin{Bmatrix} \ddot{\theta}_x \\ \ddot{\theta}_y \\ \ddot{\theta}_z \end{Bmatrix}_A + \begin{Bmatrix} 0 & \Omega_{z,w} I_{zz,w} & 0 \\ -\Omega_{z,w} I_{zz,w} & 0 & 0 \\ 0 & 0 & 0 \end{Bmatrix} \begin{Bmatrix} \dot{\theta}_x \\ \dot{\theta}_y \\ \dot{\theta}_z \end{Bmatrix}_A = \begin{Bmatrix} T_x \\ T_y \\ T_z \end{Bmatrix}_A \quad (\text{E.3.5})$$

where $\begin{Bmatrix} \dot{\theta}_x \dot{\theta}_y \dot{\theta}_z \end{Bmatrix}_A^T$ are the rotation rates of spacecraft A about its body-fixed x, y, z frame, and $\begin{Bmatrix} T_x T_y T_z \end{Bmatrix}_A^T$ are the external torques on spacecraft A about its body-fixed frame. $I_{zz,s}$ and $I_{zz,w}$ represent the mass-moments of inertia of the spacecraft and RW, respectively, about the body-fixed z -axis. $I_{rr,s}$ and $I_{rr,w}$ represent the spacecraft and RW inertias, respectively, about the body-fixed radial (x and y) axes. Recall that $\Omega_{z,w}$ is the constant spin rate of the RW, so the skew-symmetric damping matrix in Equation (E.3.5) represents gyrostiffening effects of the RW.

Since the orientations of the two spacecraft are represented in terms of their Euler angles, we rewrite Equation (E.3.5) in terms of the Euler angles. The rotational rates and accelerations are:

$$\begin{Bmatrix} \dot{\theta}_x \\ \dot{\theta}_y \\ \dot{\theta}_z \end{Bmatrix}_A = \begin{Bmatrix} \dot{\alpha}_3 - \dot{\alpha}_1 s\alpha_2 \\ \dot{\alpha}_2 c\alpha_3 + \dot{\alpha}_1 c\alpha_2 s\alpha_3 \\ \dot{\alpha}_1 c\alpha_2 c\alpha_3 - \dot{\alpha}_2 s\alpha_3 \end{Bmatrix} \quad (\text{E.3.6})$$

$$\begin{Bmatrix} \ddot{\theta}_x \\ \ddot{\theta}_y \\ \ddot{\theta}_z \end{Bmatrix}_A = \begin{Bmatrix} \ddot{\alpha}_3 - \ddot{\alpha}_1 s\alpha_2 - \dot{\alpha}_1 \dot{\alpha}_2 c\alpha_2 \\ \ddot{\alpha}_2 c\alpha_3 - \dot{\alpha}_2 \dot{\alpha}_3 s\alpha_3 + \ddot{\alpha}_1 c\alpha_2 s\alpha_3 - \dot{\alpha}_1 \dot{\alpha}_2 s\alpha_2 s\alpha_3 + \dot{\alpha}_1 \dot{\alpha}_3 c\alpha_2 c\alpha_3 \\ \ddot{\alpha}_1 c\alpha_2 c\alpha_3 - \dot{\alpha}_1 \dot{\alpha}_2 s\alpha_2 c\alpha_3 - \dot{\alpha}_1 \dot{\alpha}_3 c\alpha_2 s\alpha_3 - \ddot{\alpha}_2 s\alpha_3 - \dot{\alpha}_2 \dot{\alpha}_3 c\alpha_3 \end{Bmatrix} \quad (\text{E.3.7})$$

The torques are easily expressed in the r, ϕ, ψ frame:

$$\begin{Bmatrix} T_r \\ T_\phi \\ T_\psi \end{Bmatrix}_A = \frac{-\mu_0\mu_A\mu_B}{32\pi r^3} \begin{Bmatrix} s\alpha_2 s\beta_1 c\beta_2 - s\alpha_1 c\alpha_2 s\beta_2 \\ c\alpha_1 c\alpha_2 s\beta_2 + 2s\alpha_2 c\beta_1 c\beta_2 \\ c\alpha_1 c\alpha_2 s\beta_1 c\beta_2 + 2s\alpha_1 c\alpha_2 c\beta_1 c\beta_2 \end{Bmatrix} \quad (\text{E.3.8})$$

and must be transformed to the body-fixed x, y, z frame:

$$\begin{Bmatrix} T_x \\ T_y \\ T_z \end{Bmatrix}_A = \begin{bmatrix} 1 & 0 & 0 \\ 0 & c\alpha_3 & s\alpha_3 \\ 0 & -s\alpha_3 & c\alpha_3 \end{bmatrix} \begin{bmatrix} c\alpha_2 & 0 & -s\alpha_2 \\ 0 & 1 & 0 \\ s\alpha_2 & 0 & c\alpha_2 \end{bmatrix} \begin{bmatrix} c\alpha_1 & s\alpha_1 & 0 \\ -s\alpha_1 & c\alpha_1 & 0 \\ 0 & 0 & 1 \end{bmatrix} \begin{Bmatrix} T_r \\ T_\phi \\ T_\psi \end{Bmatrix}_A \quad (\text{E.3.9})$$

Hence while the rotational equation of motion for spacecraft A, Equation (E.3.5), appears to be linear in form, it is actually nonlinear once Equations (E.3.6)-(E.3.9) are substituted and the rotations are expressed in terms of Euler angles.

The nonlinear rotational equations of motion for spacecraft B are similar to those for A:

$$\begin{bmatrix} I_{rr,s} + I_{rr,w} & 0 & 0 \\ 0 & I_{rr,s} + I_{rr,w} & 0 \\ 0 & 0 & I_{zz,s} \end{bmatrix} \begin{Bmatrix} \ddot{\theta}_x \\ \ddot{\theta}_y \\ \ddot{\theta}_z \end{Bmatrix}_B + \begin{bmatrix} 0 & \Omega_{z,w} I_{zz,w} & 0 \\ -\Omega_{z,w} I_{zz,w} & 0 & 0 \\ 0 & 0 & 0 \end{bmatrix} \begin{Bmatrix} \dot{\theta}_x \\ \dot{\theta}_y \\ \dot{\theta}_z \end{Bmatrix}_B = \begin{Bmatrix} T_x \\ T_y \\ T_z \end{Bmatrix}_B \quad (\text{E.3.10})$$

The angular rates and accelerations for spacecraft B are found by substituting the Euler angles β_1, β_2 , and β_3 in place of α_1, α_2 , and α_3 in Equations (E.3.6) and (E.3.7). The torques acting on spacecraft B due to the electromagnet on spacecraft A are:

$$\begin{Bmatrix} T_r \\ T_\phi \\ T_\psi \end{Bmatrix}_B = \frac{-\mu_0 \mu_A \mu_B}{32\pi r^3} \begin{Bmatrix} s\alpha_1 c\alpha_2 s\beta_2 - s\alpha_2 s\beta_1 c\beta_2 \\ s\alpha_2 c\beta_1 c\beta_2 - 4c\alpha_1 c\alpha_2 s\beta_2 \\ s\alpha_1 c\alpha_2 c\beta_1 c\beta_2 - 4c\alpha_1 c\alpha_2 s\beta_1 c\beta_2 \end{Bmatrix} \quad (\text{E.3.11})$$

Expressed about the body-fixed frame on spacecraft B, these torques become:

$$\begin{Bmatrix} T_x \\ T_y \\ T_z \end{Bmatrix}_B = \begin{bmatrix} 1 & 0 & 0 \\ 0 & c\beta_3 & s\beta_3 \\ 0 & -s\beta_3 & c\beta_3 \end{bmatrix} \begin{bmatrix} c\beta_2 & 0 & -s\beta_2 \\ 0 & 1 & 0 \\ s\beta_2 & 0 & c\beta_2 \end{bmatrix} \begin{bmatrix} c\beta_1 & s\beta_1 & 0 \\ -s\beta_1 & c\beta_1 & 0 \\ 0 & 0 & 1 \end{bmatrix} \begin{Bmatrix} T_r \\ T_\phi \\ T_\psi \end{Bmatrix}_B . \quad (\text{E.3.12})$$

E.4 Linearization of Equations of Motion

We now linearize the dynamic equations of motion for spacecraft A and B about some nominal state by assuming that all motions are small relative to the nominal trajectories. We define the nominal trajectories along a circle in the global X, Y plane with a constant angular velocity. Hence the nominal state vector is:

$$\begin{aligned} \mathbf{x}_0 &= \left[r_0 \ \phi_0 \ \Psi_0 \ \alpha_{1,0} \ \alpha_{2,0} \ \alpha_{3,0} \ \beta_{1,0} \ \beta_{2,0} \ \beta_{3,0} \ r_0 \ \dot{\phi}_0 \ \dot{\Psi}_0 \ \dot{\alpha}_{1,0} \ \dot{\alpha}_{2,0} \ \dot{\alpha}_{3,0} \ \beta_{1,0} \ \beta_{2,0} \ \beta_{3,0} \right]^T \\ &= \left[r_0 \ \phi_0(t) \ 0 \ 0 \ 0 \ 0 \ 0 \ 0 \ 0 \ \dot{\phi}_0 \ 0 \ 0 \ 0 \ 0 \ 0 \ 0 \ 0 \right]^T \end{aligned} \quad (\text{E.4.1})$$

Substituting the perturbed state, $\mathbf{x} = \mathbf{x}_0 + \Delta\mathbf{x}$, into the nonlinear equations of motion presented in Section E.3 results in the following linearized equations of motion for the two-spacecraft system. For the translational degrees of freedom of spacecraft A, the linearized equations of motion are:

$$\begin{aligned}
& \begin{bmatrix} 1 & 0 & 0 \\ 0 & r_0 & 0 \\ 0 & 0 & r_0 \end{bmatrix} \begin{Bmatrix} \Delta \ddot{r} \\ \Delta \ddot{\phi} \\ \Delta \ddot{\psi} \end{Bmatrix} + \begin{bmatrix} 0 & -2r_0\dot{\phi}_0 & 0 \\ 2\dot{\phi}_0 & 0 & 0 \\ 0 & 0 & 0 \end{bmatrix} \begin{Bmatrix} \Delta \dot{r} \\ \Delta \dot{\phi} \\ \Delta \dot{\psi} \end{Bmatrix} + \begin{bmatrix} -\dot{\phi}_0^2 & 0 & 0 \\ 0 & 0 & 0 \\ 0 & 0 & r_0\dot{\phi}_0^2 \end{bmatrix} \begin{Bmatrix} \Delta r \\ \Delta \phi \\ \Delta \psi \end{Bmatrix} + \begin{Bmatrix} -r_0\dot{\phi}_0^2 \\ 0 \\ 0 \end{Bmatrix} \\
& = \frac{-3\mu_0\mu_A\mu_B}{64\pi mr_0^4} \begin{Bmatrix} 2 - \frac{8\Delta r}{r_0} \\ \Delta\alpha_2 + \Delta\beta_2 \\ -\Delta\alpha_1 - \Delta\beta_1 \end{Bmatrix} \tag{E.4.2}
\end{aligned}$$

Recall that the position of spacecraft B is determined from the position of A and the constraints in Equation (E.2.1).

For the rotational degrees of freedom of spacecraft A, the linearized equations of motion are:

$$\begin{aligned}
& \begin{bmatrix} I_{rr,s} + I_{rr,w} & 0 & 0 \\ 0 & I_{rr,s} + I_{rr,w} & 0 \\ 0 & 0 & I_{zz,s} \end{bmatrix} \begin{Bmatrix} \Delta \ddot{\alpha}_3 \\ \Delta \ddot{\alpha}_2 \\ \Delta \ddot{\alpha}_1 \end{Bmatrix} + \begin{bmatrix} 0 & \Omega_{z,w} I_{zz,w} & 0 \\ -\Omega_{z,w} I_{zz,w} & 0 & 0 \\ 0 & 0 & 0 \end{bmatrix} \begin{Bmatrix} \Delta \dot{\alpha}_3 \\ \Delta \dot{\alpha}_2 \\ \Delta \dot{\alpha}_1 \end{Bmatrix} \\
& = \frac{-\mu_0\mu_A\mu_B}{32\pi r_0^3} \begin{Bmatrix} 0 \\ \Delta\alpha_2 + \Delta\beta_2 \\ \Delta\alpha_1 + \Delta\beta_1 \end{Bmatrix} \tag{E.4.3}
\end{aligned}$$

and for the rotational degrees of freedom of spacecraft B, the linearized equations of motion are:

$$\begin{aligned}
& \begin{bmatrix} I_{rr,s} + I_{rr,w} & 0 & 0 \\ 0 & I_{rr,s} + I_{rr,w} & 0 \\ 0 & 0 & I_{zz,s} \end{bmatrix} \begin{Bmatrix} \Delta \ddot{\beta}_3 \\ \Delta \ddot{\beta}_2 \\ \Delta \ddot{\beta}_1 \end{Bmatrix} + \begin{bmatrix} 0 & \Omega_{z,w} I_{zz,w} & 0 \\ -\Omega_{z,w} I_{zz,w} & 0 & 0 \\ 0 & 0 & 0 \end{bmatrix} \begin{Bmatrix} \Delta \dot{\beta}_3 \\ \Delta \dot{\beta}_2 \\ \Delta \dot{\beta}_1 \end{Bmatrix} \\
& = \frac{-\mu_0\mu_A\mu_B}{32\pi r_0^3} \begin{Bmatrix} 0 \\ \Delta\alpha_2 - 4\Delta\beta_2 \\ \Delta\alpha_1 - 4\Delta\beta_1 \end{Bmatrix} \tag{E.4.4}
\end{aligned}$$

The nine linearized equations of motion can now be compiled into the following 9×9 second-order matrix equation:

$$\begin{bmatrix}
1 & 0 & 0 & 0 & 0 & 0 & 0 & 0 \\
0 & r_0 & 0 & 0 & 0 & 0 & 0 & 0 \\
0 & 0 & r_0 & 0 & 0 & 0 & 0 & 0 \\
0 & 0 & 0 & I_{zz,s} & 0 & 0 & 0 & 0 \\
0 & 0 & 0 & 0 & I_{rr,s} + I_{rr,w} & 0 & 0 & 0 \\
0 & 0 & 0 & 0 & 0 & I_{rr,s} + I_{rr,w} & 0 & 0 \\
0 & 0 & 0 & 0 & 0 & 0 & I_{zz,s} & 0 \\
0 & 0 & 0 & 0 & 0 & 0 & 0 & I_{rr,s} + I_{rr,w} \\
0 & 0 & 0 & 0 & 0 & 0 & 0 & I_{rr,s} + I_{rr,w}
\end{bmatrix}
\begin{Bmatrix}
\Delta \vec{r} \\
\Delta \ddot{\phi} \\
\Delta \ddot{\psi} \\
\Delta \ddot{\alpha}_1 \\
\Delta \ddot{\alpha}_2 \\
\Delta \ddot{\alpha}_3 \\
\Delta \ddot{\beta}_1 \\
\Delta \ddot{\beta}_2 \\
\Delta \ddot{\beta}_3
\end{Bmatrix}$$

$$+ \begin{bmatrix}
0 & -2r_0\dot{\phi}_0 & 0 & 0 & 0 & 0 & 0 & 0 \\
2\dot{\phi}_0 & 0 & 0 & 0 & 0 & 0 & 0 & 0 \\
0 & 0 & 0 & 0 & 0 & 0 & 0 & 0 \\
0 & 0 & 0 & 0 & 0 & 0 & 0 & 0 \\
0 & 0 & 0 & 0 & 0 & -\Omega_{z,w}I_{zz,w} & 0 & 0 \\
0 & 0 & 0 & 0 & \Omega_{z,w}I_{zz,w} & 0 & 0 & 0 \\
0 & 0 & 0 & 0 & 0 & 0 & 0 & 0 \\
0 & 0 & 0 & 0 & 0 & 0 & 0 & -\Omega_{z,w}I_{zz,w} \\
0 & 0 & 0 & 0 & 0 & 0 & \Omega_{z,w}I_{zz,w} & 0
\end{bmatrix}
\begin{Bmatrix}
\Delta \dot{r} \\
\Delta \dot{\phi} \\
\Delta \dot{\psi} \\
\Delta \dot{\alpha}_1 \\
\Delta \dot{\alpha}_2 \\
\Delta \dot{\alpha}_3 \\
\Delta \dot{\beta}_1 \\
\Delta \dot{\beta}_2 \\
\Delta \dot{\beta}_3
\end{Bmatrix} \quad (E.4.5)$$

$$+ \begin{bmatrix}
\frac{8c_1}{r_0} - \dot{\phi}_0^2 & 0 & 0 & 0 & 0 & 0 & 0 & 0 \\
0 & 0 & 0 & 0 & -c_1 & 0 & 0 & -c_1 & 0 \\
0 & 0 & r_0\dot{\phi}_0^2 & c_1 & 0 & 0 & c_1 & 0 & 0 \\
0 & 0 & 0 & -c_0 & 0 & 0 & -c_0 & 0 & 0 \\
0 & 0 & 0 & 0 & -c_0 & 0 & 0 & -c_0 & 0 \\
0 & 0 & 0 & 0 & 0 & 0 & 0 & 0 & 0 \\
0 & 0 & 0 & -c_0 & 0 & 0 & 4c_0 & 0 & 0 \\
0 & 0 & 0 & 0 & -c_0 & 0 & 0 & 4c_0 & 0 \\
0 & 0 & 0 & 0 & 0 & 0 & 0 & 0 & 0
\end{bmatrix}
\begin{Bmatrix}
\Delta r \\
\Delta \phi \\
\Delta \psi \\
\Delta \alpha_1 \\
\Delta \alpha_2 \\
\Delta \alpha_3 \\
\Delta \beta_1 \\
\Delta \beta_2 \\
\Delta \beta_3
\end{Bmatrix} = \begin{Bmatrix}
r_0\dot{\phi}_0^2 + 2c_1 \\
0 \\
0 \\
0 \\
0 \\
0 \\
0 \\
0 \\
0
\end{Bmatrix}$$

where $c_0 \equiv \frac{-\mu_0\mu_A\mu_B}{32\pi r_0^3}$ and $c_1 \equiv \frac{3c_0}{2mr_0}$.

Equation (E.4.5), along with the constraint defined in Equation (E.2.1), is sufficient to completely characterize the linearized dynamics of the system.

E.5 Summary and Conclusions

In this work, we have defined the geometry for a sample three-dimensional two-spacecraft electromagnetic formation flying array. We have developed the *nonlinear dynamic equations of motion* (the evaluation model) and linearized these equations to yield the *linearized dynamic equations of motion* (the design model). We can now proceed to perform a stability analysis and control design using the linearized design model. The closed-loop control may then be

simulated using the nonlinear evaluation model by substituting the closed-loop magnetic moments into the evaluation model equations.

APPENDIX F. J₂ DISTURBANCE AND THE RESULTING ANGULAR MOMENTUM GAIN

The J₂ effect of the Earth's geopotential is a disturbance acceleration on satellite formations that must be counteracted. The J₂ effect causes three main problems for satellite formations: changes in the orbital period of the satellite, separation of the formation in the cross-track direction, and tumbling of the entire formation. This appendix will look at the effects of fighting the separation in the cross-track direction.

The acceleration of a satellite due to the J₂ force is defined as:

$$\vec{J}_2(\vec{r}) = -\frac{3}{2} \frac{J_2 \mu R_e^2}{r^4} [(1 - 3 \sin^2 i \sin^2 \theta) \hat{x} + (2 \sin^2 i \sin \theta \cos \theta) \hat{y} + (2 \sin i \cos i \sin \theta) \hat{z}] \quad (\text{F.1})$$

where \vec{r} is the position vector of the satellite, and $\hat{x} - \hat{y} - \hat{z}$ is a local vertical, local horizontal, (LVLH) coordinate system with the origin of the coordinate system coinciding with a reference orbit. The \hat{x} vector points in the radial direction, the \hat{z} vector is perpendicular to the orbital plane and points in the direction of the angular momentum vector. Finally, the \hat{y} vector completes the orthogonal triad, and points in the direction of movement. The $\hat{x} - \hat{y} - \hat{z}$ coordinate system is a curvilinear coordinate system. The \hat{x} vector remains unchanged, however the \hat{y} and \hat{z} vectors curve along a sphere with radius r_{ref} .

While J₂ disturbances acting on the formation as a whole are important, it is the difference of the disturbance acceleration between the satellites in the cluster that causes the formation to separate.

Linearizing the J₂ acceleration about one of the satellites produces the following result:

$$\nabla \vec{J}_2(r, \theta, i) = \frac{6\mu J_2 R_E^2}{r_{ref}^5} \begin{bmatrix} (1 - 3 \sin^2 i \sin^2 \theta) & \sin^2 i \sin 2\theta & \sin 2i \sin \theta \\ \sin^2 i \sin 2\theta & -\frac{1}{4} - \sin^2 i \left(\frac{1}{2} - \frac{7}{4} \sin^2 \theta\right) & -\frac{\sin 2i \cos \theta}{4} \\ \sin 2i \sin \theta & -\frac{\sin 2i \cos \theta}{4} & -\frac{3}{4} + \sin^2 i \left(\frac{1}{2} + \frac{5}{4} \sin^2 \theta\right) \end{bmatrix} \quad (\text{F.2})$$

Assuming a two satellite formation with one satellite at the center of a closed Hills orbit, the second satellite will orbit the first (assuming no disturbances) as defined by Hill's equations:

$$\vec{s} = \begin{bmatrix} x = a \cos(\theta + \lambda_1) \\ y = \frac{a}{2} \sin(\theta + \lambda_1) \\ z = b \cos(\theta + \lambda_2) \end{bmatrix} \quad (\text{F.3})$$

One approximation to calculating the differential forces over one orbital period is to take the non-perturbed motion and dot it with the gradient of the J₂ disturbance:

$$F_{\text{differential}} = \vec{s} \cdot \nabla \vec{J}_2 \quad (\text{F.4})$$

where \vec{s} is the relative position of one satellite with respect to another. This differential force is then converted to axial and shear components as defined in section 3.1. The axial force needed to counteract the differential J_2 forces does not produce any torque on the satellite formation. It is the shear component of the force that produces torque on the satellite formation and must be counteracted. Forces in the radial direction are along the axis between the two satellites, and the tangential and normal accelerations are the shear forces with the tangential force lying in the relative orbital plane, and the normal force, normal to this plane. Forces in the tangential and normal direction produce a torque on the satellite system and the net angular momentum gain or loss must be accounted for.

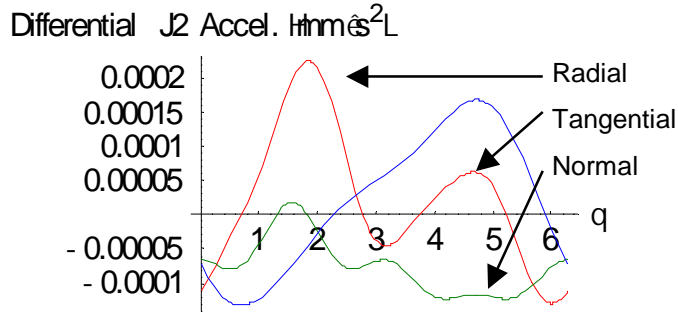


**Figure F.1: Differential J_2 Accelerations over one orbit
(50m Separation Distance)**

Figure F.1 shows the disturbance accelerations due to the J_2 geopotential on a 50m satellite formation. The reaction wheel will absorb the fluxuation over an orbital period, but if the accelerations in the normal and tangential direction integrate to a non-zero number, the reaction wheels will eventually saturate.

Looking at equation F.4, the relative obrit between the two satellites can be changes by varying the following parameters $(a, b, \lambda_1, \lambda_2)$. The variables a and b just change the size and shape of the formation, while λ_1, λ_2 control the phasing of the formation. The phasing plays a very important roll in the direction of the gain. Figure F.2 shows the integrated value of the differential acceleration over one orbit as a function of λ_1, λ_2 . There are two things that should be taken from these plots. First, there are phasing angles that produce zero net gain in the torque both in the normal and tangential directions. These formation do not have a net gain in the system angular momentum when counteracting the differential J_2 disturbances. Also, the net gain appears to be somewhat sinusodal, and so the net gain is either positive, or negative dependent on the phasing angles.

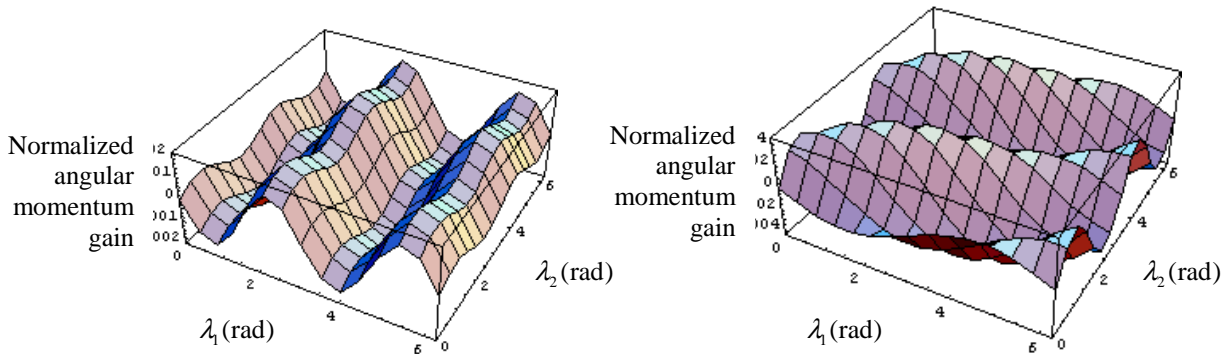


**Figure F.2: Net Angular Momentum Gain Over One Orbit
(Left) Tangential Direction (Right) Normal Direction**

Overall, Figure F.2 shows that while for most satellite formations, there is a net gain in the system angular momentum when counteracting the J_2 disturbance. However, the direction of the gain can be chosen at will by simply rephasing the satellite formation, and can be used to control the system angular momentum.